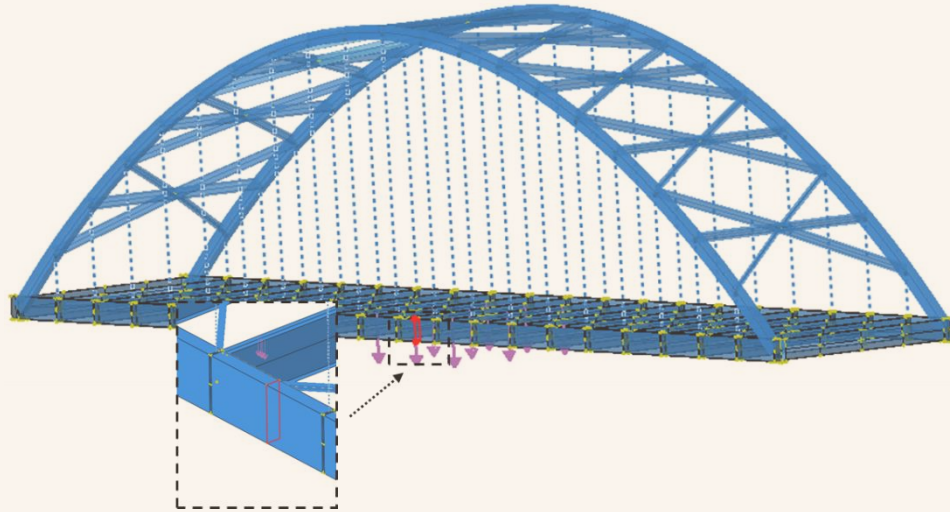


# **Development of a Simplified Methodology to Assess the Internal Redundancy of Bolted-Built-Up Tied Arch Members**



by

**Shah Zaib Farooq  
Cem Korkmaz  
Robert J. Connor**

**Purdue University  
West Lafayette, IN  
September 12, 2025**

## TECHNICAL REPORT DOCUMENTATION PAGE

1. Report No. doi.org/10.5703/1288284318219	2. Government Accession No.	3. Recipient's Catalog No.	
4. Title and Subtitle Development of a Simplified Methodology to Assess the Internal Redundancy of Bolted-Built-Up Tied Arch Members		5. Report Date September 2025	
		6. Performing Organization Code:	
7. Author(s) Shah Zaib Farooq Cem Korkmaz Robert J. Connor (ORCID 0000-0002-6964-3317)		8. Performing Organization Report No.	
9. Performing Organization Name and Address Purdue University West Lafayette, IN		10. Work Unit No.	
		11. Contract or Grant No. 693JJ322C000014	
12. Sponsoring Agency Name and Address Office of Bridges and Structures Federal Highway Administration 1200 New Jersey Ave SE Washington, DC 20590		13. Type of Report and Period Final Report, July 2022 – September 2025	
		14. Sponsoring Agency Code	
15. Supplementary Notes			
<p>16. Abstract</p> <p>Tied arch bridges represent a vital component of the nation's infrastructure, valued for their structural efficiency and aesthetic qualities. These bridges rely on arch ribs to transfer vertical loads into horizontal thrusts, which are counteracted by the tie beams (TBs) acting in axial tension. In addition to this axial tension, TBs are also subjected to strong axis bending mainly due to live loads from vehicular traffic. The TB, therefore, is a critical structural component, maintaining the internal equilibrium of the system by resisting the spreading forces generated by the arch and bending caused by the moving vehicular loads. These TBs are often constructed as built-up steel members, a design that inherently possesses a degree of internal redundancy, allowing them to redistribute loads among their components following a localized fracture.</p> <p>Under current AASHTO standards, these members are often classified as non-redundant steel tension members (NSTMs), resulting in additional inspection rigor. The existing AASHTO Guide Specifications for Internal Redundancy of Mechanically Fastened Built-up Steel Members (IRM Guide Spec.) provides limited information for assessing members under the combined axial tension and bending loads characteristic of TBs (1). This knowledge gap has led to a conservative approach, subjecting these bridges to more resource-intensive inspections, even when their actual risk profile may be comparable to typical bridges. This project was initiated to develop simplified methodologies that accurately assess the internal redundancy of bolted-built-up tie beams. The goal is to provide a reliable framework for engineers to evaluate these members, ensuring safety while reducing the need for regular hands-on inspection, ultimately contributing to more efficient bridge management practices.</p>			
17. Key Words bridges, steel bridges, tied arch bridges, tie beams, internally redundant member, non-redundant steel tension member		18. Distribution Statement No restrictions.	
19. Security Classif. (of this report) Unclassified	20. Security Classif. (of this page) Unclassified	21. No. of Pages	22. Price

Form DOT F 1700.7 (8-72)

Reproduction of completed page authorized.

SI* (MODERN METRIC) CONVERSION FACTORS				
APPROXIMATE CONVERSIONS TO SI UNITS				
Symbol	When You Know	Multiply By	To Find	Symbol
<b>LENGTH</b>				
in	inches	25.4	millimeters	mm
ft	feet	0.305	meters	m
yd	yards	0.914	meters	m
mi	miles	1.61	kilometers	km
<b>AREA</b>				
in <sup>2</sup>	square inches	645.2	square millimeters	mm <sup>2</sup>
ft <sup>2</sup>	square feet	0.093	square meters	m <sup>2</sup>
yd <sup>2</sup>	square yard	0.836	square meters	m <sup>2</sup>
ac	acres	0.405	hectares	ha
mi <sup>2</sup>	square miles	2.59	square kilometers	km <sup>2</sup>
<b>VOLUME</b>				
fl oz	fluid ounces	29.57	milliliters	mL
gal	gallons	3.785	liters	L
ft <sup>3</sup>	cubic feet	0.028	cubic meters	m <sup>3</sup>
yd <sup>3</sup>	cubic yards	0.765	cubic meters	m <sup>3</sup>
NOTE: volumes greater than 1000 L shall be shown in m <sup>3</sup>				
<b>MASS</b>				
oz	ounces	28.35	grams	g
lb	pounds	0.454	kilograms	kg
T	short tons (2000 lb)	0.907	megagrams (or "metric ton")	Mg (or "t")
<b>TEMPERATURE (exact degrees)</b>				
°F	Fahrenheit	5 (F-32)/9 or (F-32)/1.8	Celsius	°C
<b>ILLUMINATION</b>				
fc	foot-candles	10.76	lux	lx
fl	foot-Lamberts	3.426	candela/m <sup>2</sup>	cd/m <sup>2</sup>
<b>FORCE and PRESSURE or STRESS</b>				
lbf	poundforce	4.45	newtons	N
lbf/in <sup>2</sup>	poundforce per square inch	6.89	kilopascals	kPa
APPROXIMATE CONVERSIONS FROM SI UNITS				
Symbol	When You Know	Multiply By	To Find	Symbol
<b>LENGTH</b>				
mm	millimeters	0.039	inches	in
m	meters	3.28	feet	ft
m	meters	1.09	yards	yd
km	kilometers	0.621	miles	mi
<b>AREA</b>				
mm <sup>2</sup>	square millimeters	0.0016	square inches	in <sup>2</sup>
m <sup>2</sup>	square meters	10.764	square feet	ft <sup>2</sup>
m <sup>2</sup>	square meters	1.195	square yards	yd <sup>2</sup>
ha	hectares	2.47	acres	ac
km <sup>2</sup>	square kilometers	0.386	square miles	mi <sup>2</sup>
<b>VOLUME</b>				
mL	milliliters	0.034	fluid ounces	fl oz
L	liters	0.264	gallons	gal
m <sup>3</sup>	cubic meters	35.314	cubic feet	ft <sup>3</sup>
m <sup>3</sup>	cubic meters	1.307	cubic yards	yd <sup>3</sup>
<b>MASS</b>				
g	grams	0.035	ounces	oz
kg	kilograms	2.202	pounds	lb
Mg (or "t")	megagrams (or "metric ton")	1.103	short tons (2000 lb)	T
<b>TEMPERATURE (exact degrees)</b>				
°C	Celsius	1.8C+32	Fahrenheit	°F
<b>ILLUMINATION</b>				
lx	lux	0.0929	foot-candles	fc
cd/m <sup>2</sup>	candela/m <sup>2</sup>	0.2919	foot-Lamberts	fl
<b>FORCE and PRESSURE or STRESS</b>				
N	newtons	0.225	poundforce	lbf
kPa	kilopascals	0.145	poundforce per square inch	lbf/in <sup>2</sup>

## TABLE OF CONTENTS

<b>1</b>	<b>SUMMARY .....</b>	<b>1</b>
<b>2</b>	<b>INTRODUCTION AND BACKGROUND.....</b>	<b>2</b>
2.1	Inspection and classification of tie beams .....	2
2.2	Motivation.....	3
2.3	Objectives.....	3
<b>3</b>	<b>LITERATURE REVIEW .....</b>	<b>4</b>
3.1	Redundancy in bridges and the development of inspection standards .....	4
3.2	Types of redundancy.....	5
3.3	General sources of information.....	5
3.4	Evolution of redundancy understanding in steel bridges.....	6
3.5	Current reference on the redundancy of tie beams .....	7
3.6	Abbreviated summary of previous studies .....	8
3.6.1	Anecdotal observation: Hastings High Bridge .....	9
3.6.2	Experimental studies related to internal redundancy of built-up members .....	9
3.6.2.1	<i>Internal redundancy of built-up axially loaded tension members.....</i>	<i>9</i>
3.6.2.2	<i>Internal redundancy of built-up flexural members.....</i>	<i>10</i>
<b>4</b>	<b>GLOBAL MODELS .....</b>	<b>12</b>
4.1	Global bridge models .....	12
4.2	Birmingham Bridge .....	13
4.2.1	FE models of Birmingham Bridge.....	15
4.2.1.1	<i>Material properties.....</i>	<i>15</i>
4.2.1.2	<i>2D beam element model .....</i>	<i>15</i>
4.2.1.3	<i>2D model with 6 segments of TB as shell elements .....</i>	<i>19</i>
4.2.1.4	<i>3D beam elements model.....</i>	<i>19</i>
4.2.1.5	<i>3D model with 6 segments of TB as shell elements .....</i>	<i>20</i>
4.2.1.6	<i>3D model – complete TBs as shells .....</i>	<i>20</i>
4.2.2	Dead load analysis .....	21
4.2.3	Live load analysis .....	23
4.2.4	Change in the global forces under the live load.....	23
4.2.5	Longitudinal stress in the component plates of TB .....	26
4.3	Global response of Birmingham Bridge in faulted condition .....	31
4.3.1	Fracture scenarios .....	31
4.3.2	Effect of simulated fractures .....	33
4.4	Arkansas White River (AWR) Bridge.....	40
4.4.1	FE model of AWR bridge .....	41
4.4.2	Dead load analysis .....	41
4.4.3	Live load analysis .....	42
4.4.4	Change in the global response under live load .....	43
4.4.5	Longitudinal stress in the component plates of TB .....	47
4.5	Global response of AWR bridge in the faulted condition .....	55
4.5.1	Effect of simulated fractures .....	56
<b>5</b>	<b>SUBMODELLING PARAMETERS .....</b>	<b>64</b>
5.1	Force transfer from global to submodel .....	64

5.2	Submodel setup for the Birmingham Bridge.....	66
5.3	Bolted submodel configuration .....	68
5.4	Fracture scenarios.....	70
5.4.1	Force redistribution after fracture .....	70
5.4.2	Stress distribution and yielding.....	70
5.5	Transition to shell element modeling .....	74
6	DEVELOPMENT OF SIMPLIFIED METHODOLOGY FOR STRENGTH ANALYSIS .....	80
6.1	TB corner connections and fracture scenarios.....	80
6.1.1	TB geometries considered for development of formulations .....	82
6.2	Development of simplified methodology .....	85
6.2.1	Failure criterion.....	86
6.2.2	Critical plate: In the context of a fractured TB .....	87
6.3	P-M interaction curve for a fractured TB .....	88
6.3.1	Bottom plate fracture condition .....	89
6.3.2	Impact of changing loading sequence.....	94
6.3.3	Development of simplified methodology for bottom plate fractured TBs with horizontal tab connections .....	96
6.3.4	Side plate fracture condition .....	98
6.3.5	Development of simplified methodology for outer plate fractured TBs with horizontal tab connections .....	101
6.4	Evaluation of TBs with vertical tab connections.....	103
6.5	Evaluation of TBs with angle connections .....	108
6.6	Access holes in TBs .....	112
6.6.1	Top and bottom plates.....	112
6.6.2	Side plates .....	112
7	DEVELOPMENT OF SIMPLIFIED METHODOLOGY FOR FATIGUE ANALYSIS .....	116
7.1	Stress response of critical plates post-fracture.....	116
7.2	Stress estimation in critical plate under fatigue loading .....	120
7.3	Procedure to estimate stress range in the critical plate under fracture.....	124
7.4	Fatigue formulation for TBs with access holes in side plates.....	126
8	VALIDATION OF PROPOSED SIMPLIFIED METHODOLOGY .....	129
8.1	Assessment of proposed formulation for horizontal tab-based TBs .....	130
8.2	Assessment of proposed formulation for vertical tab-based TBs .....	134
8.3	Assessment of proposed formulation for angle-based TBs .....	137
9	SUMMARY AND CONCLUSIONS .....	141
9.1	Conclusions .....	141
10	REFERENCES.....	143

## LIST OF FIGURES

Figure 1. Illustration. Components of a tied arch bridge. ....	8
Figure 2. Illustration. Design elevation of Birmingham Bridge. ....	14
Figure 3. Illustration. Abaqus 2D all beams model of Birmingham Bridge.....	16
Figure 4. Graph. Comparison of FE and design plan dead load moments in Birmingham Bridge TB. ....	17
Figure 5. Illustration. Node labeling for TB region modelled as shell elements. ....	19
Figure 6. Illustration. Abaqus 3D-all beams model of Birmingham Bridge. ....	19
Figure 7. Illustration. Abaqus 3D model with 6 segments of TB as shells.....	20
Figure 8. Illustration. Final FE model of Birmingham Bridge. ....	21
Figure 9. Graph. Dead load moment in the TB for different FE models.....	22
Figure 10. Graph. Tension in the hanger under different loading conditions.....	24
Figure 11. Graph. Bending moment in the TB under different loading conditions.....	25
Figure 12. Graph. Vertical deflection in TB under different loading conditions. ....	25
Figure 13. Graph. Tie beam location for stress evaluation when trucks are placed at midspan... 26	
Figure 14. Graph. Longitudinal stress (S11) at mid span between FB connections when Birmingham Bridge is subjected to dead load. ....	27
Figure 15. Graph. Longitudinal stress (S11) at mid span between FB connections when Birmingham Bridge is subjected to dead and lane load.....	27
Figure 16. Graph. Longitudinal stress (S11) at midspan between FB connections when Birmingham Bridge is subjected to dead and lane load, and trucks at mid-span. ....	28
Figure 17. Illustration. TB location for stress evaluation when trucks are placed at quarter-span, .....	29
Figure 18. Graph. Longitudinal stress (S11) at quarter span between FB connections when Birmingham Bridge is subjected to dead load. ....	29
Figure 19. Graph. Longitudinal stress (S11) at quarter span between FB connections when Birmingham Bridge is subjected to dead and lane load.....	30

Figure 20. Graph. Longitudinal stress (S11) at quarter span between FB connections when Birmingham Bridge is subjected to dead and lane load, and trucks at mid-span. ....	30
Figure 21. Graph. Moment in the fractured TB when trucks are placed at mid-span and fractured between FBs.....	34
Figure 22. Graph. Moment in the fractured TB when trucks are placed at quarter-span and fractured between FBs.....	34
Figure 23. Graph. Vertical deflection in the fractured TB when trucks are placed at mid-span and fractured between FBs. ....	39
Figure 24. Graph. Vertical deflection in the fractured TB when trucks are placed at quarter-span and fractured between FBs.....	39
Figure 25. Illustration. 3D model of AWR bridge.....	41
Figure 26. Graph. Comparison of FE and design plan dead load moments in TB of AWR Bridge. ....	42
Figure 27. Chart. Tension in hangers of AWR bridge under different loading conditions. ....	44
Figure 28. Graph. Bending moment in TB of AWR bridge under different loading conditions..	45
Figure 29. Graph. Vertical deflection in TB of AWR bridge under different loading conditions.	46
Figure 30. Graph. Vertical deflection in TB of AWR bridge under different loading conditions.	46
Figure 31. Graph. TB location for stress evaluation when trucks are placed at mid-span. ....	47
Figure 32. Graph. TB location for stress evaluation when trucks are placed at quarter-span. ....	48
Figure 33. Graph. Longitudinal stress (S11) along the width of bottom plate when subjected to dead load. ....	49
Figure 34. Graph. Longitudinal stress (S11) along the width of top plate when subjected to dead load.....	49
Figure 35. Graph. Longitudinal stress (S11) along the height of outer plate when subjected to dead load.....	50
Figure 36. Graph. Longitudinal stress (S11) along the width of bottom plate when subjected to dead and lane load.....	50
Figure 37. Graph. Longitudinal stress (S11) along the width of top plate when subjected to dead and lane load. ....	51

Figure 38. Graph. Longitudinal stress (S11) along the height of the outer plate when subjected to dead and lane load.....	51
Figure 39. Graph. Longitudinal stress (S11) along the width of bottom plate when subjected to dead and lane load, and trucks at midspan.....	52
Figure 40. Graph. Longitudinal stress (S11) along the width of top plate when subjected to dead and lane load, and trucks at midspan. ....	52
Figure 41. Graph. Longitudinal stress (S11) along the height of outer plate when subjected to dead and lane load, and trucks at midspan. ....	53
Figure 42. Longitudinal stress (S11) along the width of bottom plate when subjected to dead and lane load, and trucks at quarter span.....	53
Figure 43. Graph. Longitudinal stress (S11) along the width of top plate when subjected to dead and lane load, and trucks at quarter span .....	54
Figure 44. Graph. Longitudinal stress (S11) along the height of outer plate when subjected to dead and lane load, and trucks at quarter span .....	54
Figure 45. Graph. Moment in the fractured TB when trucks are placed at mid span and fractured at FB connection. ....	57
Figure 46. Graph. Moment in the fractured TB when trucks are placed at mid span and fractured between FBs.....	57
Figure 47. Graph. Vertical deflection in the fractured TB when trucks are placed at mid span and fractured between FBs .....	61
Figure 48. Graph. Vertical deflection in the fractured TB when trucks are placed at quarter span and fractured between FBs.....	62
Figure 49. Illustration. Birmingham Bridge with highlighted TB section for submodeling studies. ....	67
Figure 50. Illustration. Birmingham Bridge submodel with boundary conditions. ....	67
Figure 51. Illustration. Comparison of longitudinal stress (ksi), axial force (kips) indicated by red arrow, and moment (kip-inch) indicated by blue arrow in the global and submodel. ....	68
Figure 52. Illustration. Bolted submodel for Birmingham Bridge.....	69
Figure 53. Illustration. Stress distribution across different plates of bolted TB when bottom plate is fractured. ....	72



Figure 54. Illustration. Stress distribution across different plates of bolted TB when a side plate and connected tabs are fractured.....	73
Figure 55. Illustration. Fractured bottom plate. ....	75
Figure 56. Graph. Comparison of maximum principal stress at the critical bolt hole in the tab plate under bottom plate fracture and pure axial loading .....	75
Figure 57. Graph. Comparison of global axial displacement under bottom plate fracture and pure axial loading.....	76
Figure 58. Graph. Comparison of bolt force under bottom plate fracture and pure axial loading. ....	77
Figure 59. Illustration. Representative FE shell model with meshing details around the bolts....	79
Figure 60. Illustration. TB geometries with different corner connections.....	80
Figure 61. Illustration. Flowchart illustrating the assumed fracture scenarios and fractured plates with different corner connections. ....	82
Figure 62. Illustration. TB sections of four baseline geometries.....	83
Figure 63. Graph. Ratio of bending to tensile stress along the length of the TB.....	85
Figure 64. Graph. Typical P-M curve of a fractured TB. ....	89
Figure 65. Graph. P-M curve for bottom plate fractured TBs with horizontal tab connections..	91
Figure 66. Graph. P-M curve for bottom plate fractured Birmingham TBs with horizontal tab connections .....	92
Figure 67. Graph. P-M curve for bottom plate fractured AWR TBs with horizontal tab connections .....	92
Figure 68. Graph. P-M curve for bottom plate fractured BNTA TBs with horizontal tab connections .....	93
Figure 69. Graph. P-M curve for bottom plate fractured IL64 TBs with horizontal tab connections .....	93
Figure 70. Graph. Impact of loading sequence on the P-M curve of bottom plate fractured Birmingham Bridge. ....	95
Figure 71. Graph. Impact of loading sequence on the P-M curve of bottom plate fractured AWR Bridge.....	96

Figure 72. Graph. Normalized remaining axial capacity in relation to bottom plate % fractured area.....	97
Figure 73. Graph. P-M curve for side plate fractured AWR TB with horizontal tab connection.	99
Figure 74. Graph. P-M curve for side plate fractured TB geometries with 33% fractured area.	100
Figure 75. Illustration. Side plate fractured BNTA-2 geometry subjected to pure bending (deformations in inset figure are magnified 5 times).....	100
Figure 76. Illustration. Side plate fractured BNTA-2 geometry subjected to 5 ksi of tensile and bending stresses (deformations in inset figure are magnified 5 times).....	101
Figure 77. Graph. P-M curve for bottom plate fractured baseline TB geometries with vertical tab connection. ....	105
Figure 78. Graph. P-M curve for bottom plate fractured baseline TB geometries with vertical tab connection. ....	105
Figure 79. Graph. P-M curve for bottom plate fractured baseline TB geometries with angle connection. ....	109
Figure 80. Graph. P-M curve for bottom plate fractured baseline TB geometries with angle connection. ....	109
Figure 81. Illustration. Tie beam with a manhole located in one of its side plates sized according to the suggested criteria. ....	114
Figure 82. Graph. Comparison of axial capacity ratio between proposed approach and FEA results for tie beams with access holes. ....	114
Figure 83. Comparison of flexural capacity ratio between proposed approach and FEA results for tie beams with access holes.....	115
Figure 84. Illustration. Longitudinal stress distribution in the critical plate (side plate) when bottom plate and welded tabs are fractured.....	117
Figure 85. Graph. Longitudinal stress in the side plate when bottom plate and welded tabs are fractured. ....	118
Figure 86. Illustration. Longitudinal stress distribution in the tab plate when side plate is fractured. ....	119
Figure 87. Graph. Longitudinal stress in the tab plate when side plate is fractured. ....	119

Figure 88. Graph. Fatigue stress range in the critical plate (tab) of the AWR tie beam with a side plate access hole under 1 ksi axial stress and bottom plate fracture. ....	127
Figure 89. Graph. P-M curve comparison between simplified method and FEA for LaCrosse TB when bottom plate is fractured.....	131
Figure 90. Graph. P-M curve comparison between simplified method and FEA for Atchison TB when bottom plate is fractured.....	131
Figure 91. Graph. Comparison between simplified method and FEA for fatigue stress in the critical plate in the LaCrosse TB when bottom plate is fractured.....	133
Figure 92. Graph. Comparison between simplified method and FEA for fatigue stress in the critical plate in the LaCrosse TB when side plate is fractured.....	134
Figure 93. Graph. P-M curve comparison between simplified method and FEA for LaCrosse TB with vertical tabs when bottom plate is fractured. ....	135
Figure 94. Graph. P-M curve comparison between simplified method and FEA for Atchison TB with vertical tabs when bottom plate is fractured. ....	135
Figure 95. Graph. Comparison between simplified method and FEA for fatigue stress in the critical plate in the LaCrosse TB with vertical tabs when bottom plate is fractured. ....	136
Figure 96. Graph. Comparison between simplified method and FEA for fatigue stress in the critical plate in the LaCrosse TB with vertical tabs when side plate is fractured. ....	137
Figure 97. Graph. P-M curve comparison between simplified method and FEA for LaCrosse TB with angles when bottom plate is fractured .....	138
Figure 98. Graph. P-M curve comparison between simplified method and FEA for Atchison TB with angles when bottom plate is fractured .....	138
Figure 99. Graph. Comparison between simplified method and FEA for fatigue stress in the critical plate in the LaCrosse TB with angles when bottom plate is fractured .....	139
Figure 100. Graph. Comparison between simplified method and FEA for fatigue stress in the critical plate in the LaCrosse TB with angles when side plate is fractured .....	140

## LIST OF TABLES

Table 1. Suspender member dimensions of Birmingham Bridge. ....	15
Table 2. Comparison of tension in TB across different models with design plans. ....	17
Table 3. Geometric properties and design loads of Birmingham bridge TB .....	18
Table 4. Hanger forces in different models of Birmingham Bridge (kips).....	22
Table 5. Difference (%) in the axial force of fractured TB when trucks are placed at mid-span. 35	
Table 6. Difference (%) in the axial force of fractured TB when trucks are placed at quarter-span .....	36
Table 7. Difference (%) in the hanger forces connected to the fractured TB when trucks are placed at mid-span.....	37
Table 8. Difference (%) in the hanger forces connected to the fractured TB when trucks are placed at quarter-span.....	38
Table 9. Difference (%) in the axial force of fractured TB when trucks are placed at mid-span. 58	
Table 10. Difference (%) in the axial force of fractured TB when trucks are placed at quarter-span .....	59
Table 11. Difference (%) in the hanger forces of fractured TB when trucks are placed at mid span and fractured between FBs.....	60
Table 12. Difference (%) in the hanger forces of fractured TB when trucks are placed at mid span and fractured at FB.....	60
Table 13. Axial force (kips) in the impacted and adjacent section of TB of Birmingham Bridge 65	
Table 14. Axial force (kips) in the impacted and adjacent section of TB of AWR Bridge .....	65
Table 15. Change in length in the fractured TB section of Birmingham Bridge.....	66
Table 16. Change in length in the fractured TB section of AWR Bridge.....	66
Table 17. Axial force (kips) in different plates of TB when subjected to various fracture scenarios .....	70
Table 18. Axial forces (kips) in different plates of TB in shell submodel when subjected to axial load and bottom plate fractured .....	78

Table 19. Axial forces (kips) in different plates of TB in solid submodel when subjected to axial load and bottom plate fractured .....	78
Table 20. TB geometries with tab-type corner connections .....	84
Table 21. TB geometries with angle-type corner connections .....	84
Table 22. Limiting plastic strains for different TB geometries .....	87
Table 23. The applied loads for the BNTA geometry .....	91
Table 24. Percentage fractured area for the TBs with horizontal tabs under bottom plate fracture conditions.....	94
Table 25. Estimation and comparison of P-M interaction curve parameters with the FEA values for a bottom plate fractured TB with horizontal tabs at corner connection .....	98
Table 26. Percentage fractured area for the TBs with horizontal tabs under side plate fracture conditions.....	102
Table 27. Estimation and comparison of P-M interaction curve parameters with the FEA values for a side plate fractured TB with horizontal tabs at corner connection .....	103
Table 28. Percentage area fractured for different TB corner connections .....	104
Table 29. Estimation and comparison of P-M interaction curve parameters with the FEA values for a bottom plate fractured TB with vertical tabs at corner connection .....	107
Table 30. Estimation and comparison of P-M interaction curve parameters with the FEA values for a side plate fractured TB with vertical tabs at corner connection .....	107
Table 31. Estimation and comparison of P-M interaction curve parameters with the FEA values for a bottom plate fractured TB with angle at corner connection .....	111
Table 32. Estimation and comparison of P-M interaction curve parameters with the FEA values for a side plate fractured TB with angle at corner connection .....	111
Table 33. Proposed equations to estimate the stress range in the critical plate under fatigue loading .....	122
Table 34. Proposed equations to estimate the stress range in the critical plate under fatigue loading .....	128
Table 35. TB geometries with tab-type corner connections used in the validation study .....	129
Table 36. TB geometries with angle-type corner connections used in the validation study .....	129

## **LIST OF ABBREVIATIONS AND SYMBOLS**

### **Abbreviations**

AASHTO	American Association of State Highway and Transportation Officials
AISC	American Institute of Steel Construction
AWR	Arkansas White River
BNTA	Blennerhassett Network Tied Arch
CBFR	cross-boundary fracture resistance
DL	dead load
FCM	fracture critical member
FB	floorbeam
FE	finite element
FEA	finite element analysis
FHWA	Federal Highway Administration
IL64	Illinois Route 64
IRM	internally redundant member
kip	kilopound (1000 lbf)
ksi	kips per square inch
LL	live load
LRFD	Load and Resistance Factor Design
MBE	Manual for Bridge Evaluation
NBIS	National Bridge Inspection Standards
NSTM	nonredundant steel tension member
P-M	axial load-moment
SCF	stress concentration factor
TB	tie beam

## Symbols

$A$	area
$A_{An}$	net area of an angle used in the corner connection of a tie beam
$A_{BP}$	net area of bottom plate of a tie beam
$A_{Frac}$	fractured cross-sectional area
$A_{HH}$	area removed by the hand hole or access hole at the cross section
$A_{SP}$	net area of side plate of a tie beam
$A_{TP}$	net area of tab plate used in the corner connection of a tie beam
$A\%_{Frac}$	fractured cross-sectional area percentage
$C_{Axial}^{BP}$	remaining axial capacity ratio (bottom plate fractured)
$C_{Flex}^{BP}$	remaining moment capacity ratio (bottom plate fractured)
$C_{Axial}^{SP}$	remaining axial capacity ratio (side plate fractured)
$C_{Flex}^{SP}$	remaining moment capacity ratio (side plate fractured)
$F_y$	yield strength of steel
$I$	moment of inertia
$S_A$	stress at the end of the critical plate adjacent to the fractured component
$S_B$	stress at the mid-length of the critical plate
$S_C$	stress at the end of the critical plate connected to the unfractured component
$y$	centroidal distance
$\alpha$	scaling parameter
$\beta$	amplification parameter
$\Delta FFS_{Axial}$	nominal factored axial fatigue stress range in the critical component of the fractured TB due to the fatigue design LL
$\Delta FFS_{Flex}$	nominal factored flexural fatigue stress range in the critical component of the fractured TB due to the fatigue design LL

$\Delta FFS_{Total}$	total nominal factored fatigue stress range in the critical component of the fractured TB (ksi)
$\Delta FS$	nominal factored fatigue stress range in the given TB cross section in the unfaulted state
$\eta$	redundancy factor



# 1 SUMMARY

This research presents an analytical framework for evaluating the residual strength and fatigue performance of mechanically fastened built-up tie beams (TBs) in tied-arch bridges following localized fracture of single components. Although the American Association of State Highway and Transportation Officials (AASHTO) Guide Specifications for Internal Redundancy of Mechanically Fastened Built-up Steel Members (IRM Guide Spec) provide procedures for assessing faulted built-up members under pure axial or pure bending loads, they offer limited information on components subjected to combined axial tension and bending. This limitation is critical for TBs in tied-arch bridges, which routinely experience both loading types in service. As a result, redundancy assessment and fracture evaluation for such members remain inadequately addressed.

To fill this gap, a detailed finite element (FE) study was conducted. The investigation began with the development of global bridge models incorporating both shallow and deep TBs. Simulated fractures in the bottom and side plates produced negligible changes in global forces and displacements. This outcome indicated effective internal force redistribution within the TB cross-section and justified the use of localized sub-models for further evaluation.

Thirteen TB geometries identical, or similar to those used in real highway bridges were analyzed separately for three corner connection types: horizontal tabs, vertical tabs, or angles. Each configuration was evaluated under both bottom and side plate fracture conditions. Strength was assessed through a new axial force vs. moment interaction curve approach developed in the research using nonlinear finite element analysis (FEA). Next, a simplified approach that relies upon simple hand calculations was formulated based on fracture area percentage and geometric parameters. Fatigue analysis in the faulted state was also performed. This effort involved applying axial and bending loads separately, identifying the critical plate in each scenario, and estimating local amplified stress ranges at the critical location (holes) using FEA. Again, a simplified approach utilizing hand calculations for the fatigue evaluation in the faulted state was then developed.

To validate the proposed method, two additional TB geometries from two real in-service bridges were analyzed. These geometries were not part of the initial formulation process. The simplified predictions showed strong agreement with detailed FEA results for both strength and fatigue, confirming the method's reliability and accuracy for these two bridges.

This work delivers a practical and efficient methodology to assess the internal redundancy and fatigue life of TBs under combined loading conditions. It addresses a key gap in current specifications and offers engineers a useful tool for inspection planning and maintenance of tied-arch bridges and provide a basis for specifications and commentary for consideration for inclusion in the IRM Guide Spec.

## 2 INTRODUCTION AND BACKGROUND

Tied-arch bridges are widely recognized for their efficient structural performance, seamlessly combining aesthetic appeal with material efficiency. These bridges rely on arch ribs to transfer vertical loads into horizontal thrusts, which are counteracted by the tie beams (TBs) acting in axial tension. In addition to this axial tension, TBs are also subjected to strong axis bending mainly due to live loads from vehicular traffic. The TB, therefore, is a critical structural component, maintaining the internal equilibrium of the system by resisting the spreading forces generated by the arch and bending caused by the moving vehicular loads.

Modern TBs in tied-arch bridges are often constructed as built-up steel members, composed of multiple plates bolted or welded together. This configuration offers advantages in terms of modular fabrication, efficient transportation, and straightforward assembly. However, the dual loading condition, axial tension and strong axis bending, makes the behavior of TBs distinct from standard built-up members designed for either axial force or bending alone. The structural performance of these built-up TBs is fundamentally governed by the ability of their individual components to interact and share load effectively. This load-sharing mechanism becomes particularly critical under localized fracture conditions. When one component of the TB fractures, the remaining intact elements redistribute the resulting forces internally to prevent any significant impact on the overall structural response. This internal redistribution is essential for maintaining the structure's integrity under in-service conditions.

The complexity of this load redistribution under combined axial and flexural loading necessitates a specialized approach to the design, analysis, and inspection of TBs in tied-arch bridges.

### 2.1 INSPECTION AND CLASSIFICATION OF TIE BEAMS

Tie beams are typically categorized as nonredundant steel tension members (NSTMs) due to their role as primary tension members and apparent lack of load path redundancy. This classification, which evolved from the earlier designation of fracture critical members (FCMs), was formalized with the revised National Bridge Inspection Standards<sup>1</sup> (NBIS) in 2022 (1). While this terminology shift aims to more accurately reflect the behavior of such members, the classification still mandates biennial hands-on inspection protocols evaluations. These inspections, while essential for ensuring public safety, are resource-intensive, demanding significant time, costs, and often extensive traffic management.

However, this strict classification does not fully account for the inherent internal redundancy exhibited by many TBs, especially those constructed as mechanically fastened built-up members. Numerous studies, including full-scale experimental tests, have demonstrated a behavior known as cross-boundary fracture resistance (CBFR) (2 through 5). This phenomenon allows load redistribution among intact components, enabling the bolted or riveted built-up member to maintain its load-carrying capacity even after the localized fracture of one component. The

---

<sup>1</sup> 23 CFR 650 Subpart C

impact of CBFR suggests that tie beams may have the potential to possess some internal redundancy, and that a more nuanced understanding of the behavior of tie beams is needed.

## **2.2 MOTIVATION**

The 2018 AASHTO Guide Specifications for Internal Redundancy of Mechanically Fastened Built-up Steel Members represents a significant advancement in acknowledging redundancy within built-up members (6). However, its applicability is confined to members primarily subjected to either axial force or bending moment independently. This limitation becomes a critical concern for TBs in tied arch bridges, which experience a unique combination of axial tension and strong axis bending, a condition not addressed by the current IRM Guide Specifications.

As a result, engineers lack standardized benchmarks or evaluation procedures to accurately assess the redundancy of TBs under their actual loading conditions. This gap leads to a conservative classification, where TBs are categorized as NSTMs, despite anecdotal evidence of their internal redundancy and capacity to redistribute loads after localized damage. Such classification necessitates more costly inspections, even when the actual risk may be similar to typical bridges. Furthermore, the current guide specifications do not account for detailing-specific behaviors in the built-up TBs, such as load sharing between interconnected plates depending on the corner connection in the TBs.

To address these limitations, this report develops simplified tools specifically designed to assess the internal redundancy of TBs under combined axial and bending loadings. These tools are intended to support rational reclassification decisions, enhance inspection efficiency, and ensure that the inherent resilience of properly designed TBs is accurately recognized.

## **2.3 OBJECTIVES**

The goals of this research project are to:

1. Develop simplified methods to accurately assess the internal redundancy of bolted built-up TBs in the tied arch bridges in the faulted state assuming sudden brittle fracture of one primary component in the member's cross section.
2. Estimate the fatigue stress range in the critical component of a fractured TB.
3. Develop procedures for bridge owners to consider when evaluating the internal redundancy of bolted-built-up tied arch members.

### 3 LITERATURE REVIEW

#### 3.1 REDUNDANCY IN BRIDGES AND THE DEVELOPMENT OF INSPECTION STANDARDS

The collapse of the Silver Bridge in 1967 (7) caused by the brittle fracture of a single eyebar in a suspension chain, marked a pivotal moment in bridge safety regulation in the United States. This failure highlighted the risks of non-redundant design, where failure of a single component can cause progressive collapse. In response, Congress passed the Federal-Aid Highway Act of 1968 asking the Secretary to establish standards to provide safety inspection of bridges, and to establish a program to train people to carry out those inspections. Through public rulemaking, FHWA finalized the National Bridge Inspection Standards (NBIS) in 1971 which established that all bridges on the Federal-aid highway system road had to be inspected, established the qualifications of those that conducted the inspection, and also a biennial frequency of the inspection. The term “fracture critical member,” or FCM, was first defined by AASHTO in 1978 with the publication of the *Guide Specification for Fracture Critical Nonredundant Steel Bridge Members* (8). This document was also a direct response to the Silver Bridge Collapse to outline the design, material, welding, and other fabrication criteria for new, steel tension members, that had low redundancy. In 1983, the suspended span of Mianus River Bridge carrying I-95 in Greenwich, CT collapsed (9). It was a two-girder bridge system with the suspended span supported by pin and hangers in each corner of the suspended span. In one corner, pack rust pushed one of two hangers off the pin which subsequently overloaded the second hanger leading to the whole span only being supported by three pin and hangers, which was not stable thus triggering the collapse. The collapse highlighted the importance of being up close to the hanger because visual inspections from a distance could not spot the pack rust compromising the hanger. It also highlighted the susceptibility of another low redundant system to collapse. In response to the Mianus River Bridge collapse, there was more public rulemaking leading to the revision to the NBIS in 1988 requiring bridge owners to identify bridges with FCMs and write specific in-service FCM inspection procedures. FHWA also published a document entitled *Inspection of Fracture Critical Bridge Members* in 1986 (10) which suggested that FCM inspection be “hands-on.” The “hands-on” requirement was formalized by additional public rule-making and final published in the 2005 version of the NBIS.

In 2022, the FHWA revised the NBIS to adopt more rigorous and risk-informed inspection practices. Among the key updates was the renaming of FCMs to nonredundant steel tension members (NSTMs), aiming to reduce misinterpretation that these members are inherently prone to fracture (1). The updated terminology emphasizes that the critical issue is the absence of redundancy, whether in load paths, system behavior, or internal detailing, which governs the potential for collapse following component failure. According to 23 CFR 650.305, NSTMs are defined as “*a primary steel member fully or partially in tension, and without load path redundancy, system redundancy, or internal redundancy, whose failure may cause a portion of or the entire bridge to collapse*”.

Earlier versions of AASHTO specifications recognized the importance of redundancy in design by limiting allowable fatigue stresses and mandating higher-quality materials and fabrication practices for critical members. The current Load and Resistance Factor Design (LRFD)

specifications build on this by explicitly incorporating redundancy into the design process through load modifiers, such as the redundancy factor ( $\eta$ ), which reflect the structural system's capacity to redistribute loads and enhance overall safety and reliability (11).

### 3.2 TYPES OF REDUNDANCY

Redundancy, in the context of bridge structures, implies that if a member or element fails, the loads previously carried by the failed component are redistributed to other members or elements capable of temporarily bearing the additional load. This redistribution of load prevents the collapse of the structure. Essentially, a bridge with redundancy will not collapse as it possesses sufficient reserved capacity to sustain the load even after the failure of one or several structural components. This resilience can be broadly classified into three types, as defined in 23 CFR 650.305 (1):

1. **Load path redundancy** refers to the presence of multiple primary supporting elements, often in parallel, such as girders or trusses. Load path redundancy is defined as “*A redundancy that exists based on the number of primary load-carrying members such that fracture of the cross section at one location of a member will not cause a portion of or the entire bridge to collapse*” (1). In general, FHWA considers bridges with three or more primary load-carrying members to be load path redundant (LPRM) (12). A structure is considered non-redundant if it has only two or fewer load paths. For instance, a framing system that has only two primary girders is a common example of such a system that does not possess load path redundancy. Thus, it is assumed that failure of one girder would result in the collapse of the span. Conversely, a structure with multiple girder lines is deemed to possess load path redundancy.
2. **System redundancy** is defined as “*A redundancy that exists in a bridge system without load path redundancy, such that fracture of the cross section at one location of a primary member will not cause a portion of or all of the bridge to collapse*” (1). When evaluating this form of redundancy, one considers the consequence of a failed NSTM on the response of the bridge under prescribed loads and failure criteria. Typically, this requires the use of advanced analytical tools but may also be based on more simple capacity checks. A method for evaluating such redundancy is included in the AASHTO Guide Specifications for Analysis and Identification of Fracture Critical Members and System Redundant Members (13).
3. **Internal redundancy** exists when the failure of an individual component within a mechanically fastened built-up member does not result in the failure of the entire member. Internal redundancy is defined as “*a redundancy that exists within a primary member cross-section without load path redundancy, such that fracture of one component will not propagate through the entire member, is discoverable by the applicable inspection procedures, and will not cause a portion of or the entire bridge to collapse*” (1).

### 3.3 GENERAL SOURCES OF INFORMATION

Broadly speaking, three primary sources provide insights into the behavior of faulted bridges, guiding the development of specification standards, enhancing design practices, and improving inspection protocols.

1. **Anecdotal observations:** Real-world cases where damaged structures continued to perform safely. For example, in 2021 the Hernando de Soto Bridge was closed due to a fracture in a welded box girder that was classified as an NSTM. Despite the severity of the defect, the bridge did not collapse. Such incidents highlighted that even under severe conditions, certain structural systems exhibit resilience, suggesting that current classification frameworks may not fully capture the actual in-service performance of such members (14).
2. **Experimental studies:** Controlled field and laboratory tests that provide direct insights into load redistribution. A compelling example is the Milton-Madison Bridge test, where a built-up bottom chord of a truss was intentionally fractured at mid-span while under live load. The bridge exhibited modest deflection but maintained stability, confirming that axially loaded built-up members can redistribute forces internally (3).
3. **Analytical models:** Theoretical studies and predictive equations that describe how redundancy and load-sharing occur. These models have been developed to estimate remaining capacity, predict fatigue life, and establish performance-based criteria for redundancy evaluation.

Together, these insights lay the foundation for developing comprehensive suggestion on evaluating structural redundancies in steel bridge systems. By integrating real-world observations, experimental data, and analytical models, this study aims to establish a more accurate, practical framework for assessing redundancy, enhancing design criteria, and optimizing inspection practices for steel bridge components.

### 3.4 EVOLUTION OF REDUNDANCY UNDERSTANDING IN STEEL BRIDGES

The understanding of redundancy in steel bridge design has evolved not only through catastrophic failures but also through the resilience observed in numerous in-service structures. While tragic collapses such as the Silver Bridge (1967) (7) and I-35W Bridge (2007) (15) spurred regulatory reforms, many non-collapse incidents have demonstrated the capacity of built-up members to redistribute loads and continue functioning despite localized damage. These observations challenge the traditional binary classification of members as either critical or non-critical, highlighting the need to consider partial capacity, detailing, and the potential for internal force redistribution.

While load-path redundancy has long been part of bridge design and evaluation practices, internal redundancy has gained formal recognition only recently. Studies and service records have shown that mechanically fastened built-up steel members, such as riveted girders, often resist sudden catastrophic failure. The AASHTO Manual for Bridge Evaluation<sup>2</sup> (MBE) recognizes this by recommending that riveted members be evaluated using fatigue Category C (which represents crack propagation), instead of Category D (used for first cracking in design), reflecting their superior redundancy (16). This understanding reinforces that not all tension members lacking load-path redundancy behave equally.

---

<sup>2</sup> The Manual for Bridge Evaluation, 3<sup>rd</sup> Edition (2017), is incorporated by reference in 23 CFR 650.317.

The 2022 NBIS acknowledged internal redundancy and established procedural requirements<sup>3</sup> for bridge owners seeking to reclassify NSTMs as redundant, which included a requirement to identify the nationally recognized method to be used to determine redundancy. One such method was provided by the 2018 AASHTO Guide Specification for Evaluating Internal Redundancy of Mechanically Fastened Built-Up Steel Members, otherwise referred to as the IRM Guide Spec. (6). This guide lays out validated analytical and experimental procedures to assess internal redundancy, enabling qualified members to be reclassified as internally redundant members (IRMs) and potentially benefit from more tailored evaluation protocols. The updated NBIS also explicitly acknowledges internal redundancy as a valid form of redundancy.

### 3.5 CURRENT REFERENCE ON THE REDUNDANCY OF TIE BEAMS

The IRM Guide Spec. (6), while rather comprehensive in terms of member types and cross-sections included (axial truss members and flexural members), specific provisions for the TBs of a tied arch bridge are not included because such members are *concurrently* subjected to axial and bending loads. As tied arch bridges offer viable solutions for longer spans and thus are common structures in the United States, there is a need to develop simplified procedures to evaluate the internal redundancy of TB members.

Tied arch bridges typically consist of two arch ribs which support a lower deck through a series of hanger cables as can be seen in Figure 1. The TB effectively counteracts the horizontal thrust of the arch. Tied arch bridges can be constructed with either vertical hangers or inclined hangers. When vertical hangers are evenly spaced along the TB, it is known as the moment tied configuration. On the other hand, in the inclined configuration, the hangers are arranged in a net-like structure. If the inclined hangers of a tied arch bridge cross each other at most once, it is referred to as a Nielsen type bridge. Conversely, when the hangers have multiple intersections, the tied arch bridge is categorized as a network arch bridge. [Click or tap here to enter text.](#) Arch ribs primarily experience compression, while the TBs are responsible for carrying the horizontal thrust of the arch and are therefore in tension. However, they are also subjected to bending due to various vertical dead and live loads along the span. Since there are only two TBs in most configurations and are subjected to tension, they are classified as NSTMs. While literature provides some research exploring the impact of hanger arrangement and bracing systems on tied arch bridge stability, no specific studies have investigated the redundancy of TBs in these bridge types. Traditionally, TBs in tied arch bridges are welded built-up members. However, a few examples exist where the four primary plate components used to make up the closed box of the TB were mechanically fastened using high strength bolts.

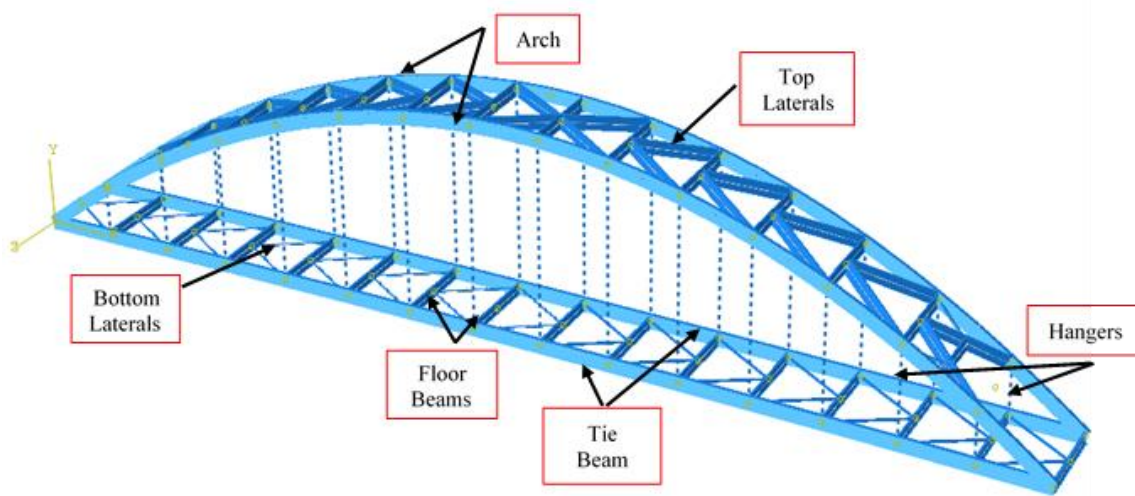
Previous studies, such as those conducted by Hebdon et al. (4, 5) and Lloyd et al. (2) have demonstrated the redundancy of built-up members under flexural or axial forces (i.e., truss members). However, no specific studies have been performed that focus entirely on the behavior of TBs (which are subjected to axial and bending loads) when an individual component is assumed to have fractured. In this regard, the current IRM Guide Spec. states the following in Article 2.2.4:

---

<sup>3</sup> 23 CFR 650.313(f)(1)(i)

The internal redundancy of tension tie members (or otherwise TBs) shall be evaluated using adequate methods of analysis. The analysis shall consider the load redistribution into the remaining components in the faulted state, as well as the second-order bending effects. Special consideration shall be given to these effects at gusset plates, hangers, and knuckles.

As noted,, very general information regarding TBs is provided in the IRM Guide Spec and no simplified approach has been developed otherwise. Thus, it can be inferred that the designer will perform detailed finite element analysis (FEA) in which an individual component is assumed to have failed. Such analysis can be challenging, especially when nonlinear material and geometry, local fastener interaction, and fatigue in the faulted state are considered. This report directly addresses this gap by developing simplified tools to assess the redundancy of TBs under realistic combined (axial and bending) loading conditions.



Source: FHWA

**Figure 1. Illustration. Components of a tied arch bridge.**

### **3.6 ABBREVIATED SUMMARY OF PREVIOUS STUDIES**

A literature review was conducted to identify if any information exists with respect to evaluating TBs when an individual component is assumed to have failed. No specific guide was identified. However, specific examples were found where the designer of a bridge made conservative assumptions regarding load redistribution. The general approach used is exemplified in the design of the Blennerhassett Island Bridge, which carries Route 50 over the Ohio River. For the redundancy evaluation, the designers assumed a failure occurred in any one of the individual components comprising the TB (e.g., failure of a side plate). In their approach, it was further assumed that the failed component is simply deleted for the entire length of the bridge. The effects of eccentric loading and added forces on connections, etc. were then accounted for in the design. Previous experimental and analytical research conducted by the research team suggests this approach is very conservative as the actual level of eccentricity and hence secondary moments may be much less than assumed. Nevertheless, the TBs designed using this approach are still classified as NSTMs.



The literature review did not identify much in the context of this specific topic (i.e., internal redundancy assessment of TBs) and no additional discussion is warranted. However, one example of a fracture in mechanically fastened built-up TB is worth noting, specifically the fractures observed in the Hastings High Bridge (17).

### **3.6.1 Anecdotal observation: Hastings High Bridge**

The Hastings High Bridge serves as a well-documented example of a bridge with a single component failure in a built-up TB which was designated as an NSTM. This riveted tied arch bridge was constructed in 1949 (17).

In 1997 and 1998, two arms-length inspections revealed two separate partial fractures in the outer side plate at opposite ends of the same TB. The first fracture was detected in 1997 and initiated at a riveted hole. The crack extended to a total of about 8 inches and arrested at an adjacent rivet hole. However, the second fracture, detected in 1998, propagated throughout the entire outer plate of the TB, originating near a tack weld near a floorbeam (FB) gusset plate. Investigation findings indicated that the plate had unusually high strength and low toughness. Retained documentation in the bridge file indicated the bridge had 32 plates with the same width, length, and thickness that were from three heats of steel. Only 1 of the 32 plates was from a heat with no documentation, the other two heats had documentation for mechanical and chemical properties. Microstructure and chemistry were assessed from cores removed from similar plates traced to two heats with documentation. Through deductive reasoning, it was determined that the fractured tie plate was the singular plate from the undocumented heat and was speculated to be a substitution of another steel that may have been improperly processed. Despite these fractures, the TB exhibited redundancy by preventing brittle fracture propagation into adjacent components and continued to bear service loads until the damage was detected and repaired.

### **3.6.2 Experimental studies related to internal redundancy of built-up members**

Built-up steel girders, commonly used in bridge construction until the 1960s, have shown remarkable resistance to complete fracture when a single component fails. Experimental testing on large-scale specimens has demonstrated that failures of a single component do not propagate to adjacent components, except under extreme condition. This research was performed by Hebdon et al. (4, 5) and Lloyd et al. (2); it aimed to evaluate the behavior and remaining capacity of partially failed built-up steel members and provide accurate methods for stress distribution and estimation.

#### ***3.6.2.1 Internal redundancy of built-up axially loaded tension members***

Lloyd et al. (2) studied mechanically fastened steel built-up tension members and their resistance to complete member fracture when a single component fractures. This resistance was labeled as cross-boundary fracture resistance (CBFR). Full-scale fracture tests and a finite-element model-based parametric study were performed to understand the load redistribution behavior of these members after an individual component failure, which is referred to as the faulted state. The research also provided simplified solutions for engineering analysis and estimation of safe inspection intervals based on member redundancy and fatigue life in a faulted condition.

Key findings of the research are as follows:

- CBFR allows properly detailed members to resist full cross-sectional fracture by arresting brittle fractures at the boundary between mechanically built-up components. CBFR is provided, at least in part, by ensuring individual components meet certain size and proportion criteria with respect to each other as well as the overall cross section. Simply put, no single component should be disproportionately large, as per the IRM Guide Spec.
- Material toughness is not essential for resisting full member fracture when CBFR is present.
- Large-scale testing has shown that a fracture is highly unlikely to pass through a randomly placed tack weld. Even in the rare event that a running fracture does intersect with a tack weld, the weld is likely to fracture, becoming separated from the base metal. This fracture of the weld prevents multiple component failures from occurring.
- After component failure, 80% to 100% of the redistributed load is carried by adjacent components, and shear lag effects and localized bending stress amplifications occur.
- Stress amplification factors were developed to evaluate after-fracture net section stress and calculate special inspection intervals.
- Failure of an individual component in a member comprised of multiple plates in the cross section has less impact on after-fracture behavior than in a member comprised of fewer components.

### *3.6.2.2 Internal redundancy of built-up flexural members*

Research conducted by Hebdon et al. (4, 5) involved testing fifteen large-scale specimens with a single failed component to determine stress redistribution in the remaining adjacent components. Experimental data was used to validate finite-element (FE) models, which were then used for a parametric study on various girder geometries. The study identified and quantified parameters affecting localized stresses near the failed component. Additionally, twelve specimens were cyclically loaded to determine the remaining fatigue life after a single component failure.

The key findings of this research are:

- Similar to the results observed in testing axially loaded members, CBFR allows properly detailed members to resist full cross-sectional fracture by arresting brittle fracture at the boundary between components. CBFR is provided, at least in part, by ensuring individual components meet certain size and proportion criteria with respect to each other as well as the overall cross section. Simply put, no single component should be disproportionately large, as per the IRM Guide Spec.
- The stress distribution in members with a failed component was nonlinear, with most of the redistributed stresses concentrated in the adjacent component.
- Nonsymmetrical cross sections with a single failed flange angle showed a stress increase of less than 10% in the remaining members due to the small proportion of tension flange area represented by the angle.
- Partial fatigue crack growth through a cover plate resulted in a larger stress increase only when crack growth exceeded 60% of the plate width. However, these larger stress cycles accounted for only a small portion of the member's fatigue life.
- Parameters like tension flange brace spacing and web height had an insignificant effect on localized stress distribution after a component failure.

- An equation was developed to calculate the amplified flexural stress in a member after the failure of an individual cover plate, considering the number of cover plates.
- Members with a single failed component exhibited substantial remaining fatigue life, and conservative fatigue categories were identified for different hole types.

Both (above) studies underscore the critical role of connection detailing in achieving redundancy and demonstrate that built-up members possess inherent resilience when properly designed. However, their limited focus on axial or flexural loading leaves a critical gap in understanding the redundancy of TBs, which are subjected to combined axial tension and bending. This report directly addresses this gap by developing a tailored methodology for evaluating the load carrying capacity of a fractured TB in tied arch bridges under combined axial and flexural loadings.

## 4 GLOBAL MODELS

To address the research gap identified in the literature review and achieve the objectives outlined in Section 2.3, this report adopts a structured analytical approach, encompassing the following steps:

1. The study begins with the creation of a finite element (FE) based global model using a dedicated FE program. This model is benchmarked against design plan forces to ensure accuracy and reliability, establishing confidence in its ability to replicate the bridge's structural behavior.
2. Upon successful validation, the FE model is employed to evaluate the global response of the tied arch bridge under localized component fractures within the TB. These fractures, which in this report refers to complete separation of one of the TB's constituent plates, are simulated at various locations to assess their impact. If the resulting variations in global forces and displacements are minimal, it would indicate effective internal force redistribution within the TB cross-section.
3. If the global response remains largely unaffected by localized fractures, a detailed submodel of the fractured TB is developed to accurately estimate its remaining strength capacity. This submodel is specifically designed to capture the internal force redistribution and redundancy mechanisms of the TB. A robust submodeling technique is adopted to ensure accurate transfer of forces or displacements from the global model to the submodel.
4. The investigation is further extended through a series of parametric studies involving various TB cross-section geometries. These studies aim to explore the behavior of fractured TBs, identify key trends, and facilitate the development of simplified methods for assessing their remaining capacity.
5. The submodel is further analyzed to estimate the remaining fatigue life of the TB under specified fracture scenarios. Based on these analyses, practical formulations are derived, enabling engineers to perform simplified hand calculations for fatigue life assessment.

The following sections present details about each of the above steps.

### 4.1 GLOBAL BRIDGE MODELS

The previous work on mechanically fastened built-up members revealed that there is negligible change in the stiffness of a member that had a fractured individual component. This is because a crack in a cover plate or angle is a small, localized discontinuity along the length of the component. In other words, the failed component does not entirely “go away” but rather, simply becomes discontinuous at a discrete point along the member. Hence, the flexural or axial stiffness of girders and truss members with failed components was found to be effectively unchanged. This was an important observation from the previous research as it showed that: 1) forces in the member in the unfaulted state are effectively the same as in the faulted state and 2) the forces in other components (girders or truss members) do not change when a single component fails. As a result, the evaluation of the faulted member is simplified, and a complex non-linear FEA of the entire structure is not needed to obtain the updated forces in the faulted or remaining unfaulted members.

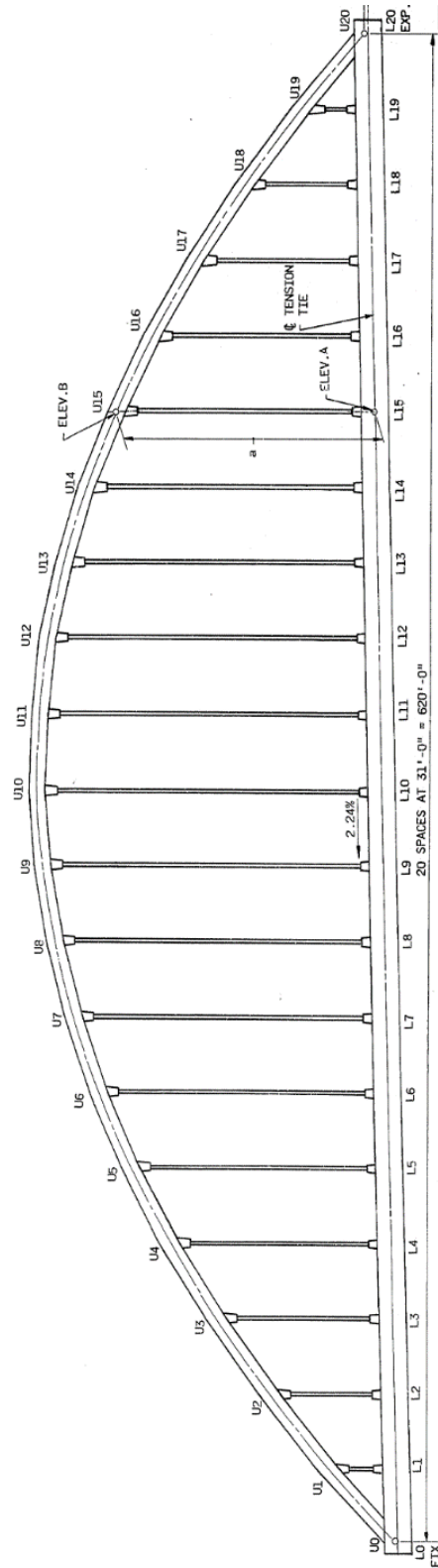
While this observation was confirmed in the flexural members and axial members studied and subsequently used to develop the IRM Guide Spec., it was unknown if such behavior would be observed should a single component of a TB were to fail. To investigate this question, two bridges were fully analyzed (i.e., full 3D non-linear FEA) to determine if failure of individual components in TB would result in changes in the forces in TB. Axial force and bending moment in the TB before component failure (unfaulted state) was compared to those forces after component failure (faulted state). Further, failure of side plates, and top or bottom plates, between and near FB connections was simulated and the effect on overall forces in other components, including the hangers, was evaluated to determine if forces in these unfaulted members change to a degree that should be considered in future evaluations. For these evaluations, dead load and live load were applied using the Redundancy II load combinations.

The following section presents an analysis of the full models of two bridges, the Birmingham Bridge and the Arkansas White River (AWR) Bridge, focusing on their global response to component fractures. For this report, a "large" TB is one that has a depth exceeding 8 feet, while a "shallow" TB refers to any depth below that threshold. It should be noted that, for the sake of clarity in this document, the terms "tie" and "TB" will be used interchangeably. The Birmingham Bridge, with a TB depth of 11 feet, 6 inches, is classified as having a "large" or deep TB, whereas the AWR Bridge, with a TB depth of 5 feet, 3 inches, is considered to have a "shallow" TB. To enhance the understanding of the behavior of both shallow and deep TBs under similar conditions and to validate the comparability of their responses, a comprehensive evaluation of the global response of these structures is conducted.

## **4.2 BIRMINGHAM BRIDGE**

The Birmingham Bridge is located in Pittsburgh, PA and crosses the Monongahela River. It was constructed in the early 1970s with a single tied arch span of 620 feet. The bridge is primarily constructed of ASTM A36 structural steel. The average daily traffic recorded for this bridge in 2020 was 19,244. The bridge was designed following the allowable stress design approach, and HS20-44 live loading was used. An elevation view is shown in Figure 2.

The concrete deck is supported by steel stringers that transfer load to the floorbeams (FBs) that are steel built-up I-sections which are 10 feet, 5 inches deep. These FBs are placed at each hanger location, spaced 31 feet apart. The center-to-center distance between TBs is 109 feet accommodating three 12 feet wide traffic lanes and a 10 feet shoulder on each side. The bridge includes approximately 6 feet wide sidewalks on both sides, which are supported on tapered cantilever beams connected to the TBs. The parabolic arch at the center span reaches a height of around 150 feet. The arch section is a 7-feet-deep, welded built-up box girder. The TBs are welded built-up steel boxes with a depth of 11 feet that can be classified as a deep TB. The bridge design loads are presented in Table 3.



Source: PennDOT

**Figure 2. Illustration. Design elevation of Birmingham Bridge.**

### 4.2.1 FE models of Birmingham Bridge

The FE analysis of the bridge was conducted in multiple stages to build confidence in the overall modeling approaches to be used. Abaqus software was used for all modeling. Each stage is described below.

#### 4.2.1.1 Material properties

For all steel components of the bridge, a modulus of elasticity of 29,000 ksi, a Poisson's ratio of 0.3, and the material density of 490 lb/ft<sup>3</sup> were used. The steel was assigned a yield strength of 50 ksi, and an ultimate tensile strength of 65 ksi. The inelastic portion of the stress-strain response was established using a Ramberg-Osgood equation, calibrated to match the specified yield and ultimate strengths. The hangers were modeled as connector elements, with their stiffness modeled as  $AE/L$ , where  $A$  denotes the cross-sectional area of the hanger cables (inch<sup>2</sup>) as specified in the design plans,  $L$  represents the hanger length as shown in Table 1 (inches), and  $E$  is the modulus of elasticity, set at 24,000 ksi in accordance with ASTM A586 (18).

**Table 1. Suspender member dimensions of Birmingham Bridge.**

Suspender Name <sup>a</sup>	Suspender Length (inches)
L1-U1 and L19-U19	351.34
L2-U2 and L18-U18	654.96
L3-U3 and L17-U17	922.86
L4-U4 and L16-U16	1,155.04
L5-U5 and L15-U15	1,351.50
L6-U6 and L14-U14	1,512.24
L7-U7 and L13-U13	1,637.26
L8-U8 and L12-U12	1,726.56
L9-U9 and L11-U11	1,780.14
L10-U10	1,798.00

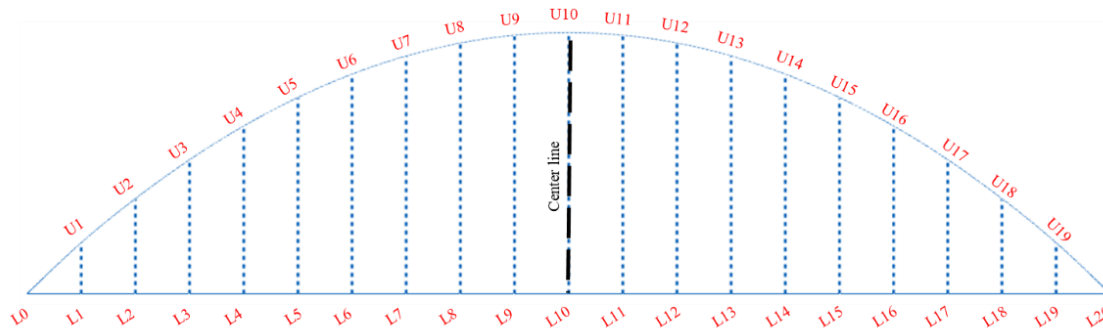
<sup>a</sup>Each suspender is four, 2-inch diameter strands.

#### 4.2.1.2 2D beam element model

First, a 2D model of the bridge was created using beam elements (Abaqus B32 elements). The TB and arch were connected with a pinned connection, while the load transferred by the floor beam (FB) to the TB was applied as point loads on the TB at the location of FB connections. Only dead loads (DL) were considered for this initial model to facilitate direct comparison with the values reported in the original design plans. Realistic support conditions were established at the ends of the TB through carefully selected boundary conditions. Specifically, a pinned condition was applied at one end of the TB, providing rotational freedom while restricting translational movement. At the other end of the TB, a roller condition was employed, allowing longitudinal movement while constraining vertical displacement. These boundary conditions

accurately represented the actual support behavior of the TBs in the model. The Abaqus model utilized for this purpose is shown in Figure 3.

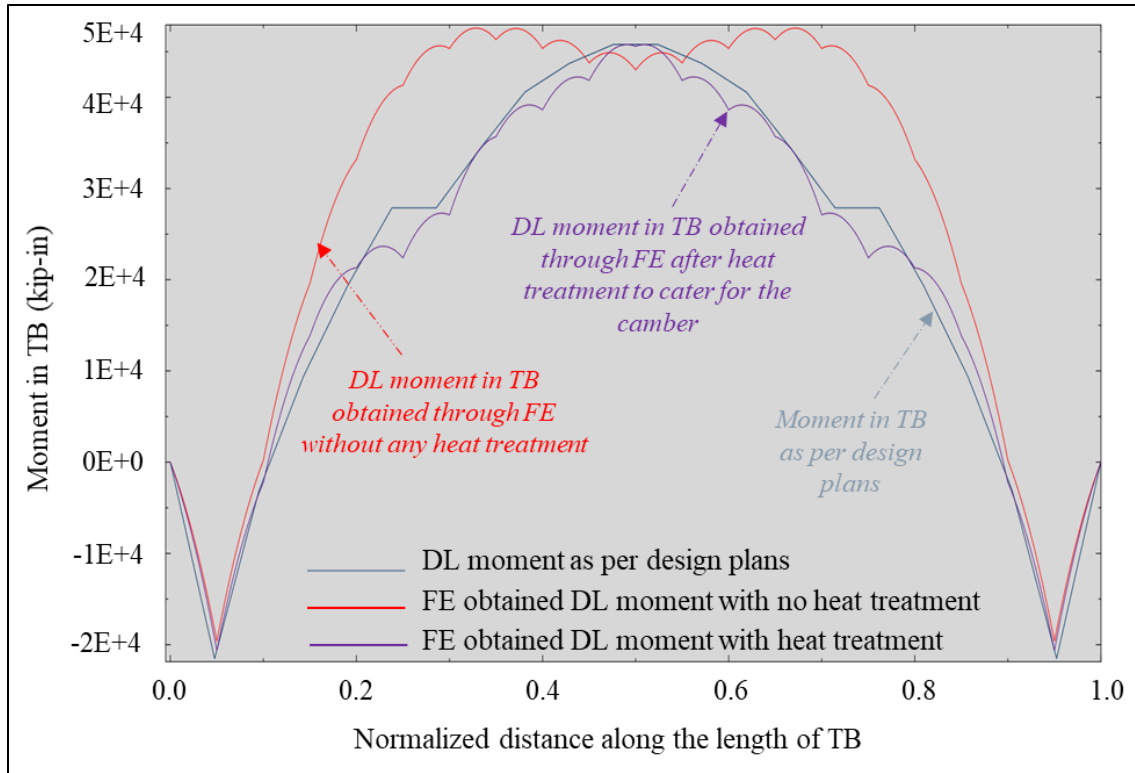
The primary objective of constructing this 2D model was to validate the model's ability to accurately predict the bearing reactions, axial forces, and bending moments in the TB, aligning with the values outlined in the design plans (Table 3). The model demonstrated a strong correlation with the design drawings for axial tension in the TB as can be noticed in Table 2. The percentage difference in the TB tension was calculated to be 2.64%. Following this, a detailed comparison of the TB bending moment under dead load with the values in the design plans was conducted. Design plans indicated that the TB was cambered during construction. To accurately reflect this in the Abaqus models, temperature variations were introduced, a common approach in tied arch bridge design to minimize bending moments in the TB (19). Specifically, this adjustment involved cooling (shortening) the TB and heating (lengthening) the arch, effectively reducing the dead load bending moments in the TB. As illustrated in Figure 4, the TB bending moment initially exhibited a deviation from the design values when no thermal adjustments were applied. Although the maximum positive and negative moment values remained consistent, the overall moment distribution differed. This discrepancy was resolved by implementing the camber adjustment through temperature variation, resulting in a bending moment distribution that closely matched the design plans.



Source: FHWA

**Figure 3. Illustration. Abaqus 2D all beams model of Birmingham Bridge.**





Source: FHWA

**Figure 4. Graph. Comparison of FE and design plan dead load moments in Birmingham Bridge TB.**

**Table 2. Comparison of tension in TB across different models with design plans.**

Model	Tension in TB (kips)	Difference (%)
2D	5050	-2.64
2D with 6 TB segments as shells	5055	-2.54
3D	4834	-6.81
3D with 6 TB segments as shells	4827	-6.94
3D – all shells	4820	-7.07

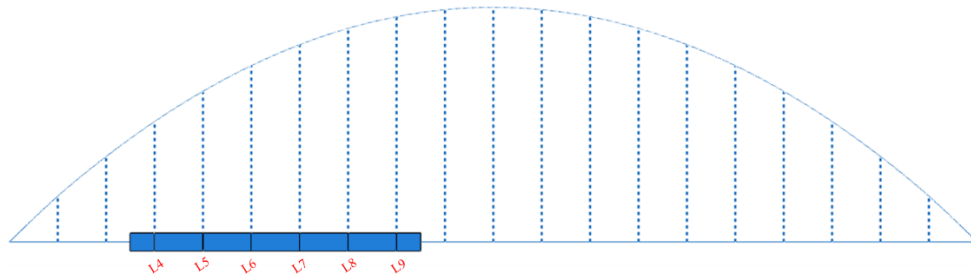
Table 3. Geometric properties and design loads of Birmingham bridge TB

Member			L0-L1 & L19-L20		L1-L2 & L18-L19		L2-L3 & L17-L18		L3-L4 & L16-L17		L4-L5 & L15-L16		L5-L6 & L14-L15		L6-L7 & L13-L14		L7-L8 & L12-L13		L8-L9 & L11-L12		L9-L10 & L10-L11	
Web plate dimensions <sup>a</sup> (in.)			138” x 7/8”		138” x 7/8”		138” x 7/8”		138” x 7/8”		138” x 7/8”		138” x 7/8”		138” x 7/8”		138” x 7/8”		138” x 7/8”		138” x 7/8”	
Flange plate dimensions (in.)			35” x 1”		35” x 1”		35” x 1”		35” x 1”		35” x 2”		35” x 2”		35” x 2”		35” x 1”		35” x 1”		35” x 1”	
Flange plate area (in. <sup>2</sup> )			329		329		355		373		382		382		382		373		355		338	
Flange plate inertia (in. <sup>4</sup> )			807,420		807,420		937,660		1,025,260		1,069,290		1,069,290		1,069,290		1,025,260		937,660		850,680	
Length (ft)			31.0077		31.0077		31.0077		31.0077		31.0077		31.0077		31.0077		31.0077		31.0077		31.0077	
Tension (kip) & Moment (kip-in.)	Loading		Tension	Moment	Tension	Moment	Tension	Moment	Tension	Moment	Tension	Moment	Tension	Moment	Tension	Moment	Tension	Moment	Tension	Moment	Tension	Moment
	(1) Dead Load		5,187	-21,530	5,187	-3,140	5,187	9,360	5,187	19,330	5,187	27,870	5,187	27,870	5,187	34,430	5,187	40,560	5,187	43,700	5,187	43,700
	(2) Maximum Positive Moment	L + I	176	60,420	230	102,220	238	129,720	294	141,160	300	142,770	300	142,770	356	130,950	360	114,330	414	90,920	405	73,890
		Sidewalk	15	3,930	19	6,910	19	8,900	23	9,890	23	10,090	23	10,990	28	9,340	28	8,090	33	6,310	31	4,600
	(3) Maximum Negative Moment	L + I	549	-50,270	505	-84,080	505	-106,640	457	-118,220	453	-119,750	453	-119,750	403	-110,880	403	-95,050	345	-73,400	366	-51,400
		Sidewalk	47	-4,170	42	-6,930	42	-8,760	38	-9,620	38	-9,720	38	-9,720	33	-8,840	33	-7,570	28	-5,750	31	-4,120
	(4) Maximum Tension	L + I	698	-6,410	698	-6,280	698	-5,880	698	-4,710	698	-2,650	698	-2,650	698	200	698	3,780	698	8,270	698	14,410
		Sidewalk	61	-240	61	-10	61	140	61	260	61	370	61	370	61	460	61	520	61	560	61	580
Actual Unit Stress (ksi)	Loading Combinations		Top	Bottom	Top	Bottom	Top	Bottom	Top	Bottom	Top	Bottom	Top	Bottom	Top	Bottom	Top	Bottom	Top	Bottom	Top	Bottom
	(1) + (2)		12.62	20.07	7.30	25.70	4.17	26.47	2.98	26.54	2.44	26.44	2.44	26.44	3.00	26.20	3.68	26.22	5.24	26.47	6.36	26.92
	(1) + (3)		24.18	10.96	25.62	9.23	24.12	8.15	22.74	7.74	21.62	8.13	21.62	8.13	20.40	9.07	19.37	10.79	18.32	12.98	17.33	15.72
	(1) + (4)		20.52	15.62	18.98	17.26	16.46	17.07	14.92	16.98	13.88	17.28	13.88	17.28	13.25	17.91	12.85	19.05	12.78	20.69	12.57	22.63
	Allowable Stress (ksi)	Top	27.00		27.00		25.70		25.11		24.84		24.84		25.35		26.02		27.00		27.00	
		Bottom	27.00		27.00		27.00		27.00		27.00		27.00		27.00		27.00		27.00		27.00	

<sup>a</sup>web plates locally thickened at the hangers and knuckle.

#### *4.2.1.3 2D model with 6 segments of TB as shell elements*

Following the initial modeling approach as mentioned in the previous section, a revised 2D model of the bridge was developed, incorporating a combination of shell and beam elements. Specifically, six segments of the TB, identified as L2P5 to L8P5 in Figure 5, were modeled using shell elements (Abaqus S8R), while the arch and the remaining sections of the TB continued to be modelled as beam elements. This section was chosen due to its significant bending moment gradients, as can be seen in Figure 4. The primary objective of this revised model was to accurately capture the interaction between shell and beam elements, ensuring that the transition between these elements was properly established. To achieve this, both rotational and translational displacements were constrained, providing full compatibility at the connections between the shell and beam elements. This setup was intended to maintain consistency with the design plans, even as the model complexity increased toward a full 3D shell model.

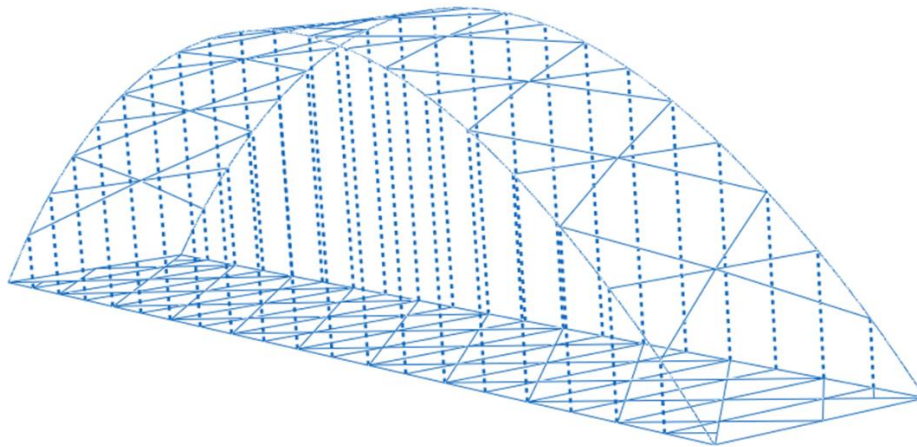


Source: FHWA

**Figure 5. Illustration. Node labeling for TB region modelled as shell elements.**

#### *4.2.1.4 3D beam elements model*

Following the successful validation of the 2D models against the design plans, a comprehensive 3D beam element model was developed, as illustrated in Figure 6. This 3D model continued to use B32 beam elements for the TBs, while the hangers were modeled as axial connector elements with stiffness values consistent with those used in the 2D models.



Source: FHWA

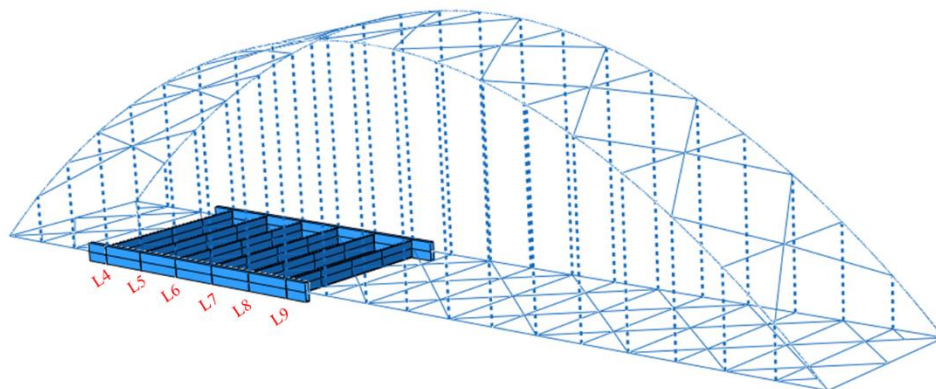
**Figure 6. Illustration. Abaqus 3D-all beams model of Birmingham Bridge.**

In this enhanced model, additional structural components, including FBs (floor beams), bottom lateral bracing, and top lateral bracing, were incorporated to capture the complete structural behavior. The FBs were connected directly to the TBs, with full rotational freedom about all three axes, ensuring accurate simulation of their interaction. Torsional restraint was achieved through the bottom lateral bracing between the TBs, enhancing the model's stability.

The applied load from the deck and stringers was modeled as a uniformly distributed load directly acting on the FBs. At the ends of the TBs, boundary conditions were selected to reflect realistic support conditions: a pinned boundary condition was applied at one end, allowing rotation but restricting translation, while a roller boundary condition was applied at the other end, permitting longitudinal movement but preventing vertical displacement. The connection between the arch and the TBs remained consistent with the approach used in the 2D beam element models.

#### ***4.2.1.5 3D model with 6 segments of TB as shell elements***

A comprehensive 3D model featuring segments of the TB represented as shell elements was subsequently developed as shown in Figure 7. The TBs in this model were modelled to closely mirror the 2D model with shell elements, but with the application extended to both TBs. Specifically, six segments of the TBs were modeled as shell elements, identical to the segments used in the 2D shell model. The element types were maintained consistent with the previous models, using S8R for shell elements and B32 for beam elements.



Source: FHWA

**Figure 7. Illustration. Abaqus 3D model with 6 segments of TB as shells.**

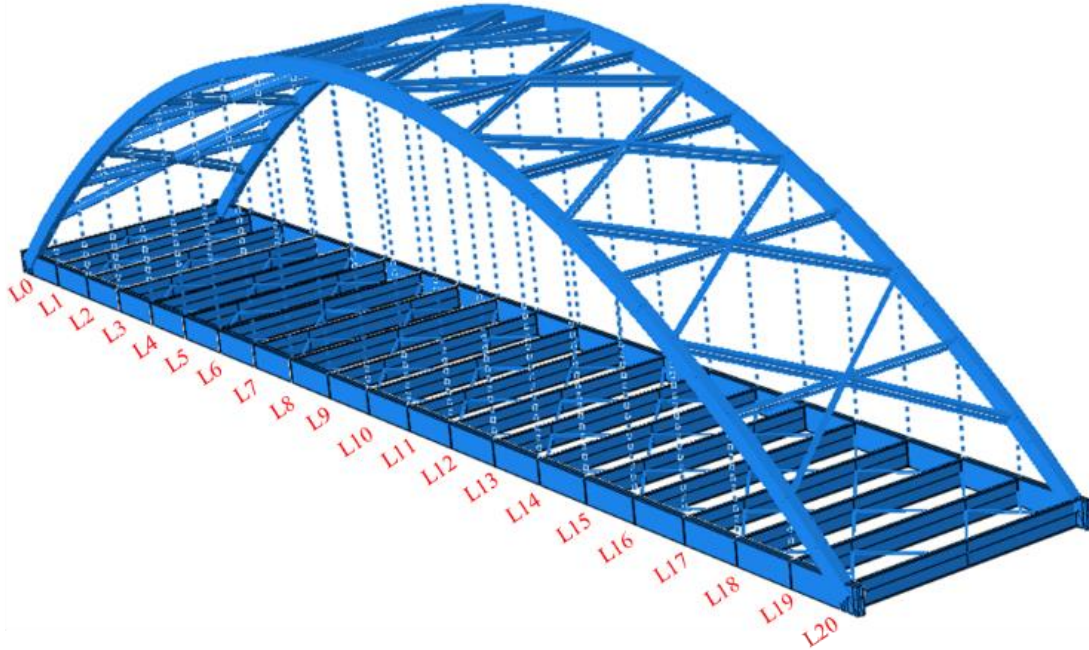
In regions where the TBs were modeled using shell elements, the FBs were also represented with shell elements to ensure accurate load transfer and interaction between the components. In contrast, the arches, bottom lateral bracing, top lateral bracing, and the remaining sections of the TBs continued to be modeled using beam elements.

#### ***4.2.1.6 3D model – complete TBs as shells***

Finally, a 3D model of the tied arch bridge was then developed, where both TBs were modeled using S8R shell elements, providing a detailed representation of their structural behavior. The FBs were also modeled using shell elements to accurately capture their interaction with the TBs. The load from the deck and stringer beams were transferred to the FBs and applied at their top

flange. Meanwhile, the arch and lateral bracing members were modeled as beam elements, maintaining an efficient yet realistic representation of the global structure.

The model configuration, presented in Figure 8, served as the final global model for further study. It was specifically developed to investigate the global response to localized fractures in TB. This detailed modeling approach ensured that the structural response to fractures was captured with higher fidelity, significantly enhancing the reliability of the analysis.



Source: FHWA

**Figure 8. Illustration. Final FE model of Birmingham Bridge.**

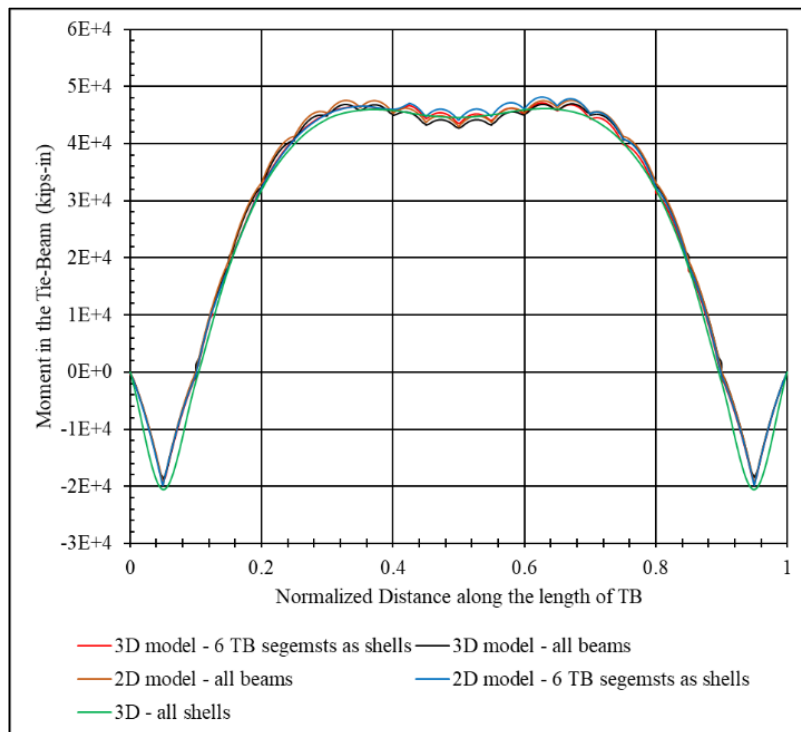
#### **4.2.2 Dead load analysis**

The above developed FE models exhibited strong agreement with the design plan values for dead load conditions, confirming their reliability. Specifically, the computed values for tension in TB are summarized in Table 2, while Figure 9 illustrates the bending moment results. According to the design plans, the reaction and tension in the TB are 4614 kips and 5187 kips, respectively.

Table 4 shows that hanger forces were also consistent for all FE models. As the bridge is symmetrical about the center line, only half of the hanger forces are presented.

This comparison was performed across four models (described above) of increasing complexity, ranging from a 2D configuration to a 3D setup. The models were progressively enhanced by incorporating FBs and bottom lateral bracing, while the representation of the TB transitioned from exclusively beam elements to a combination of beam and shell elements. This approach was intended to evaluate how the introduction of additional structural components and a more detailed representation of the TB affected the results.

The analysis revealed that the tension in the TB decreased in the 3D models due to the addition of bottom lateral bracing and FBs, which effectively redistributed the applied loads, thereby reducing the tension in the TB. The close agreement of the model results with the design plan values provides confidence in the models' accuracy, even as their complexity increased.



Source: FHWA

**Figure 9. Graph. Dead load moment in the TB for different FE models.**

**Table 4. Hanger forces in different models of Birmingham Bridge (kips)**

Hanger	Design Plans (kip)	2D model – all beams (kip)	2D model – 6 TB segments as shells (kip)	3D model – all beams (kip)	3D model – 6 TB segments as shells (kip)	3D model – all shells (kip)
L1U1	413	547	545	546	546	534
L2U2	460	440	441	439	441	424
L3U3	473	426	428	426	429	412
L4U4	476	428	430	428	431	414
L5U5	476	431	434	432	435	418
L6U6	477	434	437	434	437	421
L7U7	477	436	439	436	439	423
L8U8	478	438	441	439	441	425
L9U9	481	440	443	440	443	427
L10U10	481	441	444	441	444	428

### 4.2.3 Live load analysis

Once the Birmingham Bridge's Abaqus models were progressively developed as 3D models with TBs modeled as shell elements and successfully benchmarked against design plan values for dead loads, the next logical step was to introduce live loads. This phase involved applying lane and truck loads to the models to simulate live loading conditions on the bridge. The load from the deck and stringer beams was systematically transferred to the FBs and applied at their top flange.

In accordance with LRFD (11) Article 3.6.1.1.1, the Birmingham Bridge can accommodate eight design lanes. To maximize the live load effect, eight HL-93 design vehicular loads were positioned side by side, representing full lane utilization. This configuration ensures that the bridge experiences the most critical loading scenario, providing a robust assessment of its structural performance. Two distinct truck load scenarios were considered:

- *Trucks placed at quarter span:* This scenario was used to assess the effects of eccentric loading, which may cause uneven stress distribution in the bridge components. For this scenario, the truck load was applied to the FBs at section points L4, L5 and L6 (Figure 8).
- *Trucks placed at midspan:* This scenario was used to simulate the maximum bending effects in the bridge, as midspan is typically the region of highest bending moments. For this loading case, the FBs at section points L9, L10 and L11 as can be seen in Figure 8 were loaded with the truck loads.

Lane loads for both end and intermediate FBs were separately calculated and applied to the top flange of the FBs. The multiple presence factor ( $m$ ), specified in LRFD (8) Table 3.6.1.1.2-1, was set to 0.65, reflecting the simultaneous presence of eight lanes. This factor accounts for the reduced probability of all lanes being fully loaded simultaneously while maintaining an accurate representation of traffic conditions.

All loads were further factored using the Redundancy-2 multipliers outlined in Table 1.7.1-1 of the IRM Guide Spec. (6). Additionally, while a dynamic load allowance of 15% was considered to account for the dynamic effects of moving vehicles, this factor was not applied to the design lane load, maintaining consistency with the LRFD methodology.

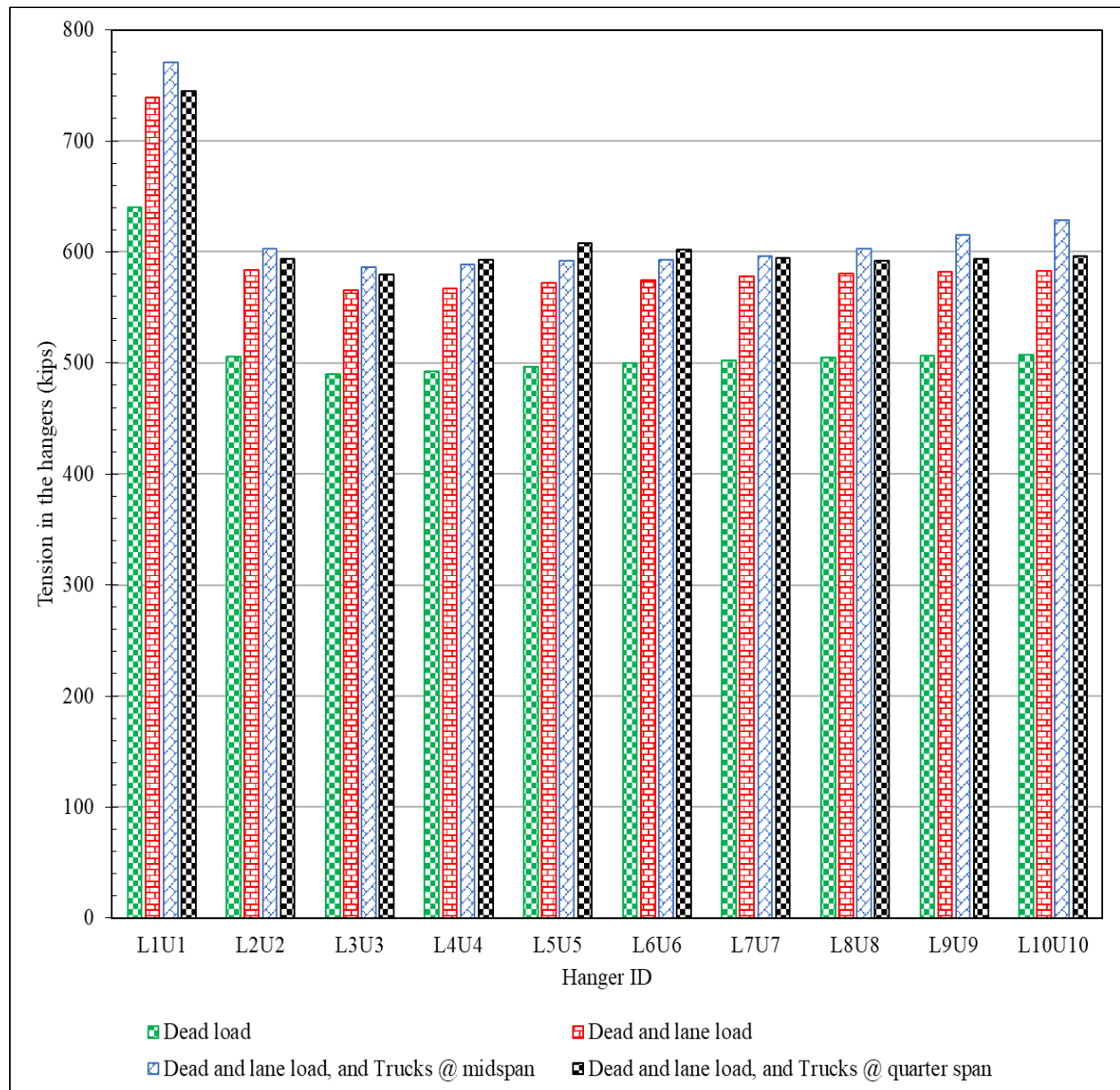
### 4.2.4 Change in the global forces under the live load

Under the applied dead, lane, and truck loads, the bridge was analyzed for hanger and TB tension, vertical deflection, and bending moment in the TB. The hanger forces on one side of the bridge's centerline are shown in the Figure 10. It is important to note that the trucks were positioned either at the quarter span or at midspan, but not simultaneously at both locations. As shown in Figure 10, the hanger forces are primarily governed by the dead load, with an increase of approximately 80 kips due to the lane load. The truck load only affected the hanger located at the section where the FBs were directly loaded by the truck.

Similar to the hanger forces, the tension in the TB was also primarily due to the dead load. The contribution from live loads was relatively smaller, with the lane load increasing the TB tension by approximately 600 kips and the HL-93 truck load adding an additional 200 kips.



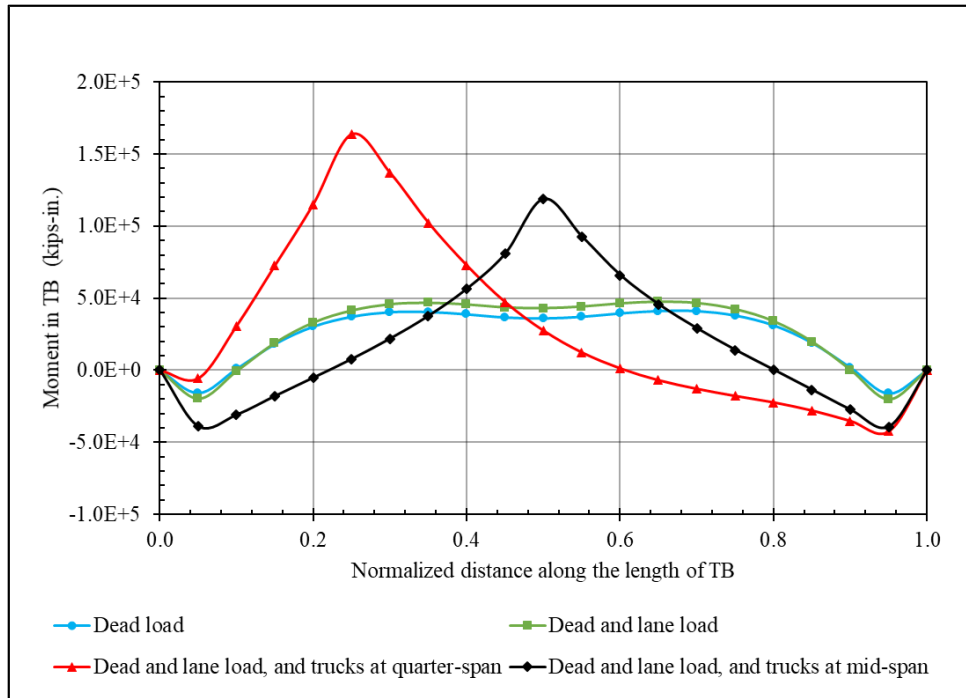
The resulting TB bending moments under these combined load cases are presented in Figure 11. As observed, the inclusion of lane loads elevated the existing dead load moments across the TB. However, the placement of the trucks not only significantly increased the magnitude of the maximum moment but also altered the location of the inflection point and changed the overall deflected shape of the TB. These effects are further confirmed by the vertical deflection profiles as presented in Figure 12, which show noticeable differences in the TB response depending on the truck position. It is important to note that, unlike the hanger forces and TB tension which were only slightly influenced by the truck load, the TB moment increased significantly due to it.



Source: FHWA

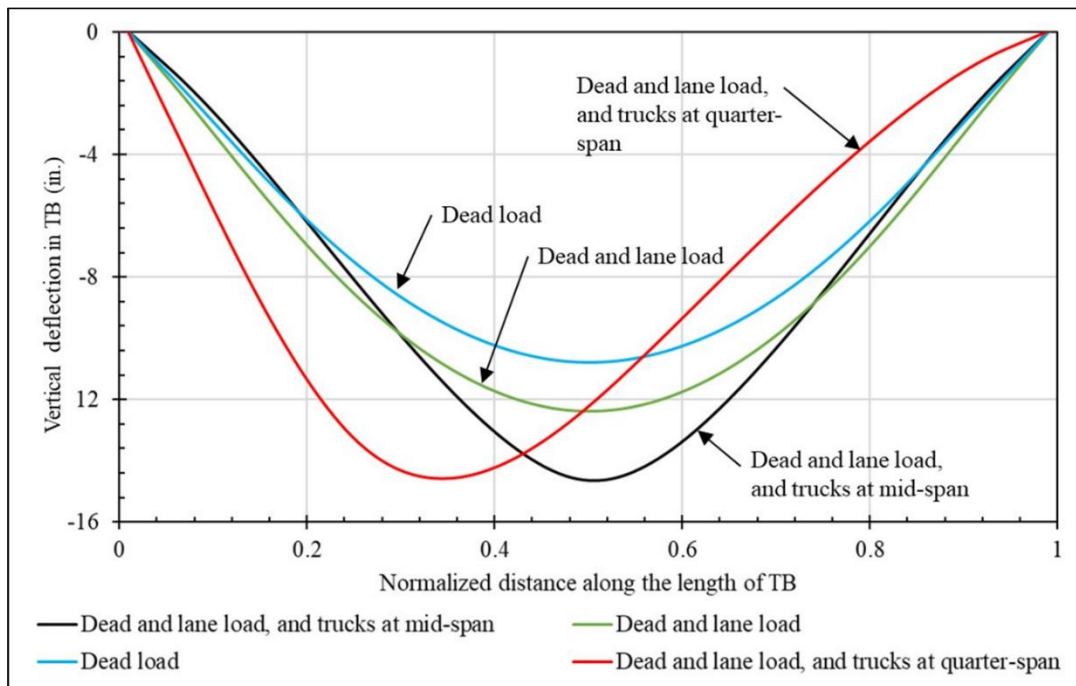
**Figure 10. Graph. Tension in the hanger under different loading conditions.**





Source: FHWA

**Figure 11. Graph. Bending moment in the TB under different loading conditions.**

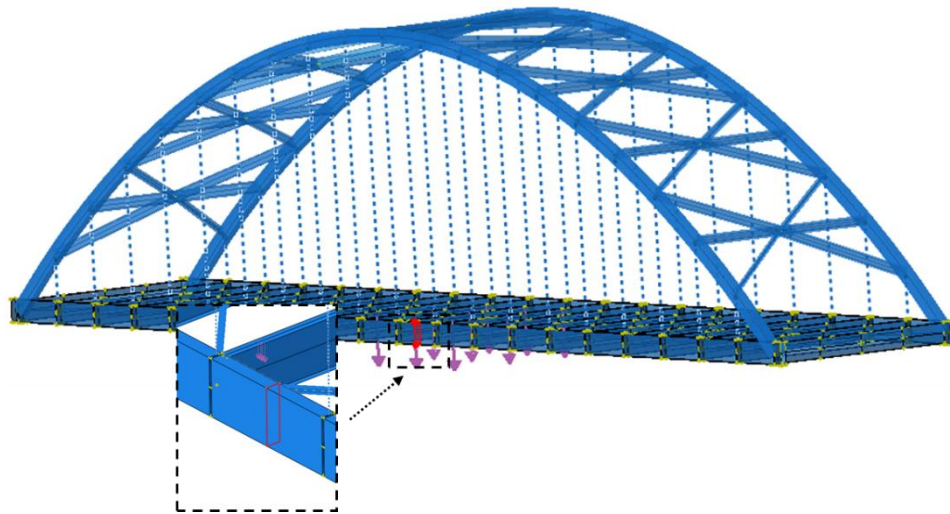


Source: FHWA

**Figure 12. Graph. Vertical deflection in TB under different loading conditions.**

#### 4.2.5 Longitudinal stress in the component plates of TB

To further investigate the stress behavior of the TB under different loading conditions, the longitudinal stress component (S11) was evaluated for component plates of the TB at the midspan between the FB connections, as indicated by the red box in Figure 13. The corresponding stress distributions for dead load only, dead plus lane load, and the combined case of dead, lane, and truck loads with the truck positioned at midspan are shown in Figure 14, Figure 15, and Figure 16, respectively.

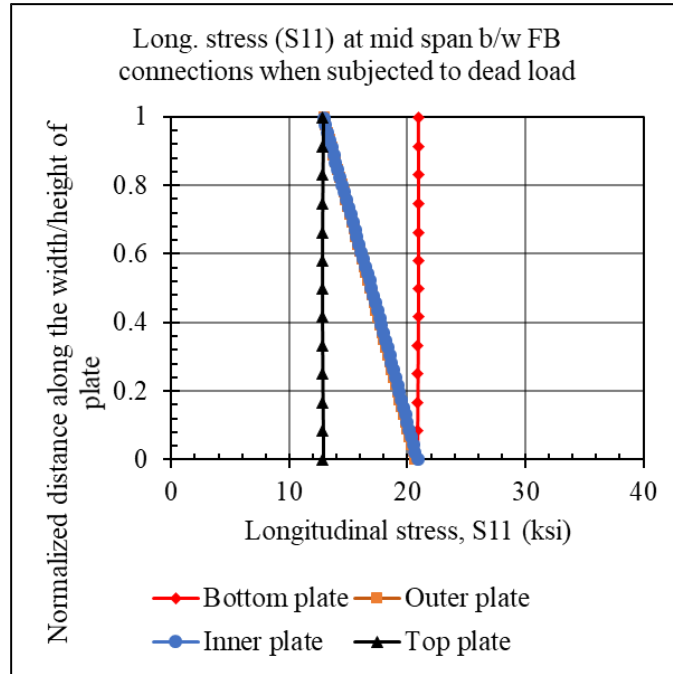


Source: FHWA

**Figure 13. Graph. Tie beam location for stress evaluation when trucks are placed at midspan.**

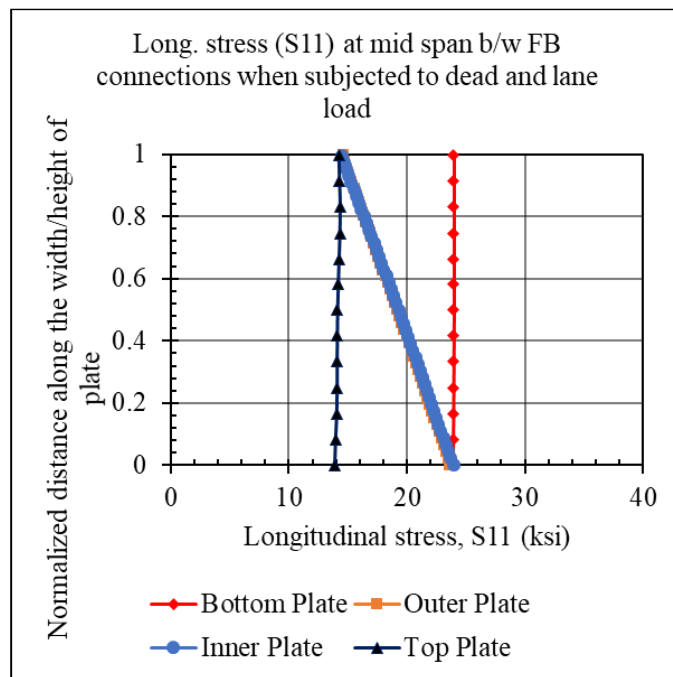
In all cases, the bottom and top plates primarily experienced uniform tensile stress, with the bottom plate showing higher tension due to its location relative to the neutral axis. The presence of bending caused a redistribution of stress, reducing the tensile stress in the top plate while increasing it in the bottom plate. The side plates, however, exhibited variations in stress that reflect bending effects. For all the plots, an important observation is that the longitudinal stress profiles in both the inner and outer plates were nearly identical. This suggests a symmetric response under the applied loads and indicates the absence of significant transverse shear effects or out of plane deformation in the evaluated region.

The magnitude of the bending stress varied significantly with the type of applied load. Under dead load alone, the bending stress in the side plates was approximately 4 ksi. This increased to around 5 ksi with the addition of lane loads. However, when truck loads were introduced, the bending stress increased markedly to nearly 11 ksi at the truck location. As the truck load dominated the bending stress, the dead and lane load caused the significant proportion of the tension in the TB as mentioned in previous sections. This is evident when comparing Figure 14, Figure 15, and Figure 16, which show that tensile stresses are more prominent than bending effects under both dead and lane loads. These findings emphasize that the TB response is primarily tension-driven under distributed loading, while localized bending becomes significant with the application of concentrated truck loads, leading to a substantial increase in flexural stresses in certain regions.



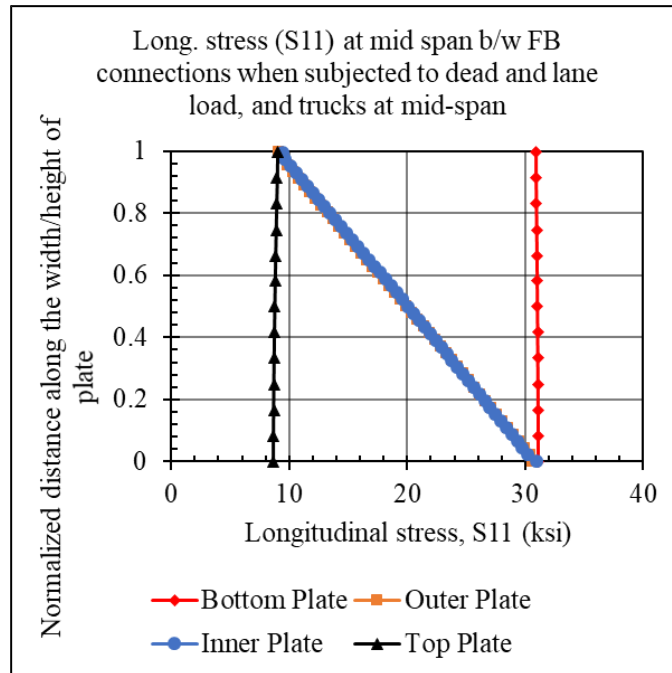
Source: FHWA

**Figure 14. Graph. Longitudinal stress (S11) at mid span between FB connections when Birmingham Bridge is subjected to dead load.**



Source: FHWA

**Figure 15. Graph. Longitudinal stress (S11) at mid span between FB connections when Birmingham Bridge is subjected to dead and lane load.**



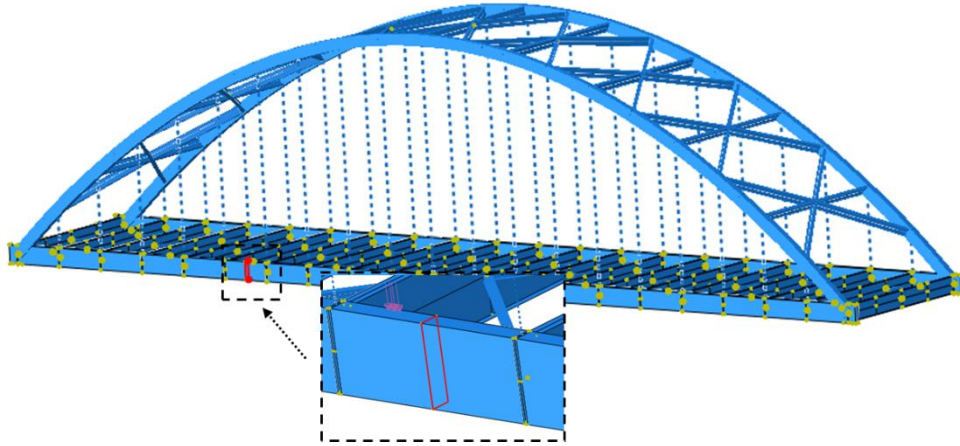
Source: FHWA

**Figure 16. Graph. Longitudinal stress (S11) at midspan between FB connections when Birmingham Bridge is subjected to dead and lane load, and trucks at mid-span.**

To further validate these observations, stress plots were also generated for the case where the trucks were placed at the quarter span, as shown by the red box in Figure 17. The overall stress behavior of the TB under different loading conditions remains consistent with the midspan loading scenario. As with the midspan case, the bottom and top plates primarily exhibited uniform tensile stresses, while the side plates experienced bending.

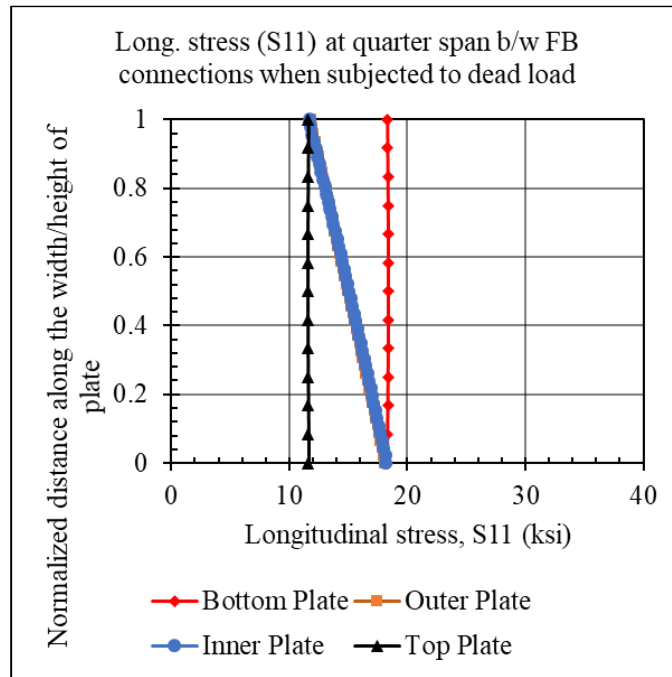
Under dead load as shown in Figure 18, the bending stress in the side plates was approximately 4 ksi, and it increased slightly with the addition of lane loads (Figure 19). However, when truck loads were applied at the quarter span, the bending stress rose significantly to approximately 12.5 ksi as calculated from the Figure 20. This increase is notably higher than that observed in the midspan truck loading case where this value was 11 ksi.

This high bending stress was expected and aligns with the global response trends observed earlier. Specifically, the bending moment diagram presented in Figure 11 show that placing the truck at the quarter span induces higher bending moments compared to the midspan scenario. This directly translates to increased flexural demand and, consequently, higher bending stresses in the TB at the quarter span location.



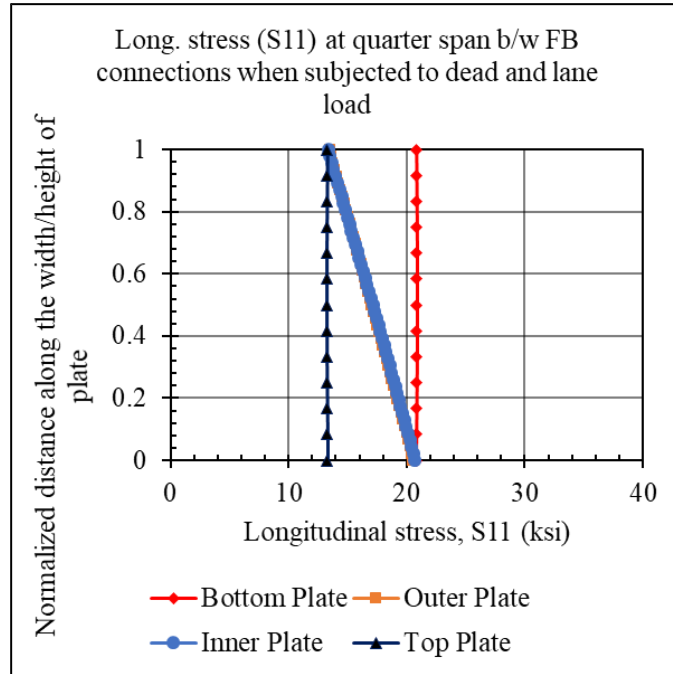
Source: FHWA

**Figure 17. Illustration. TB location for stress evaluation when trucks are placed at quarter-span,**



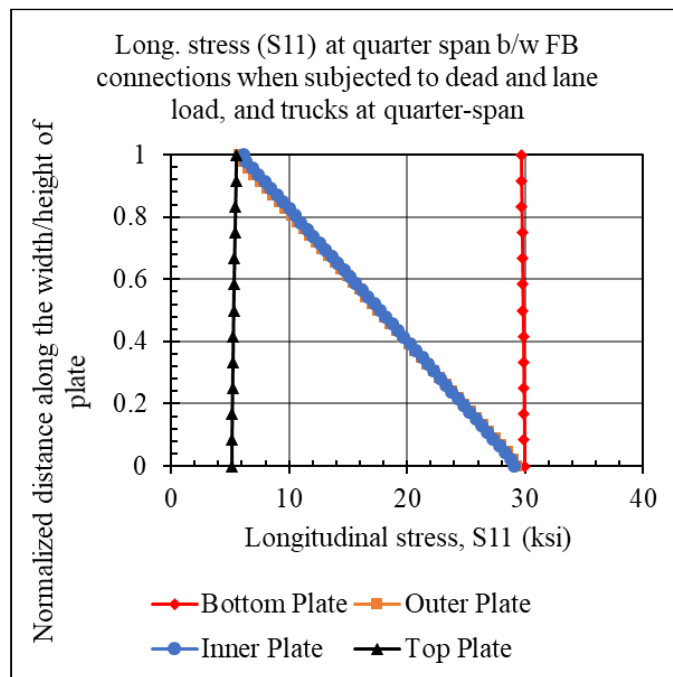
Source: FHWA

**Figure 18. Graph. Longitudinal stress (S11) at quarter span between FB connections when Birmingham Bridge is subjected to dead load.**



Source: FHWA

**Figure 19. Graph. Longitudinal stress (S11) at quarter span between FB connections when Birmingham Bridge is subjected to dead and lane load.**



Source: FHWA

**Figure 20. Graph. Longitudinal stress (S11) at quarter span between FB connections when Birmingham Bridge is subjected to dead and lane load, and trucks at mid-span.**

In addition to the regions between the FB connections, longitudinal stress values were also evaluated directly at the FB locations for both midspan and quarter-span truck loading cases.

These analyses revealed consistent stress trends and confirmed the uniformity of the TB response across different regions of the span.

The key findings from the load analysis can be summarized as follows: the hanger forces and axial tension in the TB are primarily governed by the dead load, with the lane load contributing slightly and the truck load only marginally to these values. In contrast, the truck load significantly influences the structural response by altering the deflected shape, increasing the bending moment demand, and amplifying the flexural stresses in the TB. It was also observed that the vertical inner and outer side plates of the TB experience nearly identical longitudinal stresses, indicating symmetric behavior and the absence of significant transverse effects. Among the horizontal plates, the bottom plate was found to be more critical, as it consistently exhibited higher tensile stresses than the top plate. Overall, these findings align with expectations from the global bridge model and provide a comprehensive understanding of the TB's behavior under combined dead and live loading conditions. They also instill confidence in the accuracy of the developed model and support its continued use for subsequent fracture studies.

### **4.3 GLOBAL RESPONSE OF BIRMINGHAM BRIDGE IN FAULTED CONDITION**

With the FE model of the Birmingham Bridge developed and validated against design plan values for dead load effects, including hanger forces, TB axial tension, and bending moments, the next stage involved the application of live loads as described in the previous section. These included both lane and discrete truck loads. It is important to note that truck loads were applied either at the quarter span or at midspan, but not at both locations simultaneously.

Once the bridge model was fully configured under these essential loading conditions, the analysis proceeded to evaluate the structural response to localized fractures within the TB. In the context of this report, a *localized fracture* refers to a complete failure of one of the component plates of a single box shaped TB. The bridge was reanalyzed under this fractured condition, and the resulting global responses, including TB axial tension, bending moments, hanger forces, and vertical deflections in the affected TB, were compared to the responses obtained from the intact condition. This comparison helps to assess the redundancy and force redistribution capacity of the bridge when damage is present in a primary load-carrying member.

The following section discusses in detail the rationale behind the selection of fracture locations, the specific components where fractures were introduced, and the global response parameters recorded to evaluate the impact of each simulated fracture. It is important to mention that, while some descriptions or figures may focus on the effects of truck placement, it should be clearly understood that whenever truck loads are applied, the bridge is always subjected to both dead and lane loads.

#### **4.3.1 Fracture scenarios**

TBs in tied arch bridges are typically constructed as built-up box girders. The objective of the initial fracture simulations was to investigate whether localized fractures in individual TB components significantly affect the internal force distribution, not only within the fractured TB but also in other key structural elements such as the hangers and the intact portions of the TB. If

the global distribution remains largely unchanged in the presence of such fractures, it may not be necessary to model the entire bridge system when evaluating the internal redundancy of a TB.

As discussed earlier, the placement of truck loads at either the quarter span or the midspan changes the deflected shape of the bridge and significantly alters the moment demand. To better understand the behavior of the Birmingham Bridge under fractured conditions, TB fractures were simulated independently under both truck loading scenarios, with trucks placed at the quarter span and then at midspan.

For each truck load scenario, two specific fracture locations along the TB were selected for evaluation. These include the region adjacent to an FB connection and the region located between two FB connections. Fractures near FB connections are important to study because these areas are subject to localized force concentrations where the FBs transfer loads into the TB. On the other hand, the regions between FBs experience different force distributions and are generally less stiff due to the absence of direct lateral support and the influence of hanger forces. These regions also typically experience higher moment demands. As such, these two locations exhibit distinct structural behaviors and are essential for evaluating the internal redundancy of the tied arch bridge under realistic loading and damage conditions.

For each truck load scenario (midspan or quarter span) and at each of the two selected fracture locations (adjacent to an FB or between FBs), two distinct fracture configurations, namely bottom plate fracture and side plate fracture, were modeled. This resulted in a total of eight fracture cases. The primary objective of this investigation was to evaluate whether the presence of these fractures leads to significant redistribution of internal forces, particularly increases in axial force or bending moment demands in the TB or other components of the bridge.

It is important to emphasize that this study does not aim to capture highly localized stress concentrations at the crack tips. Rather, the focus is on assessing the broader influence of a fractured TB on the global structural behavior and internal force distribution across the bridge system. The two fracture configurations evaluated at each fracture location under both truck load scenarios are summarized below:

- **Complete fracture of the bottom plate**, for the Birmingham Bridge, representing approximately 18.35% of the TB cross sectional area  
*Rationale:* Complete separation of a bottom or top plate is a plausible failure scenario, considering typical fabrication practices and in-service performance.
- **Complete fracture of one entire side plate**, for the Birmingham Bridge, accounting for approximately 31.65% of the TB cross sectional area  
*Rationale:* A full fracture of a side plate represents a realistic damage case that could significantly reduce lateral stiffness and alter the internal force flow within the TB.

The fracture studies were conducted on the Birmingham Bridge model presented in Figure 8. The Abaqus model also considered the non-linear geometry effects due to large plastic deformations. The fracture scenarios were simulated by selectively removing elements from the TB section corresponding to either the bottom plate or the outer side plate, depending on the



specific fracture case being evaluated. This method allowed for the representation of a crack-like geometry while maintaining consistency across all cases. For the midspan truck load scenario, the "between FBs" fracture was modeled by removing elements from the TB section located between section points L10 and L11. In the "at FB" configuration under the same loading condition, the fracture was introduced at a location six inches away from section point L10. Similarly, for the quarter span truck load scenario, the "between FBs" fracture was applied between section points L5 and L6. In the "at FB" case for this loading condition, the fracture was introduced at a point six inches away from section point L5. These modeling strategies provided a consistent and localized simulation of component-level damage, enabling the evaluation of how such fractures affect global force redistribution and the overall structural behavior of the bridge.

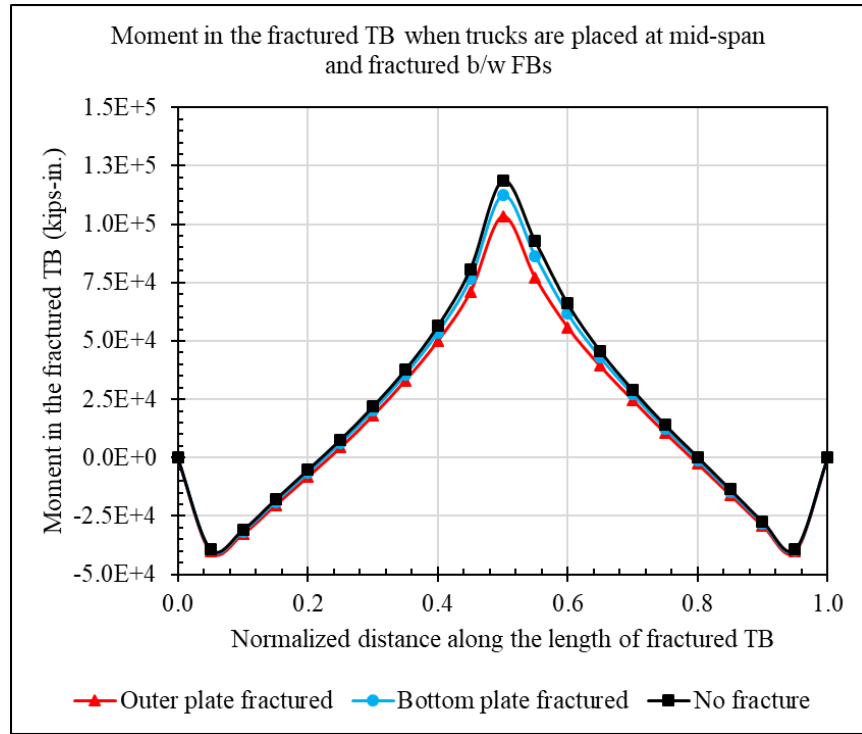
#### **4.3.2 Effect of simulated fractures**

Following the simulated fracture scenarios described earlier, the structural response of the Birmingham Bridge was evaluated and compared to the unfaulted condition. The primary goal of this analysis was to assess whether a localized fracture in a component plate of the TB causes significant changes in the global force distribution across the bridge.

For the midspan truck load scenario with a fracture located between the FBs, the moment distribution along the length of the fractured TB is shown in Figure 21. The results indicate that the complete fracture of the bottom plate led to a maximum reduction in bending moment of approximately 4% near the location of the fracture. In the case of the outer (or a side) plate fracture, the maximum observed difference was about 5%. However, these deviations were limited to the region close to the fracture. Elsewhere along the TB, the moment profiles closely followed those of the intact condition. Given that the maximum moment in the unfractured TB under this load scenario was approximately 118,778 kip-inches, these percentage differences represent only minor changes in structural response.

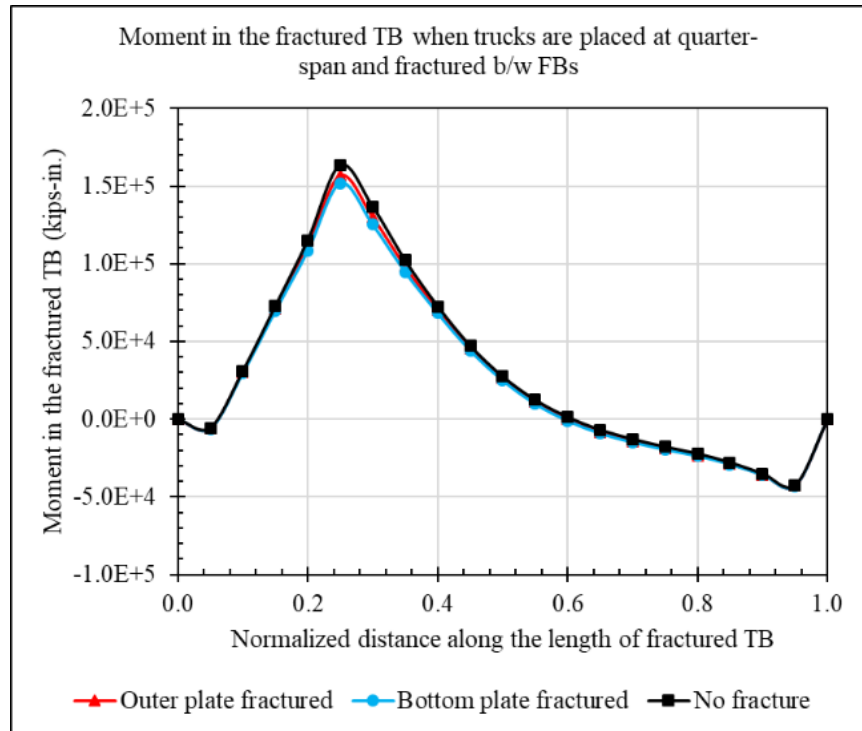
The moment profile for the quarter span truck load condition, shown in Figure 22, exhibited similar trends. The bottom plate fracture again caused a slight reduction in moment values, especially near the fractured region. The outer plate fracture had an even smaller impact, resulting in negligible deviation from the unfractured condition. Overall, the shape and magnitude of the bending moment diagrams remained largely unchanged. This confirms that the bending behavior of the TB is not significantly affected by the loss of a single component plate when evaluated at the system level.

Table 5 and Table 6 present the axial tension in the TB's section points for both midspan and quarter span truck load scenarios. Across the entire length of the TB, the variation in axial force due to the simulated fractures remained below 0.5%. This suggests that the redistribution of axial forces is minimal, even under complete fracture of a plate. The low sensitivity in axial tension can be attributed to the internal redundancy and continuity of the remaining (or intact) plate elements, which redistribute the load among themselves and continue to perform effectively.



Source: FHWA

**Figure 21. Graph. Moment in the fractured TB when trucks are placed at mid-span and fractured between FBs.**



Source: FHWA

**Figure 22. Graph. Moment in the fractured TB when trucks are placed at quarter-span and fractured between FBs.**

**Table 5. Difference (%) in the axial force of fractured TB when trucks are placed at mid-span**

<b>Section point</b>	<b>Percentage difference, bottom plate fractured</b>	<b>Percentage difference, outer plate fractured</b>
L1	0.02	0.07
L2	0.02	0.00
L3	0.02	0.05
L4	0.01	-0.01
L5	0.02	0.04
L6	0.01	-0.03
L7	0.02	0.03
L8	0.00	-0.06
L9	0.02	0.11
L10	-0.01	-0.07
L11	0.02	-0.04
L12	0.06	0.18
L13	0.02	0.03
L14	0.05	0.10
L15	0.03	0.04
L16	0.04	0.12
L17	0.03	0.06
L18	0.04	0.13
L19	0.03	0.07

**Table 6. Difference (%) in the axial force of fractured TB when trucks are placed at quarter-span**

<b>Section point</b>	<b>Percentage difference, bottom plate fractured</b>	<b>Percentage difference, outer plate fractured</b>
L1	0.09	0.03
L2	0.00	0.00
L3	0.07	0.01
L4	-0.03	0.08
L5	0.02	0.09
L6	0.03	0.06
L7	0.05	0.08
L8	0.04	0.02
L9	0.04	0.02
L10	0.02	0.03
L11	0.04	0.02
L12	0.01	0.04
L13	0.03	0.02
L14	0.00	0.03
L15	0.02	0.02
L16	-0.01	0.03
L17	0.01	0.02
L18	-0.02	0.03
L19	0.01	0.02

The influence of fractures on hanger forces was also investigated, as shown in Table 7 and Table 8. In general, changes in hanger tension were small and limited to the hangers located near the fractured region. The maximum observed change was 12 kips, which occurred in the bottom plate fracture case under the quarter span truck load condition. This change corresponds to approximately a 2% difference from the unfaulted condition. All other fractured scenarios showed smaller deviations. The relatively minor effect on hanger forces reinforces the conclusion that global force paths within the bridge remain intact and functional, even in the presence of localized damage.

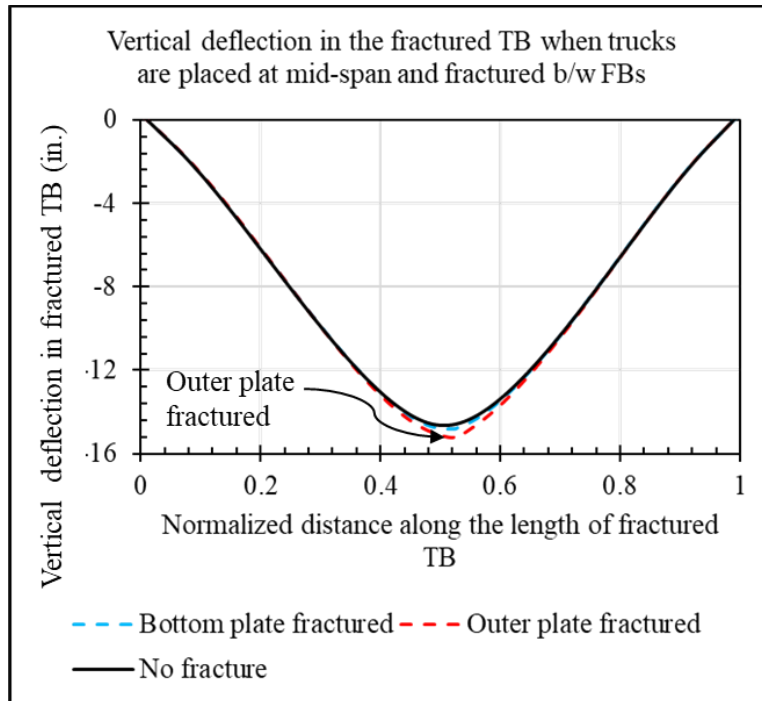
**Table 7. Difference (%) in the hanger forces connected to the fractured TB when trucks are placed at mid-span**

<b>Hanger ID</b>	<b>Percentage difference, bottom plate fractured</b>	<b>Percentage difference, outer plate fractured</b>
L1U1	0.06	-0.06
L2U2	0.04	-0.04
L3U3	0.05	-0.06
L4U4	0.05	-0.07
L5U5	0.03	-0.04
L6U6	-0.05	0.07
L7U7	-0.19	0.28
L8U8	-0.33	0.48
L9U9	-0.20	0.31
L10U10	0.78	-1.04
L11U11	0.84	-1.20
L12U12	-0.17	0.24
L13U13	-0.33	0.48
L14U14	-0.20	0.30
L15U15	-0.06	0.09
L16U16	0.03	-0.03
L17U17	0.05	-0.06
L18U18	0.05	-0.04
L19U19	0.06	-0.05

**Table 8. Difference (%) in the hanger forces connected to the fractured TB when trucks are placed at quarter-span**

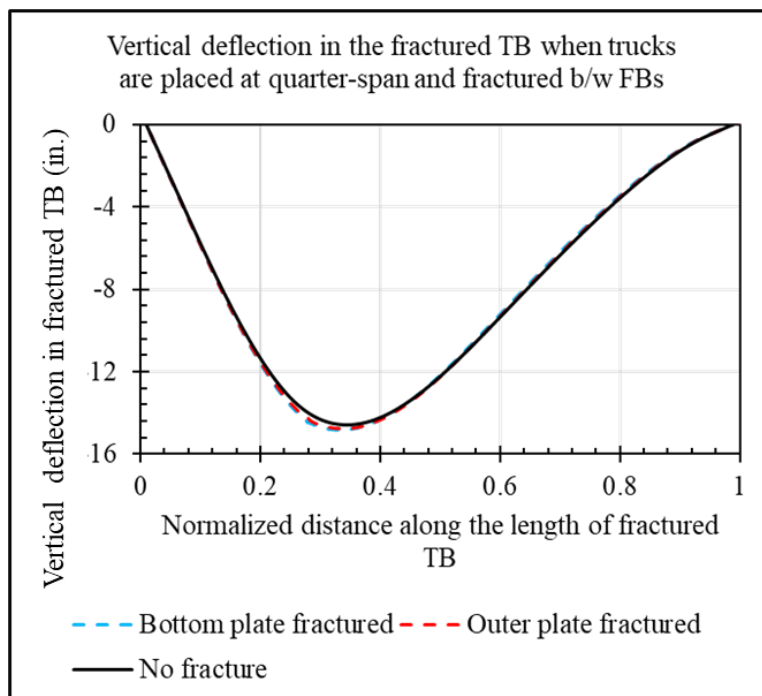
<b>Hanger ID</b>	<b>Percentage difference, bottom plate fractured</b>	<b>Percentage difference, outer plate fractured</b>
L1U1	-0.10	-0.10
L2U2	-0.58	-0.36
L3U3	-0.91	-0.54
L4U4	-0.43	-0.27
L5U5	1.97	1.11
L6U6	1.67	0.97
L7U7	-0.46	-0.27
L8U8	-0.69	-0.41
L9U9	-0.39	-0.23
L10U10	-0.11	-0.07
L11U11	0.04	0.02
L12U12	0.09	0.05
L13U13	0.08	0.05
L14U14	0.06	0.04
L15U15	0.05	0.03
L16U16	0.04	0.03
L17U17	0.04	0.03
L18U18	0.04	0.03
L19U19	0.06	0.05

In addition to moments, axial forces, and hanger tensions, vertical deflections of the TB were also analyzed to assess the influence of localized fractures on global stiffness. Figure 23 and Figure 24 present the vertical deflection profiles for the midspan and quarter span truck load scenarios, respectively. In both cases, the TB exhibited slightly larger deflections in the fractured condition compared to the unfractured state. This increase in the deflection can be attributed to the localized loss of stiffness in the TB due to the absence of a full plate section. The fractured region becomes softer, resulting in reduced flexural rigidity and slightly greater deformation under the same loading conditions. However, these differences in deflection remain localized and small in magnitude. The overall deflected shape and global displacement pattern of the TB remained nearly identical to that of the intact condition.



Source: FHWA

**Figure 23. Graph. Vertical deflection in the fractured TB when trucks are placed at mid-span and fractured between FBs.**



Source: FHWA

**Figure 24. Graph. Vertical deflection in the fractured TB when trucks are placed at quarter-span and fractured between FBs.**

Although the results discussed here pertain to fracture scenarios located between FBs, identical trends were observed for cases where the fracture was located directly at the FB connection. Therefore, the conclusions drawn regarding bending moments, axial tension, hanger forces, and deflections apply consistently across both fractured locations and for both truck load scenarios. It is also important to note that the results discussed above are for faulted TB where a fracture was simulated and analyzed. The model showed that no changes occurred in the unfaulted TB.

In summary, the results of the Birmingham Bridge simulations demonstrate that while localized fractures in individual TB components do affect local stress distribution and slightly influence deflection, they do not significantly alter the global structural behavior. The internal force redistribution remains limited, and the performance of the bridge system as a whole is largely preserved. This validates the approach of using localized TB models rather than simulating the entire bridge when evaluating the effects of component-level damage. By applying the pre-fracture force state to a simplified TB segment, the redistribution of forces can be studied effectively. This methodology greatly simplifies the process for future parametric studies.

#### **4.4 ARKANSAS WHITE RIVER (AWR) BRIDGE**

The Birmingham Bridge, with a TB depth of 11 feet 6 inches, is classified for the sake of this report as having a “large” or deep TB, using a threshold depth of approximately 8 feet to distinguish between deep and shallow TBs. As discussed in the preceding sections, the simulated component fractures in the TB of the Birmingham bridge did not significantly impact global structural behavior. The changes in axial force and bending moment in the fractured TB due to localized fractures were minimal, and only negligible differences were observed in the hanger forces and overall force distribution between the faulted and unfaulted TB conditions. To assess whether TB depth influences the global response of tied arch bridges under localized TB component fractures, a second case study was conducted on the Arkansas White River (AWR) Bridge, which features a small TB with a depth of 5 feet 3 inches. The following section presents the analysis and findings for the AWR bridge to determine whether the reduced TB depth leads to any meaningful differences in global behavior compared to the Birmingham Bridge.

The AWR, constructed in 1970, spans over AR-38 in Des Arc in Prairie County, Arkansas. It is a tied arch bridge with a main span length of 420 feet and an arch rise of 75 feet, 6 inches at the centerline. The bridge includes multiple plate-girder approach spans on both ends and was designed in accordance with the 1965 AASHTO specifications, using ASTM A36 and A441 steels.

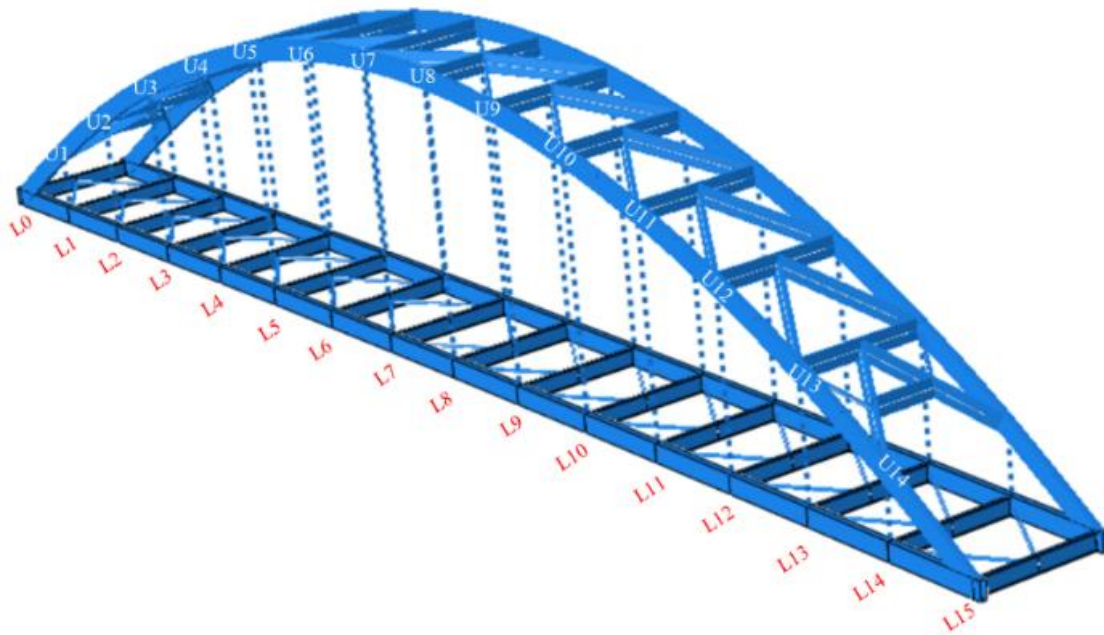
The superstructure features vertical hangers composed of box-shaped sections spaced at regular intervals of 28 feet. The two TBs are spaced 35 feet apart (center-to-center), providing a clear roadway width of 30 feet, sufficient for two traffic lanes. A V-type wind bracing system is employed to enhance lateral stability and resist out-of-plane buckling. The arch ribs are constructed as 5 feet deep welded built-up box girders, while the TBs consist of similarly welded built-up steel box sections with a depth of 5 feet 3 inches.



#### 4.4.1 FE model of AWR bridge

Consistent with the approach used for the Birmingham Bridge, the FE analysis for AWR Bridge began with the development of a 2D model to verify structural behavior against design drawing values, focusing on TB and hanger forces. Two models were created using beam elements: the first was a 2D model consisting of a single arch and TB, where the arch and TB were modeled using beam elements and the hangers were represented by connector elements. The second model was a 3D configuration that additionally incorporated FBs, along with bottom and top lateral bracing members. Both models used B32 elements, which are 3-node beams with quadratic interpolation.

Although this modeling approach had already demonstrated reliability in the previous case, it was repeated for the AWR bridge to ensure consistency and allow a direct comparison between bridges with deep and shallow TBs. After the 2D models, a 3D hybrid model combining shell and beam elements was developed. In this configuration, TBs and FBs were modeled using shell elements, while the arches and lateral bracing members were represented using B32 beam elements. Shell elements were selected for the TBs to enable the simulation of localized fractures through seam definition or element deactivation, which is not feasible with beam elements. Shell elements of type S8R, which are 8-node elements with reduced integration, were used for this purpose. The final Abaqus model is shown in Figure 25, where the panel points indicate the locations of FBs and hangers along the TB.



Source: FHWA

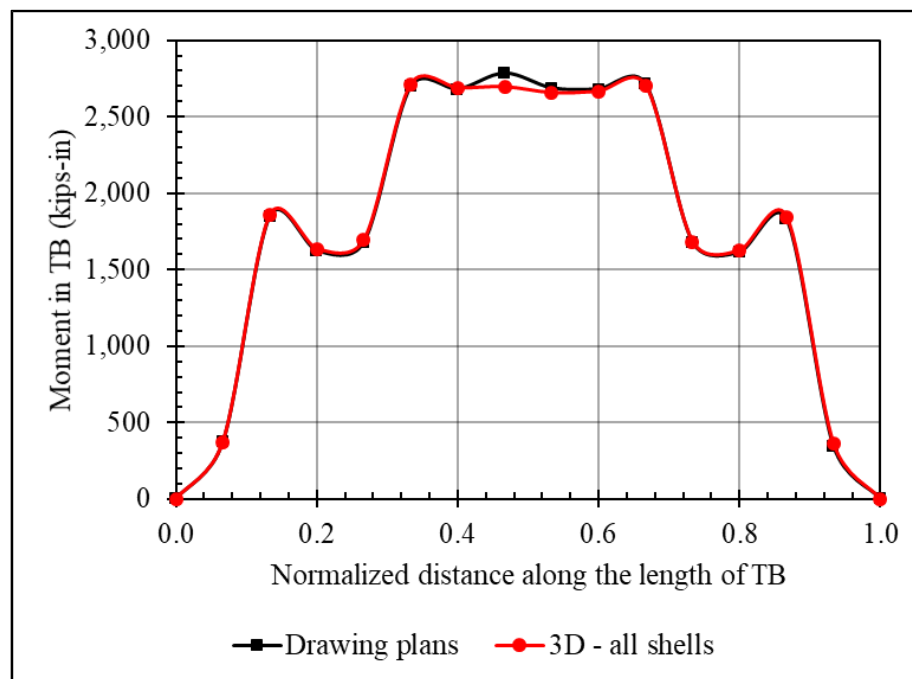
**Figure 25. Illustration. 3D model of AWR bridge**

#### 4.4.2 Dead load analysis

The final 3D model was analyzed under gravity loads, where the dead load from the deck and stringers was directly applied as a uniformly distributed load on the top flange of the FBs. For all

modeled members, Abaqus internally calculated the self-weight based on the cross-sectional properties and material densities.

A comparison of dead load effects was conducted for axial tension, bending moment in the TB, and hanger forces, all of which showed reasonable agreement with the design plan values. Figure 26 presents the comparison of dead load bending moments, where the FE results (red line) closely align with the design drawing values (black line). The axial tension in the TB due to dead load, as predicted by the FE model, was 1,094 kips, which is approximately 2.8% higher than the 1,064 kips reported in the design plans. This close agreement confirms the validity of the FE model for subsequent analysis.



Source: FHWA

**Figure 26. Graph. Comparison of FE and design plan dead load moments in TB of AWR Bridge.**

#### 4.4.3 Live load analysis

Once the 3D model (Figure 25) of the AWR bridge models was successfully benchmarked against design plan values under dead load, the next step was to introduce live load conditions. This phase involved the application of both lane and truck loads to simulate live loading. The load from the deck and stringer beams was systematically transferred to the FBs and applied as a uniformly distributed load to their top flanges.

In accordance with the AASHTO LRFD BDS (11), Article 3.6.1.1.1, the AWR bridge is designed to accommodate two traffic lanes. To maximize the live load effect, two HL-93 design vehicular loads were positioned side by side across the deck width. Two distinct truck load scenarios were considered, similar to the approach adopted for the Birmingham Bridge. In the first scenario, trucks were placed at the quarter span to assess the effects of eccentric loading, which can lead to localized stress concentrations and uneven force distribution within the

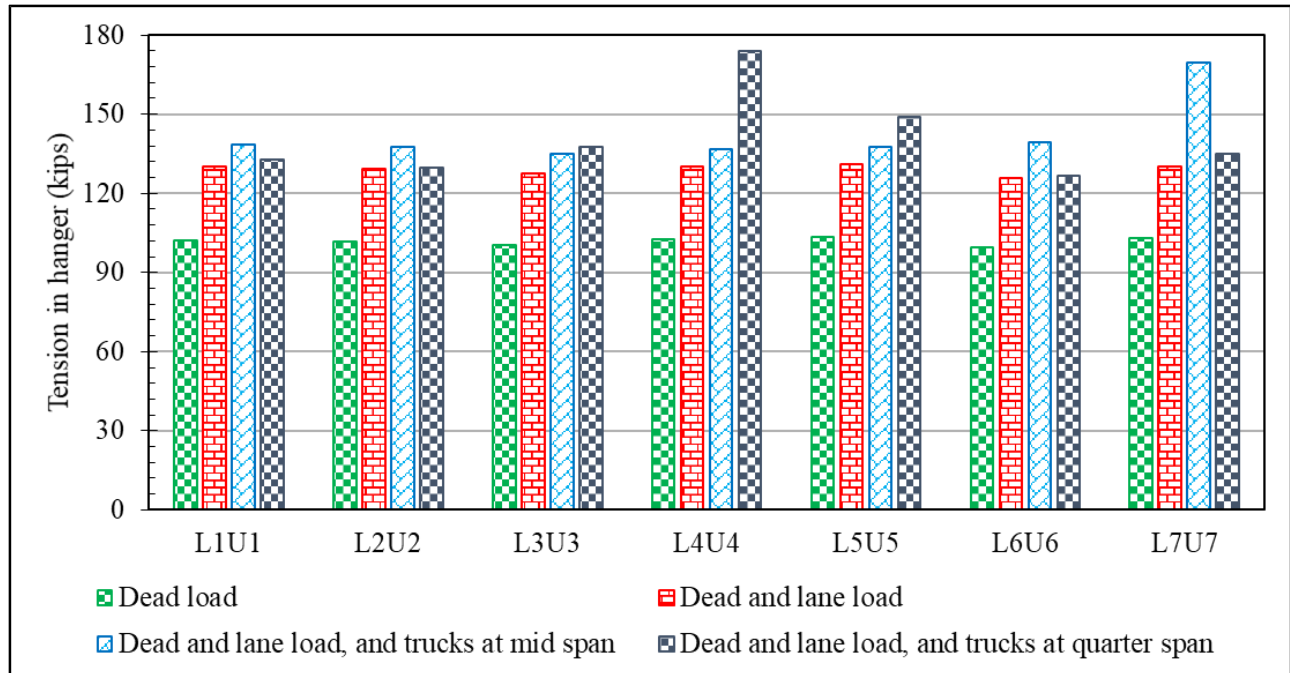
structure. In the second scenario, trucks were positioned at the midspan to evaluate maximum bending effects, as the midspan is typically the region most susceptible to high bending moments in tied arch bridges. To evaluate these effects, trucks were positioned over specific FBs in the model. For the midspan loading case, the FBs at panel points L6, L7, and L8 were loaded, while for the quarter-span scenario, the FBs at L3, L4, and L5 were loaded. These locations correspond to regions of high bending sensitivity in the span. These load cases provide a consistent basis for comparison with the Birmingham Bridge and help evaluate whether TB depth influences the global structural response under critical live loading conditions.

Lane loads for both external and internal FBs were calculated separately and applied at their top flanges. The multiple presence factor, as specified in the AASHTO LRFD BDS (11), Table 3.6.1.1.2-1, was taken as 1.0 to reflect the simultaneous presence of two loaded lanes. All loads were then factored using the Redundancy-II multipliers outlined in Table 1.7.1-1 of the IRM Guide Spec. (6). A dynamic load allowance (IM) of 15% was included to account for vehicle-induced dynamic effects, though this was not applied to the design lane load, in accordance with the AASHTO LRFD BDS.

#### **4.4.4 Change in the global response under live load**

The bearing reaction increased from 884 kips under dead load to 1,175 kips with the inclusion of lane and truck loads, reflecting a 33% increase. This trend closely mirrors the increase in axial tension in the TB, which rose from 1,214 kips under dead load alone to 1,495 kips with the addition of lane load, and further to 1,627 kips when truck loads were included. This represents an increase of approximately 23% due to the lane load and an additional 9% from the truck load. These results indicate that both the TB and the bearings are primarily influenced by dead loads, while live loads, particularly lane loading, contribute noticeably to the overall demand.

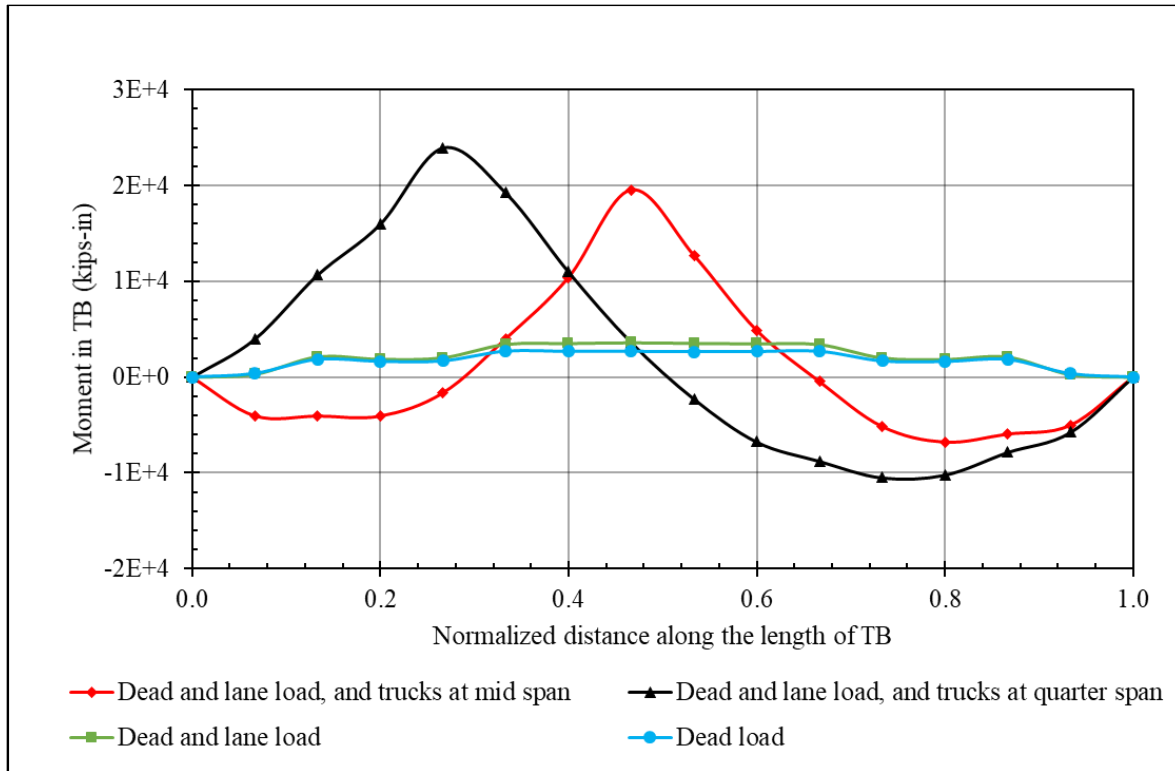
The hanger forces on one side of the bridge's centerline are shown in Figure 27. Truck loads were applied either at the quarter span or at the midspan, but not simultaneously at both locations. As illustrated in the figure, hanger forces are largely governed by the dead load, with the lane load contributing an increase of about 28 kips. The effect of truck loading was localized, primarily influencing the hanger positioned directly above the FBs where the truck loads were applied.



Source: FHWA

**Figure 27. Chart. Tension in hangers of AWR bridge under different loading conditions.**

The bending moment in the TB under combined dead, lane, and truck loads is presented in Figure 28. When dead and lane loads are applied, the TB experiences positive moment demand, but no negative moment regions are observed. However, the addition of truck loads results in the development of negative moment regions within TB. This behavior is primarily attributed to the concentrated and heavier nature of truck loads compared to the more uniformly distributed dead and lane loads. The configuration and positioning of the truck loads significantly influence the force distribution in the bridge. When trucks are placed at the quarter span or midspan, where the TB is more prone to bending, the resulting moments increase considerably. As shown in Figure 28, the lane load causes a moderate rise in positive moments without introducing negative moments. In contrast, truck loads substantially increase the overall moment and lead to the formation of negative moment regions. The red and black lines in Figure 28 represent the TB moment response when trucks are placed at the midspan and quarter span, respectively, in combination with dead and lane loads. The moment demand increases from 3,617 kip-inches under dead and lane loads to 19,512 kip-inches when trucks are placed at the midspan, and to 23,942 kip-inches when trucks are positioned at the quarter span. This significant increase highlights the critical influence of truck placement on TB behavior and reinforces the need to assess fracture scenarios under these high-demand conditions.

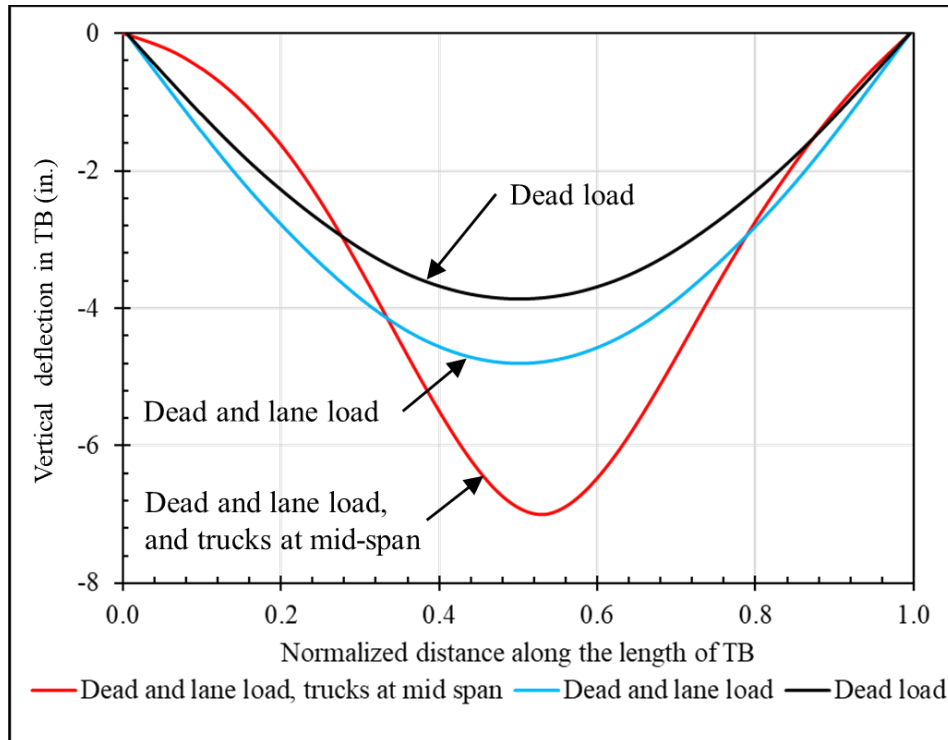


Source: FHWA

**Figure 28. Graph. Bending moment in TB of AWR bridge under different loading conditions.**

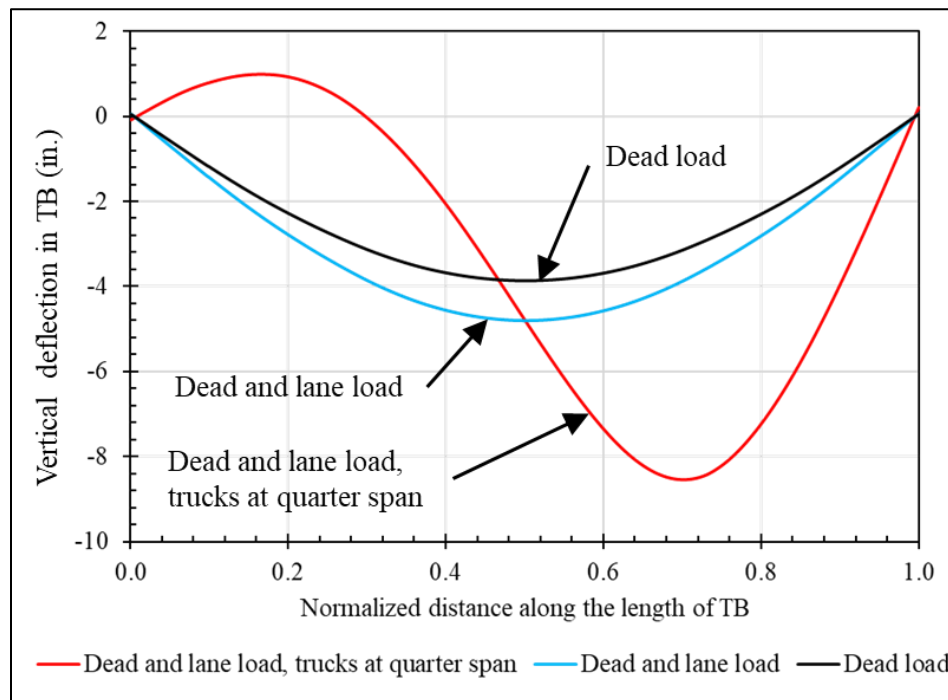
The vertical deflection of the TB under combined dead, lane, and truck loads is shown in Figure 29 and Figure 30. Similar to the bending moment behavior, the deflection response is strongly influenced by the position of the applied truck loads. While the addition of lane load to the dead load results in a moderate increase in deflection without significantly altering the deflected shape, the inclusion of truck loads leads to a pronounced change in both the magnitude and shape of the deflection curve. When trucks are placed at midspan (Figure 29), the maximum vertical deflection increases significantly compared to the dead and lane load case and occurs near the center of the span, as shown by the red curve. In contrast, when trucks are placed at the quarter span (Figure 30), the deflection profile becomes asymmetric, with increased displacement localized near the loaded region, as illustrated by the black curve. These shifts in deflection shape and magnitude highlight the sensitivity of the TB to the positioning of concentrated loads.

It is also important to note that while the hanger forces and TB tension experienced only localized or moderate changes due to truck loads, the TB deflection increased more significantly. This further underscore the critical impact of truck load positioning on the global response of the bridge.



Source: FHWA

**Figure 29. Graph. Vertical deflection in TB of AWR bridge under different loading conditions.**

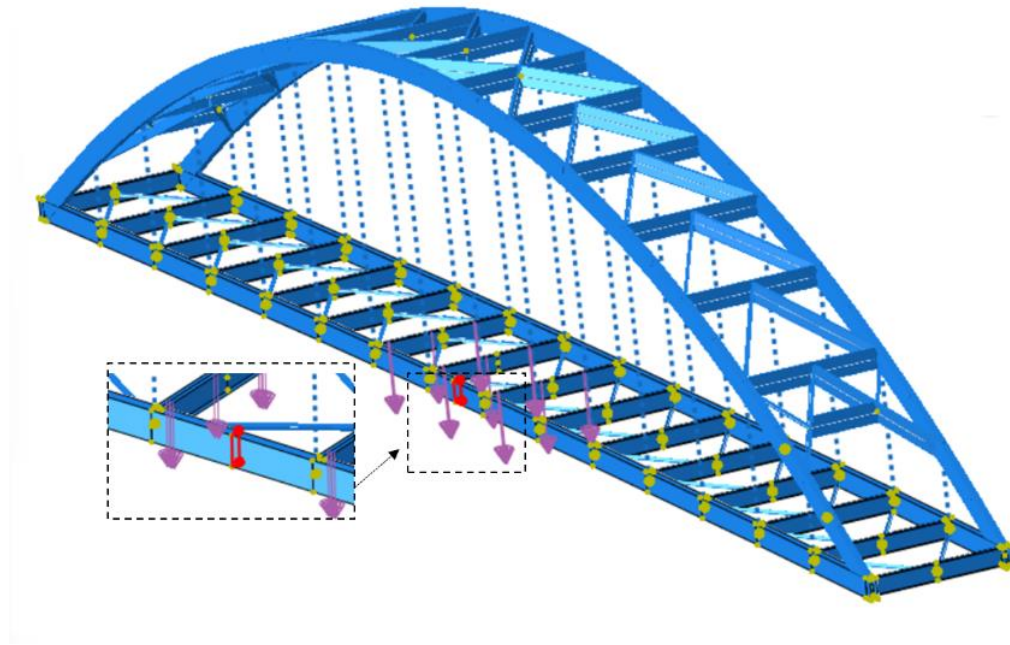


Source: FHWA

**Figure 30. Graph. Vertical deflection in TB of AWR bridge under different loading conditions.**

#### 4.4.5 Longitudinal stress in the component plates of TB

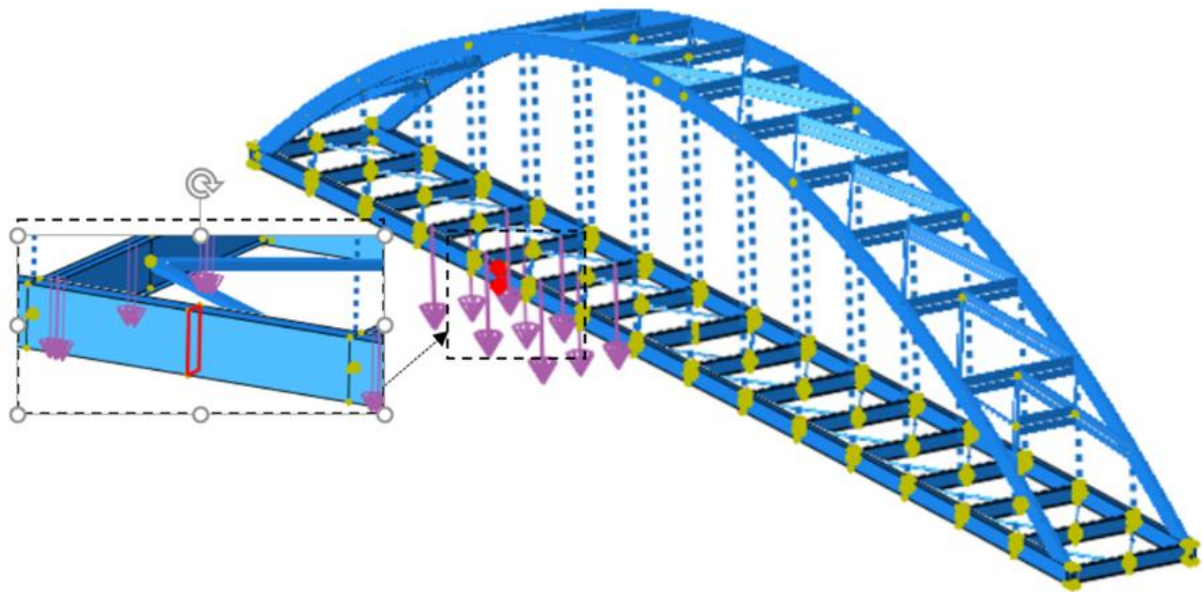
The specific locations along the TB where these stress values were extracted are indicated by the red box in Figure 31 for the midspan plots and Figure 32 for the quarter-span plots. Figure 33, Figure 34, and Figure 35 present the longitudinal stress ( $S_{11}$ ) distribution under dead load for the bottom plate, top plate, and outer plate, respectively. The corresponding stress distributions under dead and lane load are shown in Figure 36, Figure 37, and Figure 38. For the case with dead, lane, and truck loads applied at the midspan, the stresses are also presented in Figure 39, Figure 40, and Figure 41, while for the case with trucks positioned at the quarter span, the stress distributions are shown in Figure 42, Figure 43, and Figure 44.



Source: FHWA

**Figure 31. Graph. TB location for stress evaluation when trucks are placed at mid-span.**



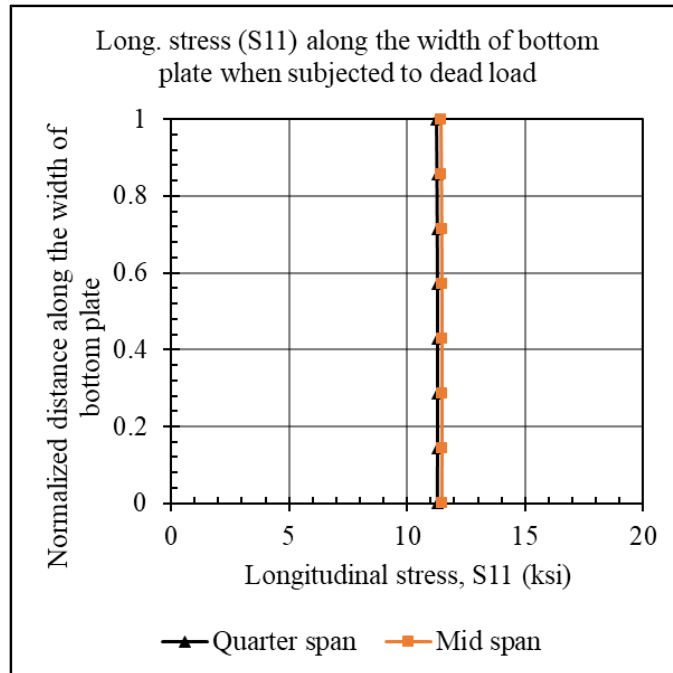


Source: FHWA

**Figure 32. Graph. TB location for stress evaluation when trucks are placed at quarter-span.**

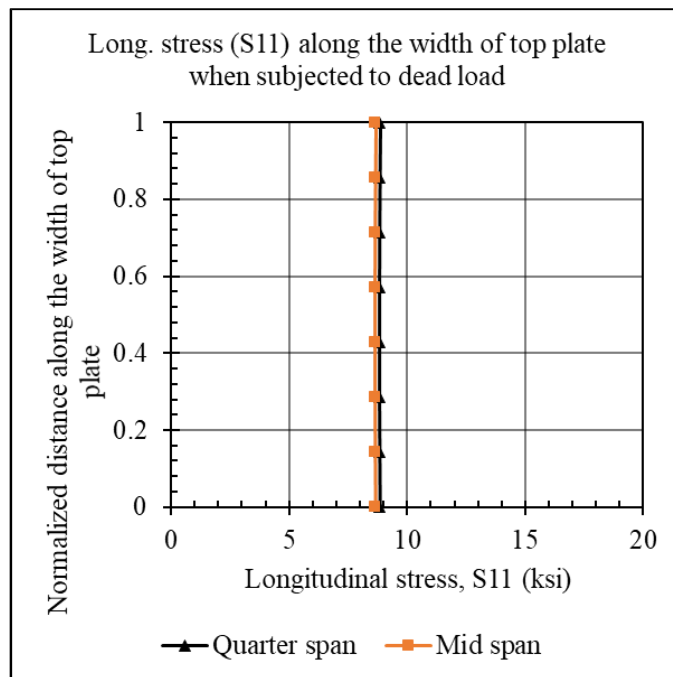
As demonstrated in the Birmingham Bridge analysis, the component plates of the TB show consistent behavior under various loading conditions. The top and bottom plates primarily experience uniform axial tension across their width due to the absence of significant lateral bending. Among these, the bottom plate is more critical, consistently exhibiting higher tensile stress than the top plate due to the presence of flexural effects. This difference becomes more pronounced under truck loading, where the concentrated loads induce increased tension in the bottom plate near the loaded regions. For the AWR bridge, a similar trend was observed. Under dead and lane loads, the stress distribution remained uniform with consistent values at both midspan and quarter-span locations. However, the application of truck loads resulted in a significant increase in localized stress, particularly in the bottom and outer plates. These findings confirm the sensitivity of TB components to high concentration loads and the importance of their position on the bridge span.





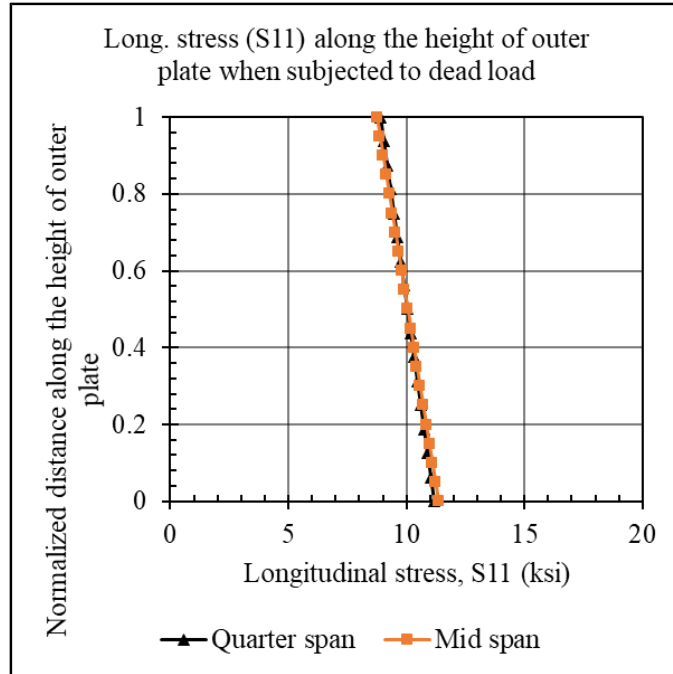
Source: FHWA

**Figure 33. Graph. Longitudinal stress (S11) along the width of bottom plate when subjected to dead load.**



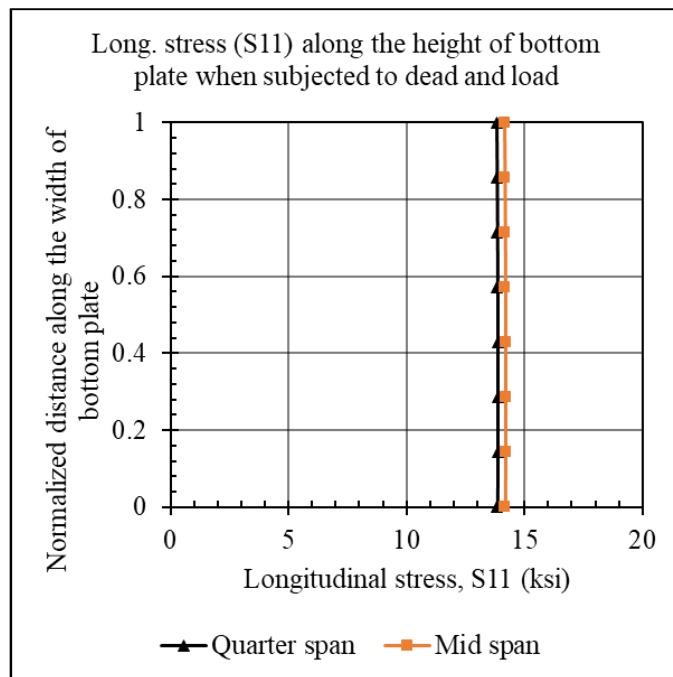
Source: FHWA

**Figure 34. Graph. Longitudinal stress (S11) along the width of top plate when subjected to dead load.**



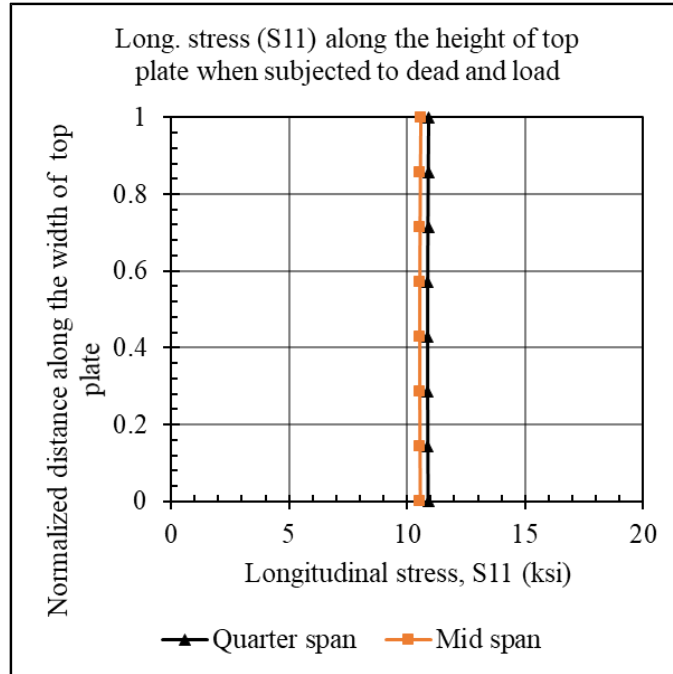
Source: FHWA

**Figure 35. Graph. Longitudinal stress (S11) along the height of outer plate when subjected to dead load.**



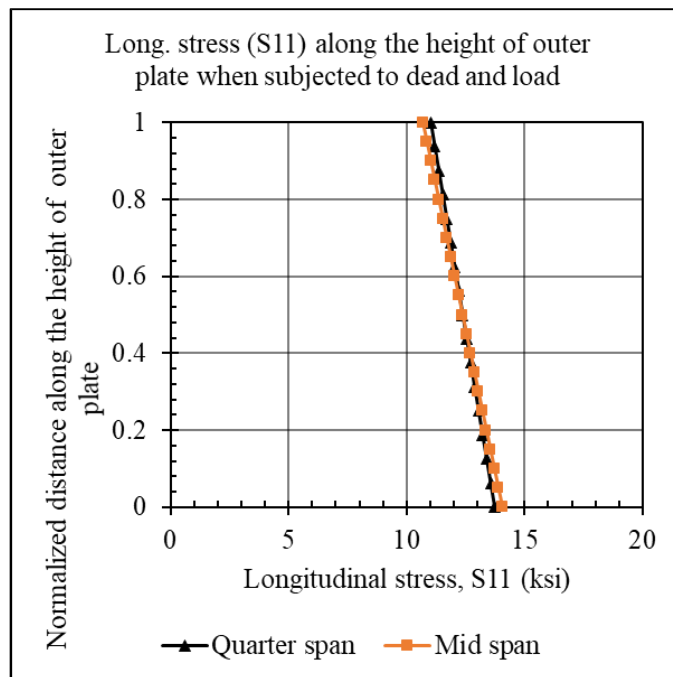
Source: FHWA

**Figure 36. Graph. Longitudinal stress (S11) along the width of bottom plate when subjected to dead and lane load.**



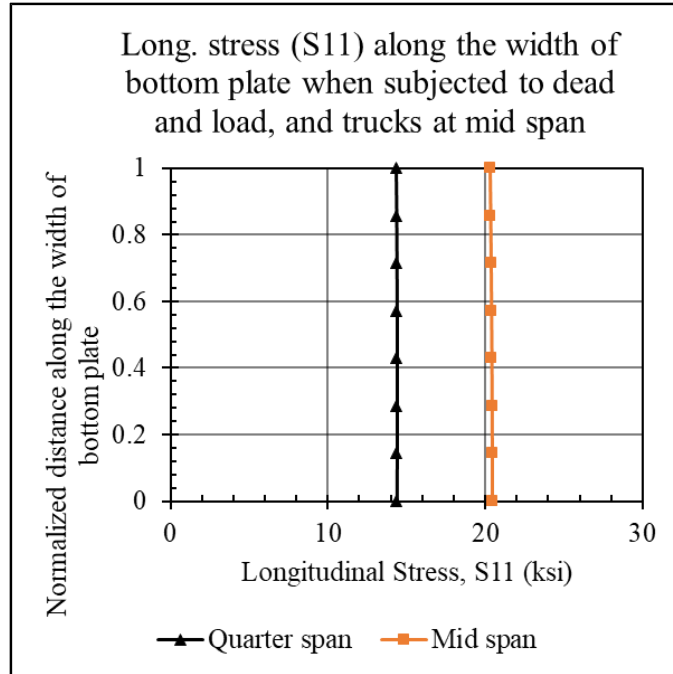
Source: FHWA

**Figure 37. Graph. Longitudinal stress (S11) along the width of top plate when subjected to dead and lane load.**



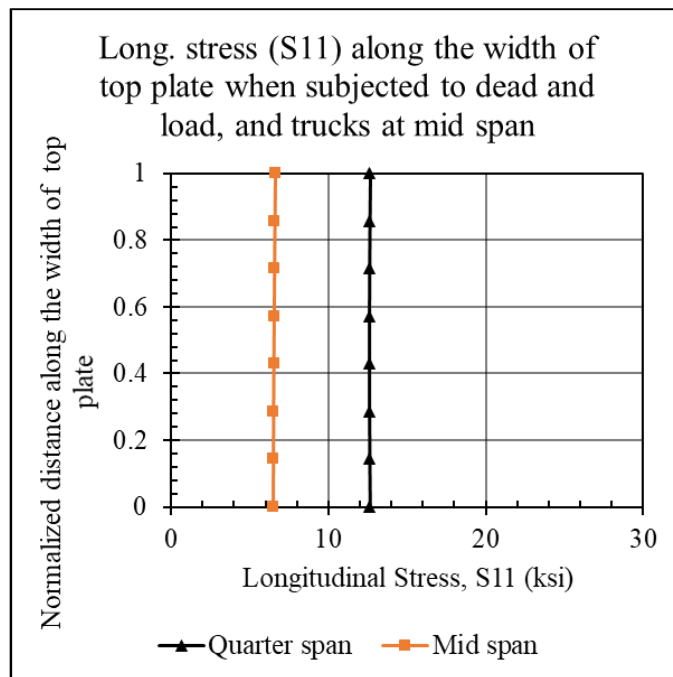
Source: FHWA

**Figure 38. Graph. Longitudinal stress (S11) along the height of the outer plate when subjected to dead and lane load.**



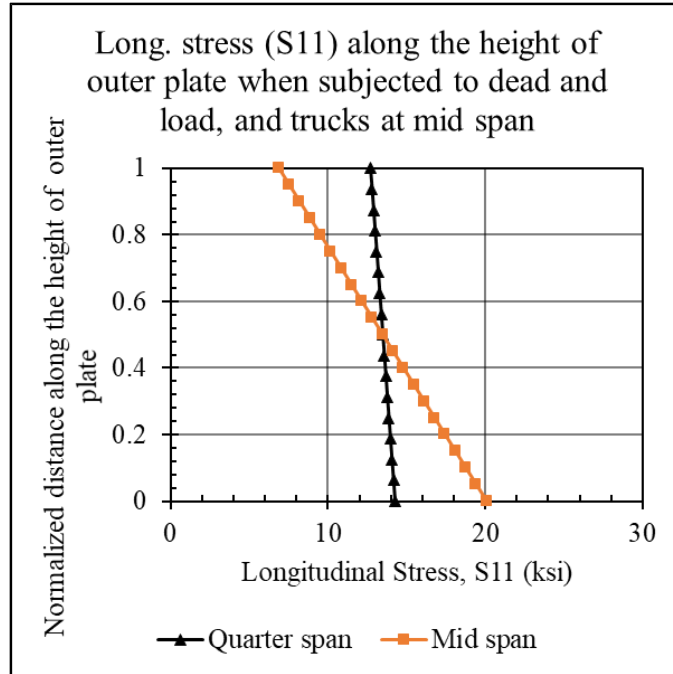
Source: FHWA

**Figure 39. Graph. Longitudinal stress (S11) along the width of bottom plate when subjected to dead and lane load, and trucks at midspan.**



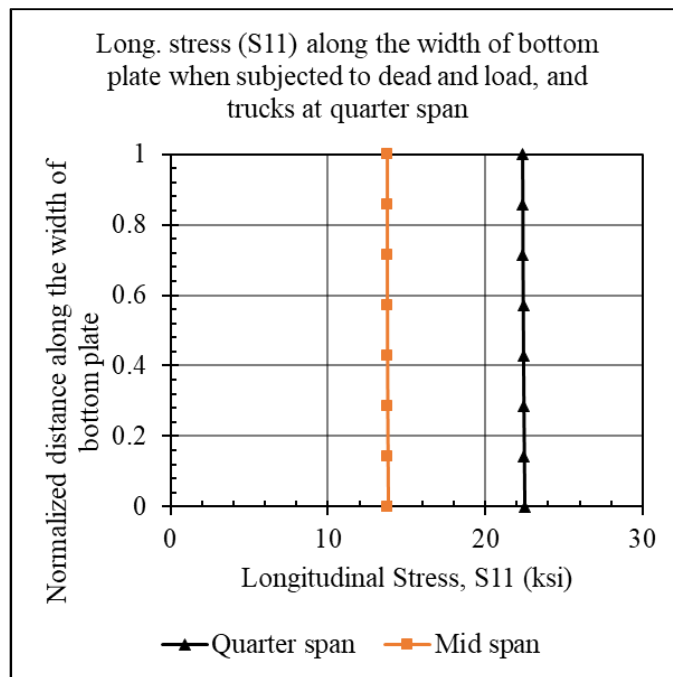
Source: FHWA

**Figure 40. Graph. Longitudinal stress (S11) along the width of top plate when subjected to dead and lane load, and trucks at midspan.**



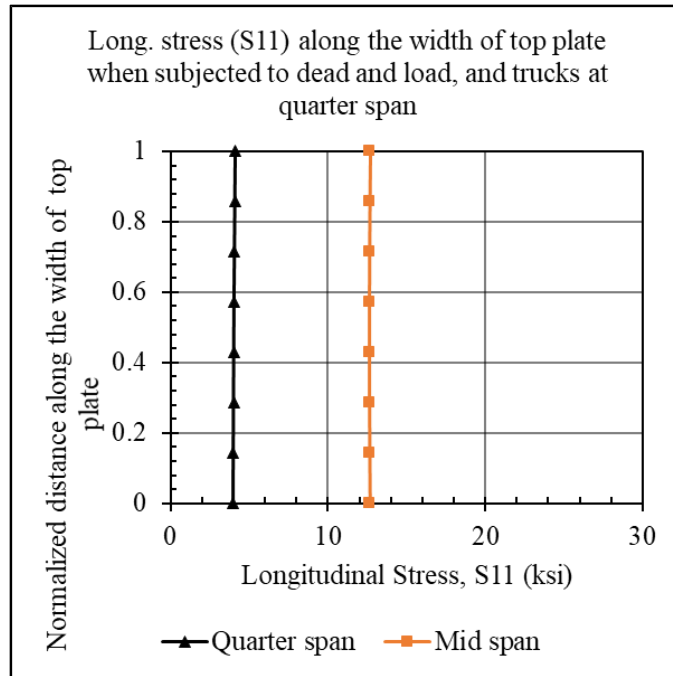
Source: FHWA

**Figure 41. Graph. Longitudinal stress (S11) along the height of outer plate when subjected to dead and lane load, and trucks at midspan.**



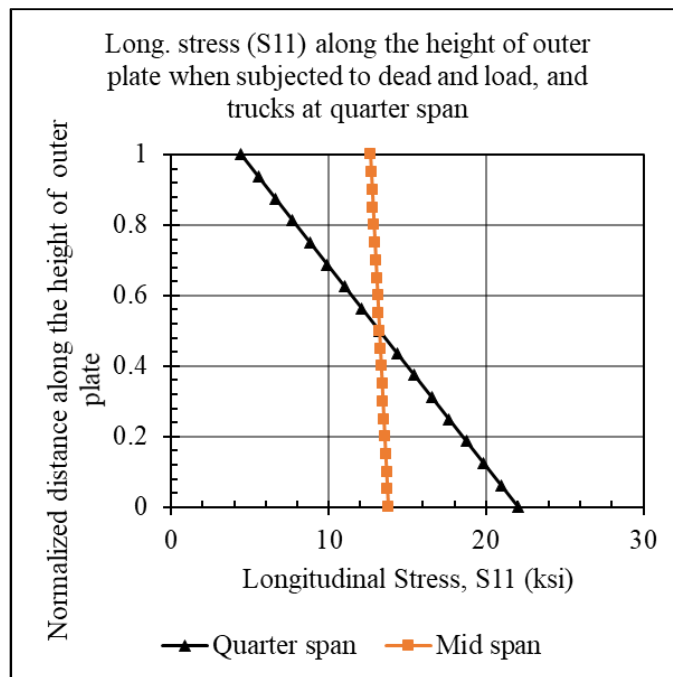
Source: FHWA

**Figure 42. Longitudinal stress (S11) along the width of bottom plate when subjected to dead and lane load, and trucks at quarter span**



Source: FHWA

**Figure 43. Graph. Longitudinal stress (S11) along the width of top plate when subjected to dead and lane load, and trucks at quarter span**



Source: FHWA

**Figure 44. Graph. Longitudinal stress (S11) along the height of outer plate when subjected to dead and lane load, and trucks at quarter span**

As presented in Figure 33 and Figure 36, the longitudinal stress in the bottom plate at both the midspan and quarter-span locations increases from approximately 11 ksi under dead load to

around 14 ksi with the addition of lane load. This increase is nearly identical at both locations. However, when truck loads are introduced, the stress rises significantly. At mid span, the stress increases to approximately 20 ksi (Figure 39), while for the quarter-span truck loading case, it reaches around 21 ksi (Figure 42).

In the case of the top plate, as shown in Figure 34 and Figure 37, the longitudinal stress increases from approximately 9 ksi under dead load to about 11 ksi with the addition of lane load, showing similar behavior at both the midspan and quarter-span locations. However, when truck loads are applied, the top plate experiences compressive stress due to flexural effects and therefore does not show a significant increase in tensile stress.

The stress response of the outer plate, shown in Figure 35 for dead load and in subsequent figures for live load cases, reflects the combined presence of axial and bending stresses along the normalized height of the TB. Under dead load, the bending stress was approximately 1 ksi and increased to about 1.5 ksi with the addition of lane load. When trucks were placed at midspan, the bending stress increased to roughly 6.5 ksi. However, when trucks were placed at the quarter span, the stress in the outer plate rose sharply to approximately 9 ksi. This increase was expected, as a higher bending moment demand was also observed in Figure 28 for the quarter-span truck loading scenario.

#### **4.5 GLOBAL RESPONSE OF AWR BRIDGE IN THE FAULTED CONDITION**

As noted in the previous section, under the combined effects of dead, lane, and truck loads, the bottom and side plates (outer and inner) of the TB become the most critical components. Therefore, any fracture studies aimed at evaluating the global structural response should focus on the potential impact of fractures in these plates. Following a similar approach to that used for the Birmingham Bridge, fracture simulations were conducted to assess how damage to a single component in the shallow TB of the AWR bridge influences the overall structural behavior.

To evaluate this, two fracture locations were selected: one adjacent to an FB connection and another between FB connections. Fracture near the FB is of particular interest due to the localized forces introduced by the FB and hanger connections. In contrast, regions between FBs often experience higher bending demands, especially near midspan, making them critical zones for assessing flexural sensitivity.

To understand the effects of such fractures, multiple cases were modeled to examine how damage to a single plate alters the axial forces and bending moments in the remaining components. Two types of fractures were considered at each location: one simulating a complete fracture of the bottom flange, and another simulating a complete fracture of a single web plate. These fracture scenarios were evaluated under two separate truck loading conditions: one with trucks positioned at the quarter span and the other at midspan.

This resulted in four fracture scenarios for each loading case, covering both outer plate and bottom plate fractures located near and between FB connections. For truck loading at the quarter span, fractures were simulated near the FB at the L4 connection and between FBs from L4 to L5. For midspan truck loading, fractures were simulated near the FB at the L7 connection and between FBs from L7 to L8.

To simulate the fracture, elements representing the failed component were selectively removed, creating a crack-like discontinuity in the model. In each fracture case, dead and lane loads were applied in addition to the truck loads to realistically represent service conditions. This modeling approach enabled a detailed evaluation of how localized fractures in key TB plates influence global force redistribution and the overall structural performance of the AWR Bridge.

#### **4.5.1 Effect of simulated fractures**

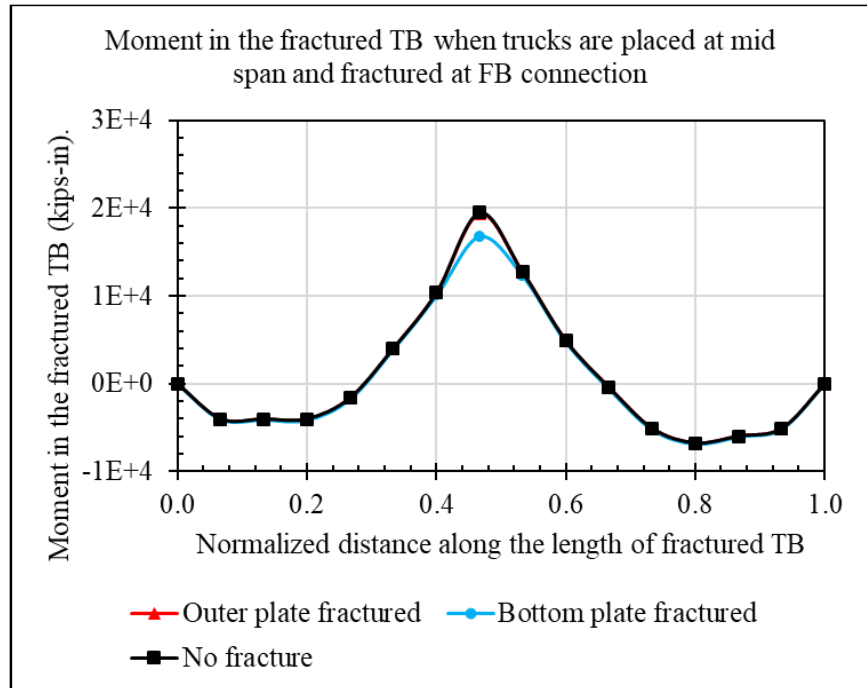
Following the simulated fracture scenarios described earlier, the structural response of the AWR bridge was evaluated and compared to the unfaulted condition. The objective was to determine whether a localized fracture in a component plate of the TB significantly alters the global force distribution across the bridge. As with the Birmingham bridge, the failure of a single TB component did not lead to any meaningful change in the overall structural behavior.

For the midspan truck load scenario with fractures modeled between FBs, the bending moment profile along the fractured TB is shown in Figure 45 and Figure 46. In this case, fractures were analyzed at two locations: near the FB connection (Figure 45) and between FBs (Figure 46). In both locations, the bottom plate fracture resulted in a more noticeable reduction in bending moment compared to the outer plate fracture. This outcome is expected because the bottom plate plays a critical role in resisting flexural demands in the TB. The analysis of the AWR shows the critical nature of bottom plate fracture in comparison to an outer plate fracture scenario. Vertical loads on the bridge are efficiently transmitted to the TB through tension generated by the arch. In this bridge, where the cross-sectional area of each plate is proportionally equal, the bottom plate carries a tensile force of approximately 616 kips with a longitudinal stress of 21 ksi. This is more than the tension carried by the outer plate, which amounts to 404 kips and tensile stresses of around 13.5 ksi. Consequently, the severing of the bottom plate is a critical concern due to its role in carrying the higher tensile force and inducing a significant change in the bending moment within the TB.

The reduction in bending moment caused by the bottom plate fracture was approximately 2,742 kip-inches when the fracture occurred near the FB connection and about 1,513 kip-inches when it occurred between FBs. In comparison, the outer plate fracture had a much smaller effect, with a maximum difference of only 79 kip-inches, or 0.6 percent, and a peak deviation of 12 kip-inches in other regions of the TB. Given that the maximum bending moment in the unfaulted condition was approximately 19,525 kip-inches, these variations reflect only localized changes. Overall, the global structural response remains largely unaffected by the fracture of a single component plate.

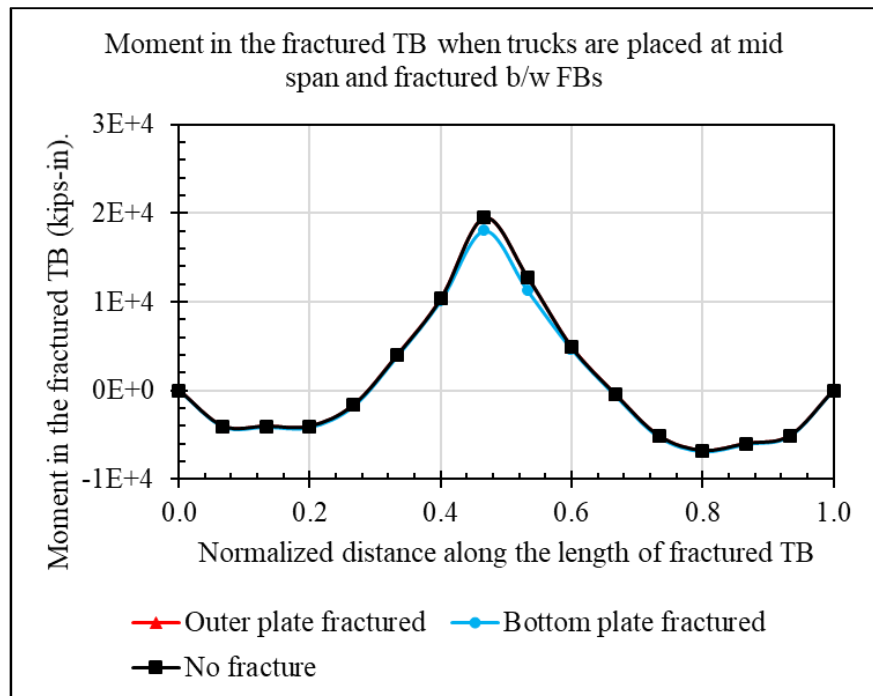
Although the results discussed here are based on the midspan truck load scenario, the analyses performed for the quarter span truck load scenario produced nearly identical trends and conclusions.





Source: FHWA

**Figure 45. Graph. Moment in the fractured TB when trucks are placed at mid span and fractured at FB connection.**



Source: FHWA

**Figure 46. Graph. Moment in the fractured TB when trucks are placed at mid span and fractured between FBs.**

Table 9 and Table 10 present the percentage difference in axial tension in the fractured TB for the between-FB and near-FB connection scenarios, respectively, when trucks are placed at the midspan. The results indicate that the variation in axial force due to simulated fractures remained below 0.5 percent along the entire length of the TB. This minimal change highlights the limited influence that a single component fracture has on the axial behavior of the TB at the system level. The negligible variation in axial tension is attributed to the structural continuity and redundancy of the remaining unfractured components, which continue to effectively carry the axial load. Whether the fracture occurred near the FB connection or between FBs, and regardless of whether it involved the bottom plate or the outer plate, the global axial response remained largely unchanged.

These findings are consistent with those from the Birmingham Bridge analysis. In both cases, the fracture of a single plate does not significantly alter the axial force distribution within the TB, demonstrating that the structural system has sufficient internal redundancy to accommodate such localized damage without compromising overall behavior.

**Table 9. Difference (%) in the axial force of fractured TB when trucks are placed at mid-span**

<b>Section Point</b>	<b>Percentage difference, bottom plate fractured</b>	<b>Percentage difference, outer plate fractured</b>
L1	-0.26	-0.28
L2	-0.24	-0.26
L3	-0.23	-0.24
L4	-0.21	-0.23
L5	-0.19	-0.21
L6	-0.18	-0.22
L7	-0.15	-0.06
L8	-0.12	-0.16
L9	-0.10	-0.12
L10	-0.08	-0.10
L11	-0.06	-0.08
L12	-0.04	-0.06
L13	-0.02	-0.04
L14	0.01	-0.02

**Table 10. Difference (%) in the axial force of fractured TB when trucks are placed at quarter-span**

<b>Section Point</b>	<b>Percentage difference, bottom plate fractured</b>	<b>Percentage difference, outer plate fractured</b>
L1	-0.29	-0.23
L2	-0.27	-0.21
L3	-0.25	-0.20
L4	-0.23	-0.19
L5	-0.21	-0.18
L6	-0.20	-0.20
L7	-0.17	-0.18
L8	-0.14	-0.11
L9	-0.12	-0.10
L10	-0.10	-0.08
L11	-0.08	-0.07
L12	-0.06	-0.05
L13	-0.03	-0.03
L14	-0.01	-0.01

The influence of component fractures on hanger forces in the AWR Bridge was evaluated for the midspan truck load scenario, with the results presented in Table 11 and Table 12. Overall, the variation in hanger forces was small and primarily affected only the hangers located near the fractured location. The largest variation occurred in the case of a fracture at the FB connection, which is expected to be due to the direct force transfer between the floor beams and the hangers at these locations. A fracture in this region disrupts the load path, resulting in slightly greater changes in hanger tension compared to fractures occurring between FBs.

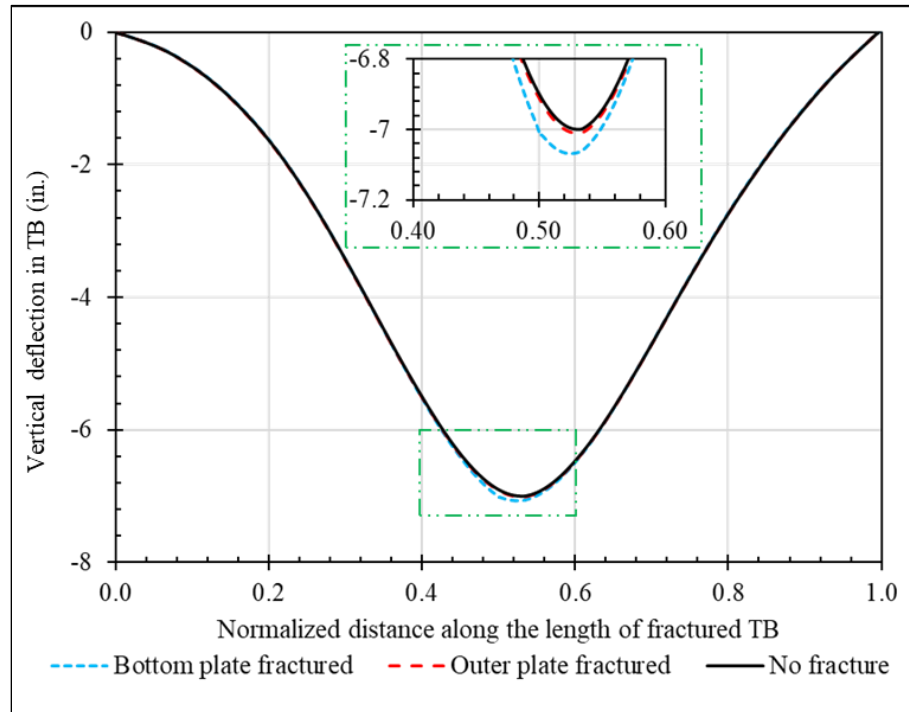
**Table 11. Difference (%) in the hanger forces of fractured TB when trucks are placed at mid span and fractured between FBs**

<b>Hanger ID</b>	<b>Percentage difference, bottom plate fractured</b>	<b>Percentage difference, outer plate fractured</b>
L1U1	0.11	0.09
L2U2	-0.03	-0.05
L3U3	0.00	-0.02
L4U4	0.02	-0.04
L5U5	-0.18	-0.06
L6U6	-1.85	0.01
L7U7	1.90	0.05
L8U8	2.00	0.05
L9U9	-1.87	0.00
L10U10	-0.20	-0.07
L11U11	0.01	-0.05
L12U12	-0.01	-0.04
L13U13	-0.05	-0.09
L14U14	0.07	0.03

**Table 12. Difference (%) in the hanger forces of fractured TB when trucks are placed at mid span and fractured at FB**

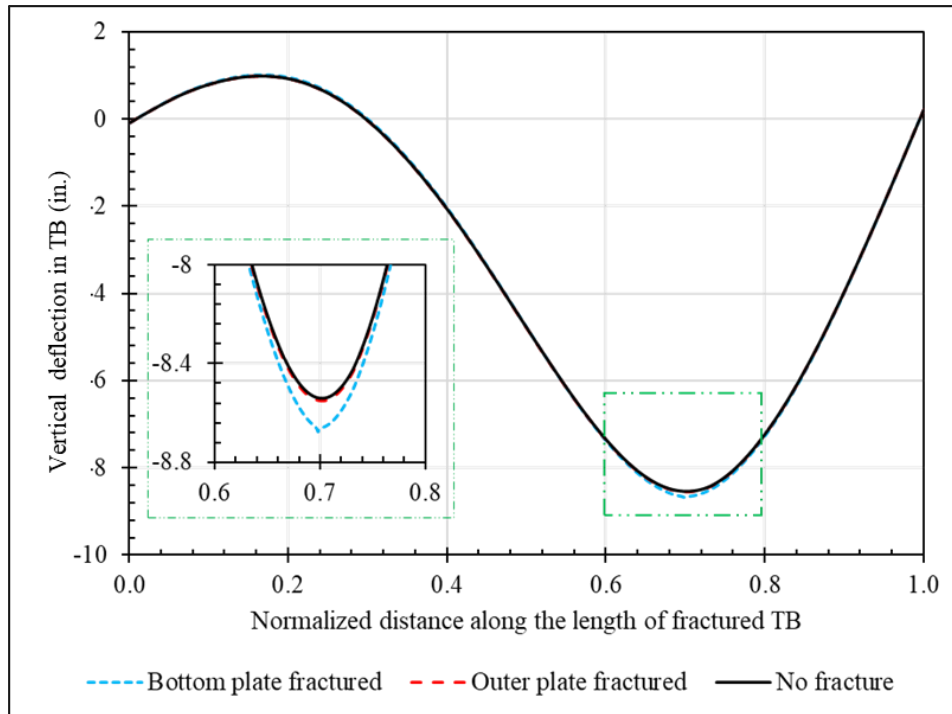
<b>Section Point</b>	<b>Percentage difference, bottom plate fractured</b>	<b>Percentage difference, outer plate fractured</b>
L1U1	0.04	0.02
L2U2	0.03	0.01
L3U3	0.03	0.00
L4U4	0.11	0.00
L5U5	-0.36	-0.01
L6U6	-3.27	-0.04
L7U7	6.75	0.00
L8U8	-3.05	0.03
L9U9	-0.40	-0.03
L10U10	0.11	-0.01
L11U11	0.00	-0.01
L12U12	0.00	-0.01
L13U13	0.01	-0.03
L14U14	0.00	-0.03

In addition to evaluating bending moments, axial forces, and hanger tensions, the vertical deflections of the TB were also analyzed to assess the impact of localized fractures on the global stiffness of the AWR Bridge. The vertical deflection profiles for the midspan truck load scenario, with fractures located between FBs and at FB connections, are shown in Figure 47 and Figure 48, respectively. In both cases, the TB exhibited only slight changes in deflection in the fractured condition compared to the unfractured state. These differences in deflection were small in magnitude and remained localized near the fracture. The overall deflected shape and global displacement pattern of the TB remained largely consistent with those of the intact configuration, indicating that the system-level stiffness is not significantly affected by a single plate fracture.



Source: FHWA

**Figure 47. Graph. Vertical deflection in the fractured TB when trucks are placed at midspan and fractured between FBs**



Source: FHWA

**Figure 48. Graph. Vertical deflection in the fractured TB when trucks are placed at quarter span and fractured between FBs**

This chapter presented a comprehensive FE investigation of two tied arch bridges: the Birmingham Bridge with a deep TB and the AWR Bridge with a shallow TB. The objective was to evaluate the influence of localized component fractures on global structural behavior and to examine whether TB depth affects global response and force redistribution. For both bridges, the response was evaluated under combined dead, lane, and truck loads, followed by a series of fracture simulations in critical TB components, specifically the bottom and outer plates. The analysis considered fracture locations both near and between FB connections, and the resulting structural behavior was compared to the unfaulted condition.

The results consistently showed that localized fractures, whether in the deep TB of the Birmingham Bridge or the shallow TB of the AWR Bridge, produced only minor changes. These changes remained localized and did not significantly affect the overall global behavior. Axial tension in the TB remained largely unchanged in both bridges, with variations typically below 0.5 percent. Hanger forces also varied only slightly, with noticeable differences limited to hangers adjacent to the fracture. The maximum observed difference in hanger force was 12 kips, recorded in the AWR bridge under a bottom plate fracture near an FB connection. Changes in vertical deflection were also minimal, and the overall deflected shape and bending moment profiles remained nearly identical to those in the unfaulted condition.

The consistent trends observed in both bridges demonstrate that TB depth does not significantly influence the global response of a tied arch bridge with a localized fracture in the TB. Both deep and shallow TB systems exhibited sufficient internal redundancy, enabling them to maintain structural integrity despite localized damage. These findings support the use of sub-modelling

strategy for evaluating fracture scenarios and contribute to the development of practical redundancy assessment methods for TBs subjected to combined tensile and flexure loading.

## 5 SUBMODELLING PARAMETERS

As demonstrated in the previous chapter through the examples of the Birmingham and AWR bridges, fracturing a component plate of the TB does not significantly influence the global response of the bridge. These findings support the conclusion that a localized submodel of the TB section, incorporating the fractured component, is sufficient to capture the force redistribution occurring in the vicinity of the fracture. To thoroughly investigate the local response to component fractures in only the TB, a submodeling approach is appropriate. Submodeling is a crucial technique in FEA that efficiently facilitates a more in-depth examination of specific areas within a larger structure. This approach proves especially beneficial when certain regions experience unique loading conditions, stress concentrations, or potential failure mechanisms. By focusing computational resources on these critical areas, submodeling offers a cost-effective alternative to analyzing the entire structure at a high level of detail, which can be computationally intensive. The technique allows for a refined analysis with higher mesh density, capturing intricate details and variations in stress and strain that are essential for accurately representing local effects, such as stress concentrations, deformations, and failure modes.

Building on this insight, the current chapter presents the development of such submodels. The modeling strategy, boundary conditions, and loading procedures used to simulate the localized behavior of the fractured TB section are discussed in detail, with a focus on accurately capturing the stress redistribution and internal force flow resulting from component-level damage.

### 5.1 FORCE TRANSFER FROM GLOBAL TO SUBMODEL

To develop a localized submodel and perform parametric studies on the behavior of fractured TBs under combined axial and bending loads, a submodeling approach in Abaqus can be implemented by transferring either displacements or forces from the global bridge model. This section discusses which of these approaches is more appropriate for capturing the local behavior with sufficient accuracy. A component fracture introduces a localized reduction in stiffness due to the discontinuity in stress along the TB. This leads to a decrease in the effective moment of inertia contributing to bending resistance and a reduction in the cross-sectional area that resists axial force. To investigate the effect of this stiffness degradation, the elastic modulus was varied within the region of the TB where the fracture was located, for both the Birmingham Bridge and the AWR Bridge.

For each bridge, four models were developed. Three models had no fractures and differed only in the assigned stiffness values for the relevant TB section: full stiffness (1E), reduced stiffness by 25% (0.75E), and reduced stiffness by 50% (0.5E). A fourth model included a bottom plate fracture with the original stiffness (1E) maintained elsewhere. In the Birmingham Bridge, the variation in elastic modulus was applied to the L10 to L11 segment (Figure 8), while in the AWR Bridge, it was applied to the L7 to L8 segment (Figure 25). Assuming that the entire TB panel between two FBs becomes softer is a highly conservative approach. Previous internal redundancy studies have shown that a single fractured component in a built-up member has minimal influence on the overall stiffness of the member (2). Nonetheless, this conservative



assumption was adopted to demonstrate with confidence that a localized submodel can still capture the relevant force redistribution even under worse-case conditions.

For this analysis the models were loaded with dead and lane loads, and the design trucks were positioned at midspan to induce maximum bending demand. Axial forces in both the fractured and adjacent TB sections were extracted from the global models, and the results are summarized in Table 13 for the Birmingham Bridge and Table 14 for the AWR Bridge. As seen in the tables, variations in stiffness had no measurable effect on the axial force in the TB, regardless of whether the section was fractured or not. The axial force remained consistent across all cases, demonstrating that local stiffness reduction does not affect global axial force distribution.

**Table 13. Axial force (kips) in the impacted and adjacent section of TB of Birmingham Bridge**

Model ID	Axial force at L9L10 (kip)	Axial force at L10L11 (kip)	Axial force at L11L12 (kip)
1E – No fracture	6,729	6,729	6,726
0.75E – No fracture	6,729	6,730	6,729
0.5E – No fracture	6,730	6,730	6,726
1E – Bottom plate fracture	6,730	6,731	6,727

**Table 14. Axial force (kips) in the impacted and adjacent section of TB of AWR Bridge**

Model ID	Axial force at L6L7 (kip)	Axial force at L7L8 (kip)	Axial force at L8L9 (kip)
1E – No fracture	1,624	1,624	1,624
0.75E – No fracture	1,625	1,624	1,624
0.5E – No fracture	1,626	1,624	1,625
1E – Bottom plate fracture	1,622	1,618	1,622

The change in length (displacement) of the fractured TB segment in both bridge models is presented in Table 15 and Table 16. These results show that the axial displacement ( $\Delta L$ ) is directly influenced by the elastic modulus ( $E$ ) assigned to the fractured region. According to the elastic deformation relationship:

$$\Delta L = \frac{FL}{EA} \quad (4.1)$$

where  $F$  is the axial force,  $L$  is the original length of the segment,  $A$  is the cross-sectional area, and  $E$  is the elastic modulus. Since the cross-sectional area and length remain unchanged, and the axial force was shown earlier to be unaffected by variations in stiffness, any reduction in  $E$  results in a proportional increase in  $\Delta L$ .

This trend is clearly evident in the results. For example, in the Birmingham Bridge model, the axial displacement in the 0.5E case is approximately twice that of the 1E case, which aligns with

theoretical expectations. These findings have important implications for the submodeling approach. Since the applied axial force does not change with E, but the resulting displacement does, a load-controlled submodel that applies forces from the global model is more appropriate. A displacement-controlled approach, where boundary displacements are fixed, would not accurately represent the actual global behavior, as the imposed displacements would vary depending on the assumed stiffness and misrepresent the state of the local stress in the fractured region.

**Table 15. Change in length in the fractured TB section of Birmingham Bridge**

<b>Model ID</b>	<b>Change in length, <math>\Delta L</math> (inch)</b>
1E – No fracture	0.2340
0.75E – No fracture	0.3130
0.5E – No fracture	0.4709
1E – Bottom plate fracture	0.5118

**Table 16. Change in length in the fractured TB section of AWR Bridge**

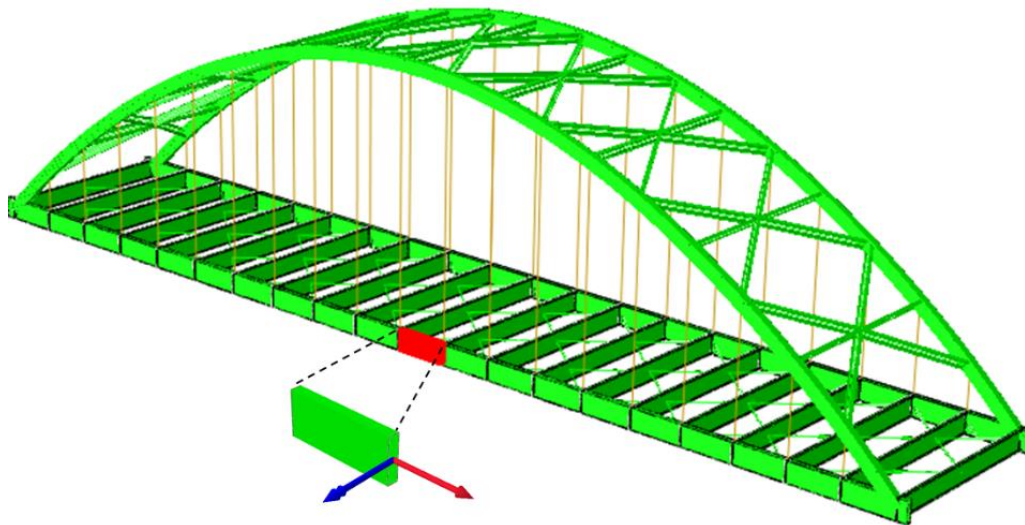
<b>Model ID</b>	<b>Change in length, <math>\Delta L</math> (inch)</b>
1E – No fracture	0.1556
0.75E – No fracture	0.2077
0.5E – No fracture	0.3117
1E – Bottom plate fracture	0.1673

## **5.2 SUBMODEL SETUP FOR THE BIRMINGHAM BRIDGE**

As mentioned earlier, the submodeling study for Birmingham Bridge focuses on a specific section of the TB located between the L10 and L11 FBs connections, highlighted with red elements in Figure 49. This segment was selected due to the high moment demand observed in the global model. To maintain consistency between the global and submodel, the TB section in the submodel was constructed using four individual plates: top, bottom, inner side, and outer side. Each plate was modeled using solid C3D8R elements, which are three-dimensional, eight-node brick elements with reduced integration. These elements were chosen for their accuracy in capturing complex stress states. Initially, the plates were tied together to replicate the welded configuration used in the global model.

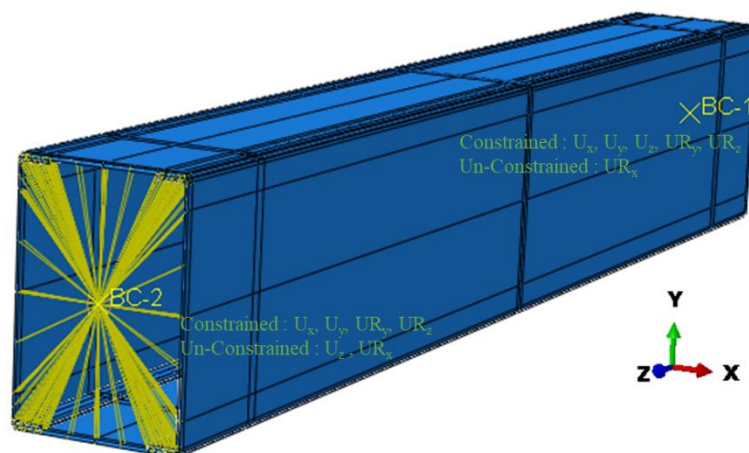
The TB submodel was developed with plate interactions and boundary loadings consistent with those in the global model to ensure meaningful and representative comparison. These boundary conditions were applied through a reference point placed at the centroid of each end section of the submodel. The reference point was coupled to the corresponding end faces of the plates, ensuring transmission of loads and displacements across the section. The full boundary condition configuration is illustrated in Figure 50.

Based on the restraints provided by the FBs and bracing elements, vertical (y) and out-of-plane (x) displacements were restrained at both ends of the submodel. Axial translational displacement (z) was restrained at one end to ensure model stability, while axial tension corresponding to the global model was applied at the other end to simulate TB continuity. Additionally, both weak axes bending ( $UR_y$ ) and torsional rotations ( $UR_z$ ) were restrained at both ends. To simulate bending demands observed in the global model, equal and opposite strong axis bending moments ( $UR_x$ ) were applied at both ends of the submodel. The values of axial force and strong axis bending moment were taken directly from the global model outputs.



Source: FHWA

**Figure 49. Illustration. Birmingham Bridge with highlighted TB section for submodeling studies.**



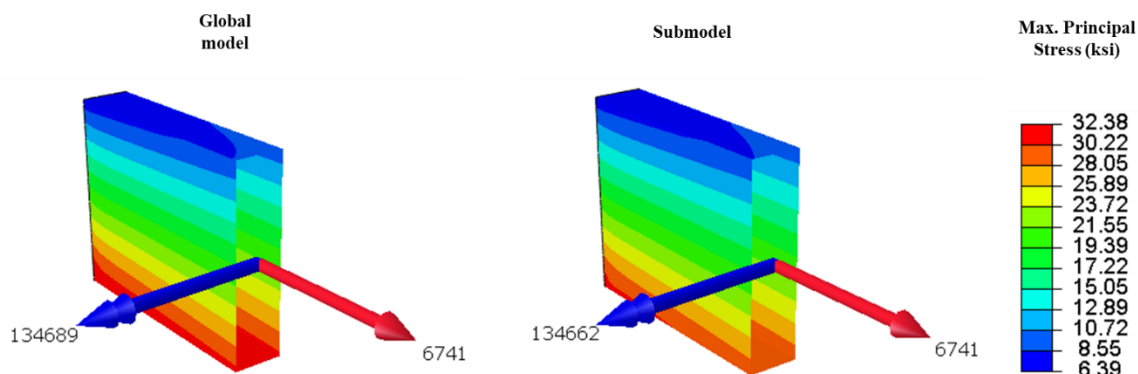
Source: FHWA

**Figure 50. Illustration. Birmingham Bridge submodel with boundary conditions.**

The section forces in the TB from both the global model and the submodel are compared in the Figure 51. The plots show the principal stress distribution, and the section is cut at the mid-length of the submodel (total length of submodel is 348 inches). The axial force, in kips (indicated by red arrows), and the bending moment, in kip-inches (indicated by the blue arrow),

are nearly identical between the submodel and the corresponding location in the global TB model. This close match confirms that the internal force transfer is consistent across both models. The same agreement is observed in the distribution of maximum principal stresses (ksi), as both models show nearly identical stress patterns in the TB section.

In summary, the close agreement in section forces and stress distributions between the global model and the submodel confirms the reliability of the submodeling approach and the applied boundary conditions and interactions. This validation supports the feasibility of advancing to the next phase of the study, which involves replacing the tied plate connections with bolted ones to investigate force redistribution and local behavior in the presence of component-level fractures.

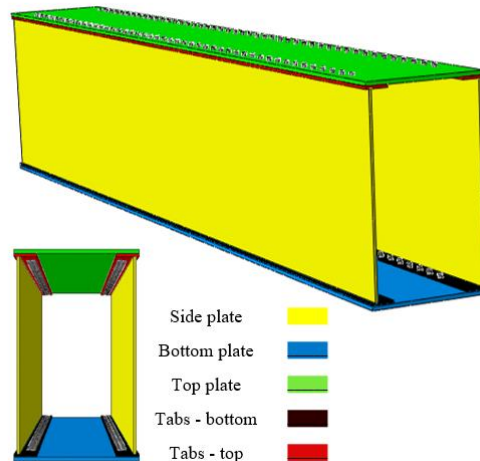


Source: FHWA

**Figure 51. Illustration. Comparison of longitudinal stress (ksi), axial force (kips) indicated by red arrow, and moment (kip-inch) indicated by blue arrow in the global and submodel.**

### 5.3 BOLTED SUBMODEL CONFIGURATION

After establishing the general submodeling approach, the next step involved introducing mechanical fasteners to connect the side plates to the top and bottom plates. To simulate a bolted built-up TB configuration, welded tab-plates (or tabs) were used in the submodel. These tabs connect the bottom and top plates to the side plates. In the FE model, the tabs were tied to the side (outer and inner) plates to represent welded connections, while the tab-plates themselves were bolted to the bottom plate. This configuration resembles in-service bridge designs such as the Broadway Bridge over the Arkansas River and the bridge on US-52 over the Mississippi River. The use of tabs in this way helps reduce the total number of bolts used to isolate each component. The geometry of the plates in the bolted submodel is based on the Birmingham Bridge and is shown in Figure 52. Fully bolted angle connections, where bolts are used in both legs of the angle instead of tabs, will be discussed in the next chapter.



Source: FHWA

**Figure 52. Illustration. Bolted submodel for Birmingham Bridge**

For these submodels, the steel was assigned to an elastic modulus of 29,000 ksi, a Poisson's ratio of 0.3, a yield strength of 50 ksi, and an ultimate tensile strength of 65 ksi. The inelastic portion of the stress-strain response was established using a Ramberg-Osgood equation, calibrated to match the chosen yield and ultimate strengths. Bolts were modeled with a yield strength of 105 ksi and an ultimate strength of 120 ksi. The meshing approach was selected to ensure accuracy in critical regions while keeping computational costs reasonable. Around each bolt hole, 17 elements were used to capture stress concentration. A finer mesh was also applied to the bolts to better represent local force transfer and potential failure mechanisms. The other regions in the plates were meshed with 0.25-inch elements near fracture region and then transitioned to 6-inch size as high stresses were not expected in the regions away from fracture. Across all plates, four elements were used through the thickness to capture stress variation and record mid-thickness stresses. The initial FE simulations used standard bolt hole sizes (i.e., 1/16-inch oversize), bolt pre-tensioning values based on bolt diameter, and a friction coefficient of 0.3. It was observed that this combination led to slippage between the plates under high loading conditions. This behavior was attributed to the oversized bolt holes, high local shear forces, and plate thinning due to Poisson's effect. While modeling slip, preload loss, and frictional behavior would provide a more complete response, such modeling is highly computationally intensive.

Since the bolts enter bearing immediately after fracture and friction is not the dominant mechanism for post-fracture force transfer, a simplified approach was adopted. In the final model, bolts were assumed to fully fill the holes, using 1-inch diameter bolts placed in 1-inch diameter holes. A frictionless general contact was established, ensuring that force transfer occurred entirely through direct bearing. This eliminates load transfer from friction and reflects a conservative scenario where bolts carry the entire load directly. This approach also accounts for realistic construction tolerances, where some bolts may be in bearing contact from the beginning. A small amount of pre-tensioning was applied to prevent bolt rotation during loading. While the assumption of full bearing and frictionless contact may be conservative in estimating bolt shear forces, it provides a realistic and practical method for capturing the critical load redistribution in the fractured TB section.

This bolted configuration, combined with the described mesh and contact assumptions, offers a robust framework for analyzing post-fracture behavior and force redistribution between TB components in a computationally efficient manner.

## 5.4 FRACTURE SCENARIOS

Similar to the global models, the submodel was subjected to fracture scenarios involving both the bottom plate and a side plate of the TB. In the case of side plate fracture, it was assumed that the tab plates connected to it were also fractured, as they are welded to the plate and would fail when the connected element fractures. The fracture was modeled using the seam feature available in Abaqus. A seam is an edge or surface where overlapping nodes are initially tied but allowed to separate during the analysis. This feature enables the simulation of fractures along a pre-selected path and allows for realistic evaluation of structural response post-fracture. All fracture simulations were conducted using the axial and, bending moments values extracted from the global bridge model under combined dead, lane, and truck loading conditions.

### 5.4.1 Force redistribution after fracture

Before any fracture, both side plates and connected tabs collectively carried an axial force of 5,381 kips, whereas the bottom plate carried only 1,223 kips, which is approximately 50 percent less than the force carried by the single side plate. The results of the force redistribution following simulated fractures are summarized in Table 17. In the case of bottom plate fracture, the axial force is redistributed to both side plates as well as to the connected tab plates. Before the fracture, both the inner and outer plates carried approximately 2,292 kips of axial force. After the bottom plate fracture, each of these plates experienced an increase of 517 kips, leading to a new axial force of approximately 2,809 and 2,811 kips, respectively. Conversely, in the scenario involving fracture of a side plate along with the associated tab plates, the redistribution of force occurred primarily to the bottom and top plates. Before fracture, the bottom and top plates carried 1,223 and 380 kips, respectively. After fracture, the bottom plate experienced an additional 1,170 kips of axial force, while the top plate experienced an increase of 1,571 kips.

**Table 17. Axial force (kips) in different plates of TB when subjected to various fracture scenarios**

<b>Component plate</b>	<b>Axial force, no fracture (kip)</b>	<b>Axial force, bottom plate fractured (kip)</b>	<b>Axial force, side plate fractured (kip)</b>
Bottom plate	1,223	0	2,393
Top plate	380	301	1,951
Side plates	4,585	5,620	1,963
Tabs – bottom	416	693	355
Tabs – top	132	104	196

### 5.4.2 Stress distribution and yielding

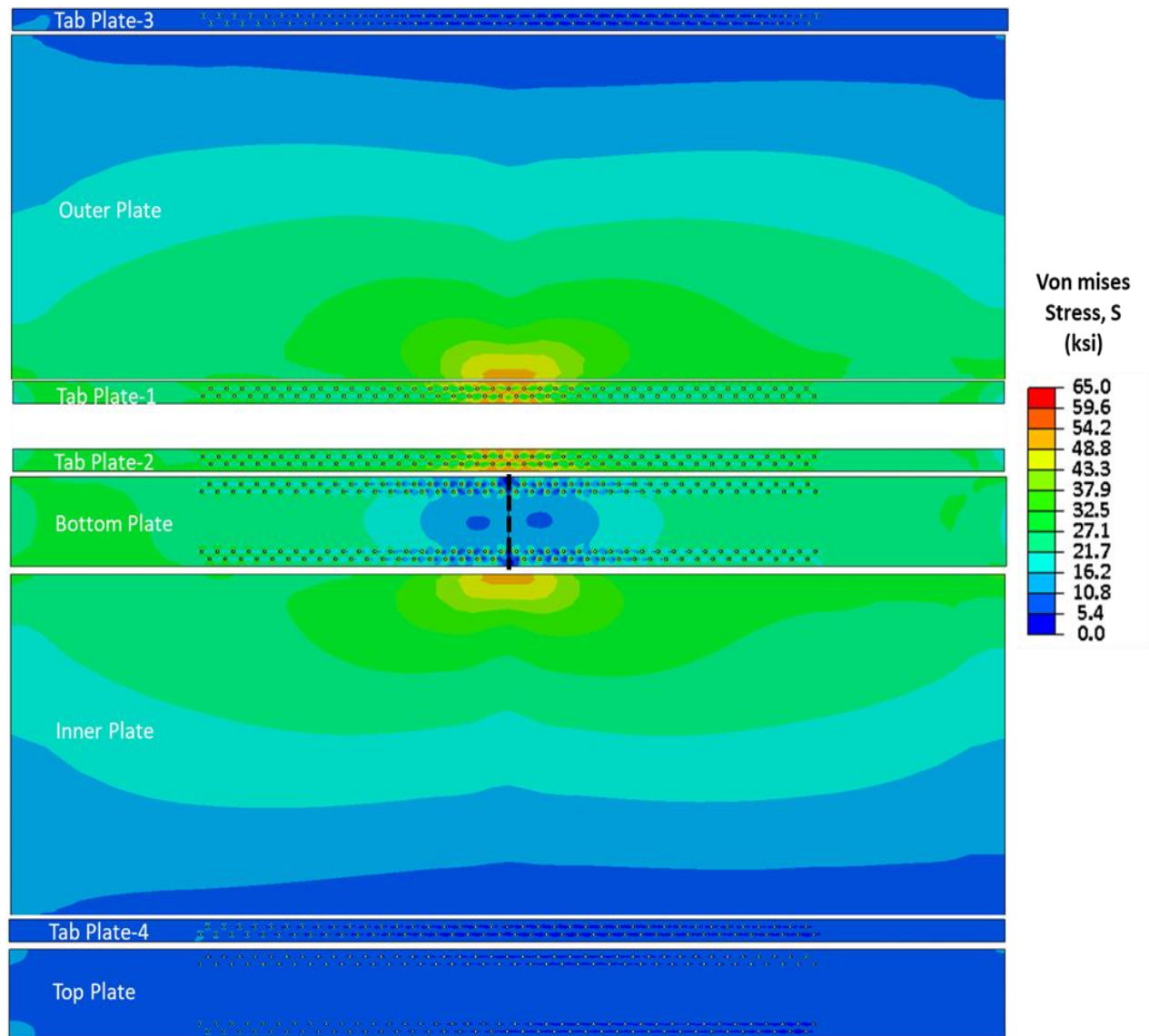
The stress distribution across the TB plates following the two fracture scenarios is shown in Figure 53 and Figure 54. These figures are generated by unfolding the TB section to provide a

continuous view of the stress distribution across all plates. The dashed black lines indicate the fracture locations.

In the case of bottom plate fracture (Figure 53), stress concentrations are observed in the tab plates as well as the outer and inner plates. Very low stress levels are seen near the fractured region of the bottom plate, consistent with the fact that there is no force transfer across the fracture. The stress concentrations remain localized near the fracture region. Under this loading condition, no yielding was observed on any of the plates.

In the scenario involving fracture of a side plate (labelled as outer plate) and the associated tab plates (Figure 54), significant stress concentrations are observed in the remaining plates. Stress is widely distributed on the top and bottom plates and remains localized in the unfractured portion of the fractured side plate. In the unfractured tab plates, elevated stresses and deformations are concentrated around several bolt holes adjacent to the fracture. This scenario leads to yielding in both the top and bottom plates, indicating that the loss of a side plate introduces more severe demand on the remaining structural elements. This outcome may suggest the need to re-evaluate the sizing of the plates to ensure structural adequacy in the presence of such a fracture.

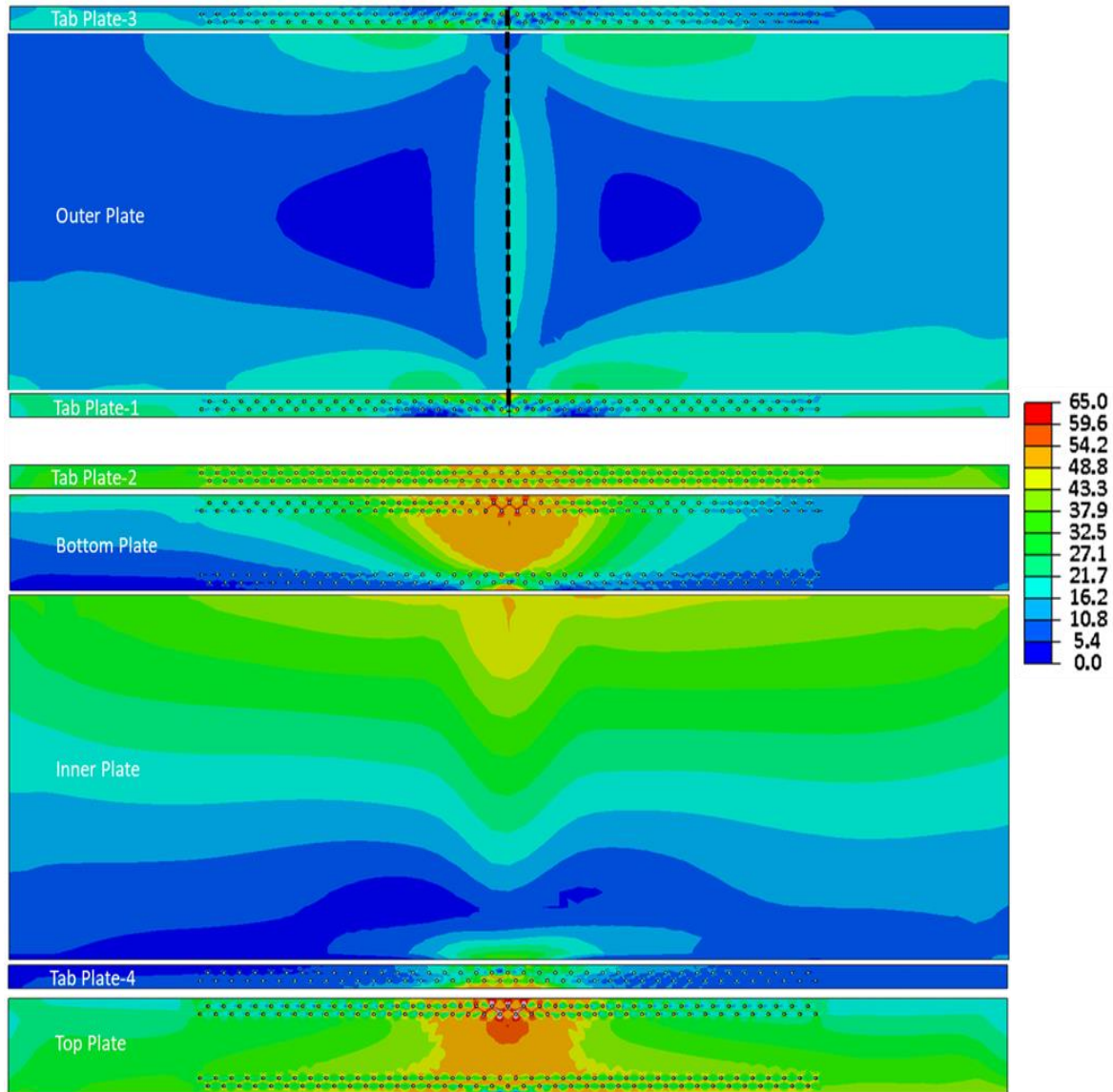
Although local yielding near the fracture, or around bolt holes is observed, it is not necessarily a cause for concern by itself. The focus should be on evaluating whether the local strains remain within acceptable limits.



Source: FHWA

**Figure 53. Illustration. Stress distribution across different plates of bolted TB when bottom plate is fractured.**





Source: FHWA

**Figure 54. Illustration. Stress distribution across different plates of bolted TB when a side plate and connected tabs are fractured.**

While the solid element-based submodel provides highly detailed insight into the stress distribution and force redistribution in the fractured TB, it is computationally expensive. Incorporating both material and geometric nonlinearity further increases the analysis time significantly. For instance, the fractured solid model presented in the previous section took approximately 8 hours to complete a single load case. Given that multiple TB geometries and loading scenarios are explored to develop a simplified and generalizable approach for assessing the internal redundancy of fractured TBs, there is no efficacy in relying solely on solid models. Therefore, it is necessary to consider alternative modeling strategies. Shell element-based models offer a promising alternative, capable of producing results comparable to solid models when accurately implemented, while substantially lowering computational demands. By using shell

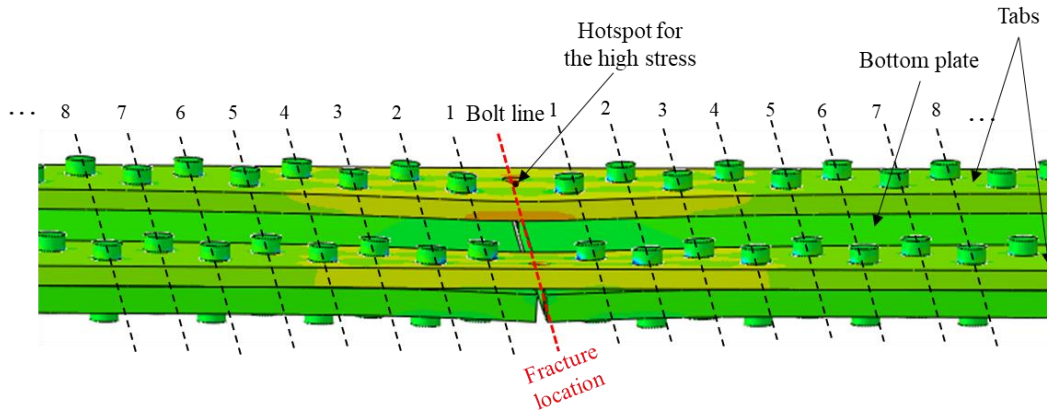
models, a broader range of configurations can be analyzed efficiently, supporting the development of a robust and simplified assessment methodology.

## **5.5 TRANSITION TO SHELL ELEMENT MODELING**

To address the computational challenges associated with solid element modeling, a shell element-based submodel was developed for the TB section. This shell submodel adopted the same boundary conditions and constraints between plates as those used in the previously validated solid submodel, ensuring consistency in how structural behavior was represented. Shell elements of type S8R were used throughout the model. These are 8-node, doubly curved, thick shell elements with reduced integration. Five integration points were established through the thickness of each shell to accurately capture through-thickness stress variations. As in previous models, all components were assigned a modulus of elasticity of 29,000 ksi, a Poisson's ratio of 0.3, and a density of 490 lb/ft<sup>3</sup>. The inelastic portion of the stress-strain curve was established using a Ramberg-Osgood fit based on the yield and ultimate strengths of 50 ksi and 65 ksi, respectively. In this shell model, bolts were modeled using connector elements in accordance with the methods established in NCHRP Web-Only Document 197 (20). This approach allowed for realistic simulation of load transfer through mechanical fasteners while reducing the computational complexity typically associated with detailed solid bolt modeling.

To evaluate the accuracy of the shell submodel, its results were compared directly to those from the solid submodel. For this comparison, the bottom plate fracture scenario was considered, and both models were subjected to an axial tensile force of 6,741 kips, consistent with the force obtained from the global model. This simplified loading condition allowed for a focused comparison of stress distribution and internal force redistribution between the two modeling approaches. By maintaining identical geometry, boundary conditions, and material properties, the comparison ensured that any observed differences in behavior could be attributed to the element type and modeling strategy rather than inconsistencies in input parameters.

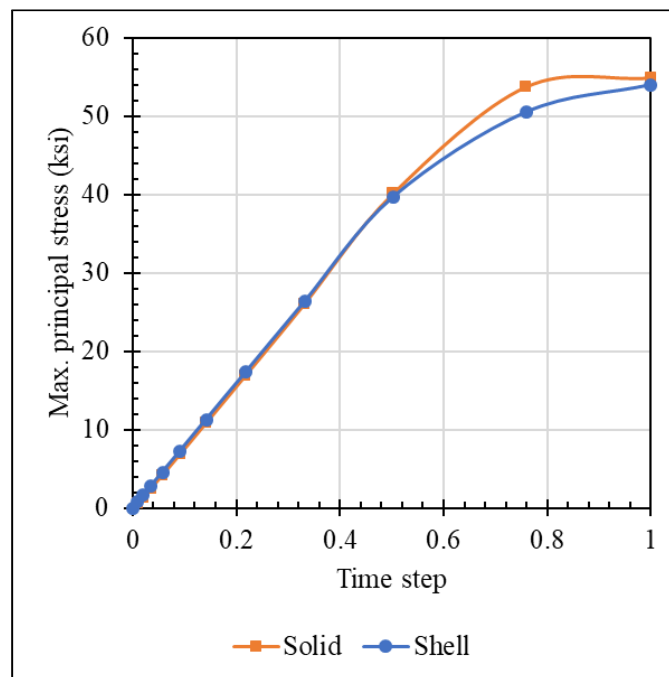
Under the bottom plate fracture condition, the bolts located directly at the fracture interface do not contribute to load transfer between the separated components. As a result, these bolts were not modeled at the fractured location in either the solid or shell submodels. Instead, the tab plates connected to the fractured bottom plate become critical in redistributing the axial load. Due to this load path, the bolt hole located in the tab plate at the fracture interface becomes a stress hotspot and a focal point for structural demand. The fractured TB and the critical tabs are shown in the Figure 55. It is important to note that the full TB, including all component plates, was used in the analysis; however, for clarity and better visualization, only the bottom plate and tab plates are highlighted in this figure.



Source: FHWA

**Figure 55. Illustration. Fractured bottom plate.**

To validate the shell submodel's ability to capture this local behavior, the stress at this bolt hole was monitored across the analysis and compared with the corresponding solid submodel results. As shown in the Figure 56, the stress histories at this location closely matched between the two models throughout the axial loading time steps, demonstrating that the shell model provides comparable accuracy in capturing local stress concentrations.

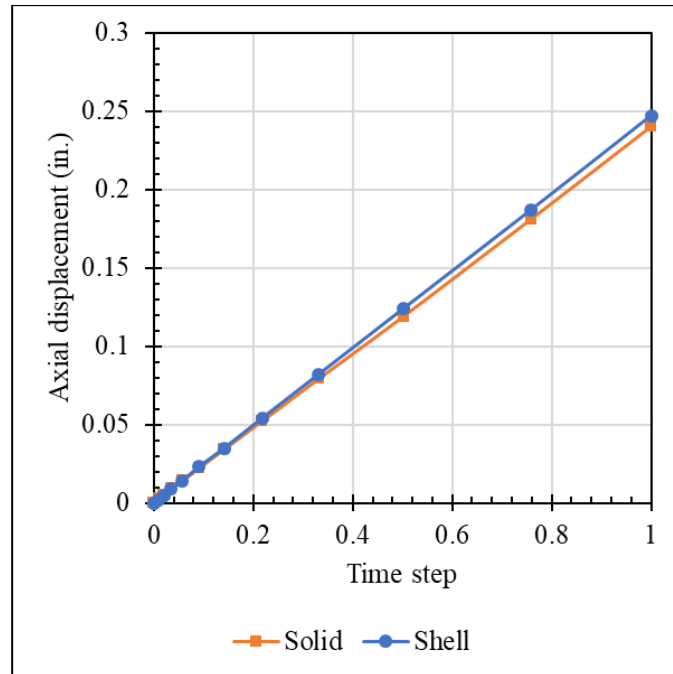


Source: FHWA

**Figure 56. Graph. Comparison of maximum principal stress at the critical bolt hole in the tab plate under bottom plate fracture and pure axial loading**

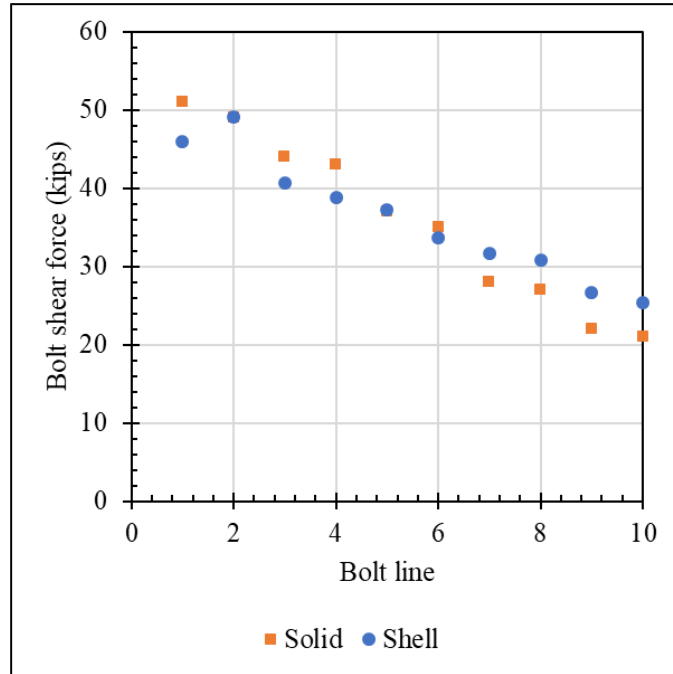
In addition to local stress, the global response of the TB was evaluated by comparing axial displacements at boundary condition location BC2 (Figure 50) for both models. This is shown in Figure 57. The displacement histories showed near-identical behavior, confirming consistency in

global deformation. Furthermore, bolt shear forces were extracted and compared across 10 consecutive bolt lines extending from the fracture location and plotted in Figure 58. It is important to note that each bolt line consists of two bolts, capturing the distribution of load across both fasteners per line. The results again showed reasonable agreement between the solid and shell models, reinforcing the validity of the shell modeling approach for capturing both local and global responses in the fractured TB configuration.



Source: FHWA

**Figure 57. Graph. Comparison of global axial displacement under bottom plate fracture and pure axial loading.**



Source: FHWA

**Figure 58. Graph. Comparison of bolt force under bottom plate fracture and pure axial loading.**

To evaluate the effectiveness of the shell submodel in capturing internal force redistribution before and after fracture, the axial forces in the individual component plates of the TB were extracted at the fracture location and compared to those obtained from the solid submodel. These values are shown in Table 18 for shell submodel and in Table 19 for solid submodel. Prior to fracture, the axial force was distributed across all component plates, with the side plates (inner and outer) carrying most of the load, while the bottom and top plates carried smaller portions. Following the fracture of the bottom plate, the load previously resisted by that plate was redistributed primarily to the connected tab plates and side plates, with a smaller share taken up by the top plate. The comparison reveals a nearly identical redistribution pattern between the solid and shell models. Both models captured the increase in axial force in the remaining plates with minimal variation, confirming that the shell submodel accurately replicates the internal force transfer mechanisms observed in the more detailed solid model. This result supports the use of shell modeling as an efficient and reliable approach for evaluating force redistribution in fractured TB configurations.

**Table 18. Axial forces (kips) in different plates of TB in shell submodel when subjected to axial load and bottom plate fractured**

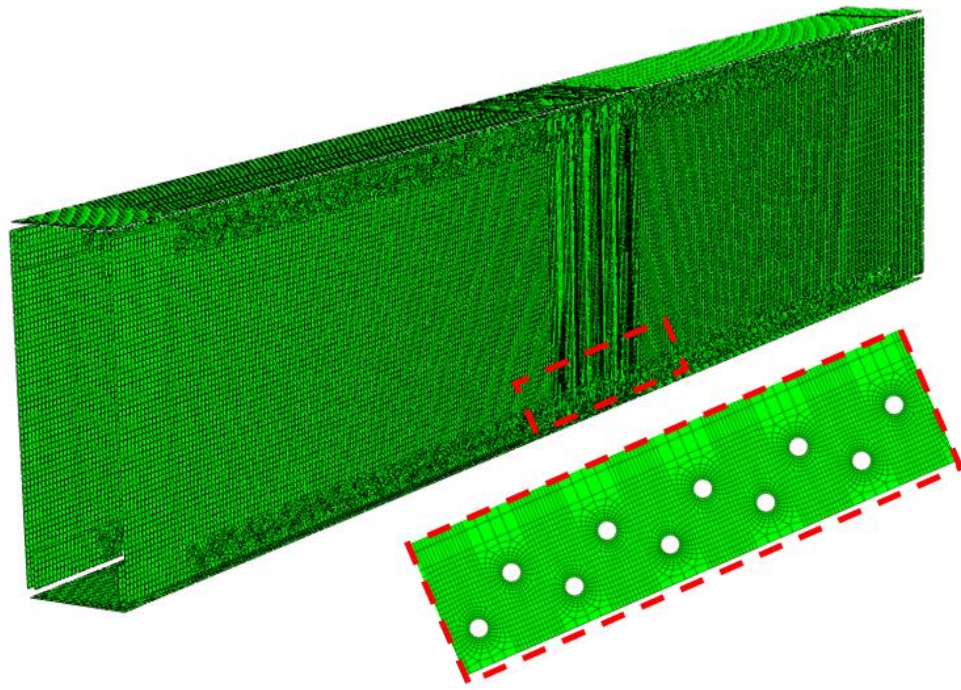
<b>Component plate</b>	<b>Axial force, no fracture (kip)</b>	<b>Axial force, bottom plate fractured (kip)</b>
Bottom plate	816	0
Top plate	816	763
Side plates	4,529	5,115
Tabs – bottom	282	605
Tabs – top	282	258

**Table 19. Axial forces (kips) in different plates of TB in solid submodel when subjected to axial load and bottom plate fractured**

<b>Component plate</b>	<b>Axial force, no fracture (kip)</b>	<b>Axial force, bottom plate fractured (kip)</b>
Bottom plate	801	0
Top plate	801	767
Side plates	4,584	5,109
Tabs – bottom	275	608
Tabs – top	275	260

With the shell submodel shown to accurately replicate both the global and local behavior of the more detailed solid submodel, it can now be confidently used for further analysis. The shell submodel significantly reduced computation time compared to its solid counterpart, lowering it from approximately 8 hours to 4.5 hours for the same loading and fracture conditions. This improvement in efficiency makes it a practical and reliable tool for conducting larger parametric studies. The final shell model with mesh details around the holes is presented in Figure 59.

The reduction in computational demand enables the investigation of a broader range of TB geometries, connection configurations, and fracture scenarios. These analyses are essential for developing a generalized and simplified methodology to assess internal redundancy in fractured TBs, which will be explored in the following chapters. The validated shell modeling framework therefore provides the foundation for the next phase of this study.



Source: FHWA

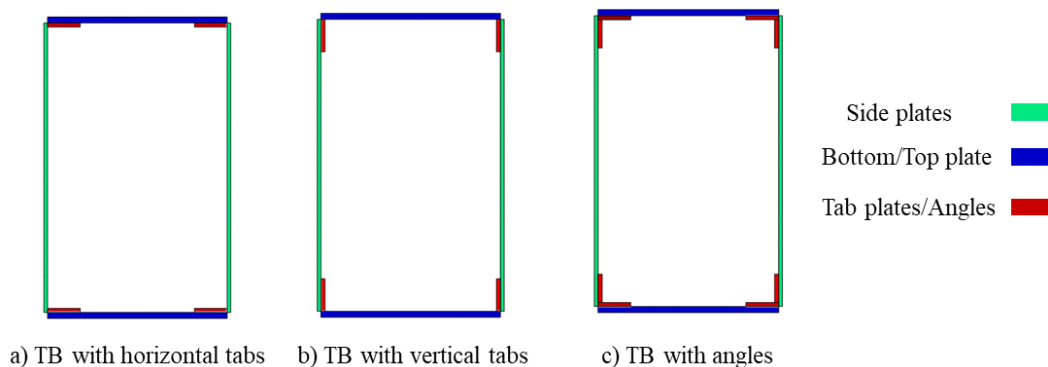
**Figure 59. Illustration. Representative FE shell model with meshing details around the bolts.**

## 6 DEVELOPMENT OF SIMPLIFIED METHODOLOGY FOR STRENGTH ANALYSIS

This chapter focuses on the development of a simplified methodology to assess the strength and internal redundancy of TB sections subjected to component-level fractures. Before introducing the failure criterion and capacity evaluation framework, it is necessary to first describe the different TB geometries and connection details considered in this study. The structural detailing at the corners of built-up TBs significantly affects their local behavior, stress redistribution, and post-fracture response. Therefore, the performance of each connection type is evaluated separately under fracture conditions to develop a generalized and reliable assessment methodology.

### 6.1 TB CORNER CONNECTIONS AND FRACTURE SCENARIOS

Multiple TB configurations were considered by varying the orientation and detailing of the connection elements located at the intersection of the top, bottom, and side plates. These configurations typically involve either tab plates or angle sections. The three connection types analyzed are illustrated in Figure 60. Although the global load path through which axial and flexural forces are transmitted remains consistent across all configurations, the specific connection details influence local stiffness, force transfer behavior, and structural performance under both service and fracture conditions.



Source: FHWA

**Figure 60. Illustration. TB geometries with different corner connections.**

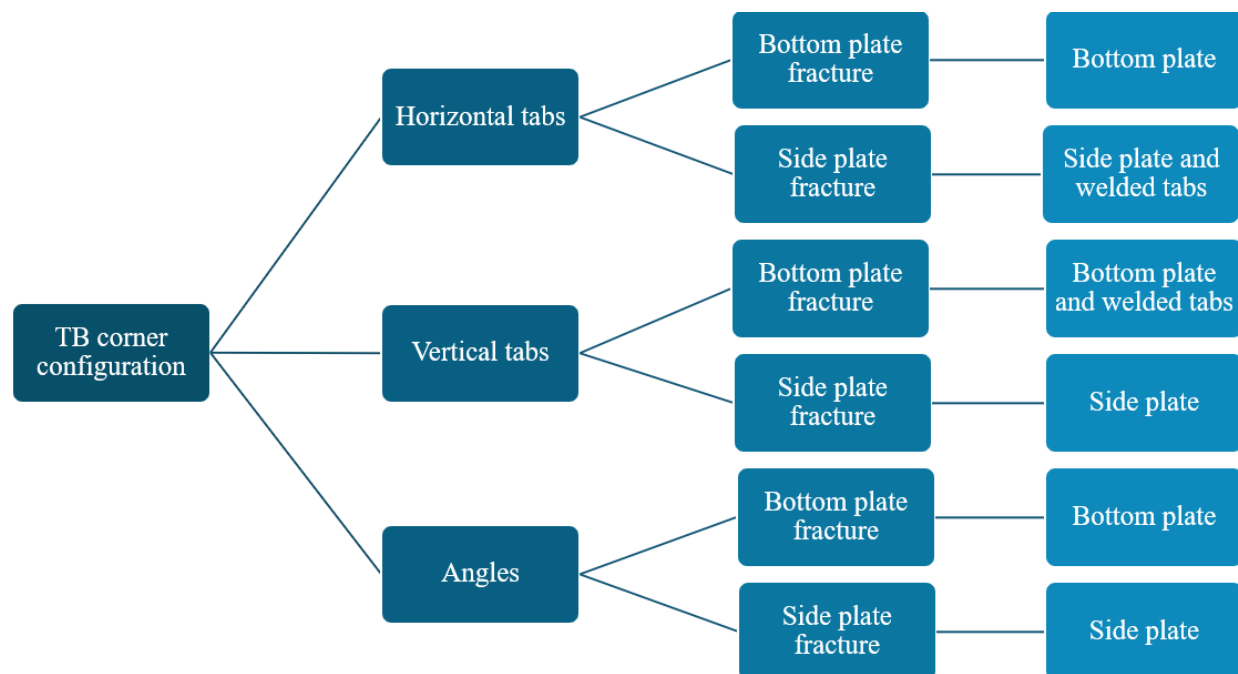
The orientation of the tab plates (indicated as red) determines which components are welded and which are bolted. In the horizontal tab configuration (Figure 60(a)), the tabs are welded to the side plates (indicated as green) and bolted to the top and bottom plates (indicated as blue). In contrast, the vertical tab configuration (Figure 60(b)) features tabs welded to the top and bottom plates and bolted to the side plates. While these connection types do not change the overall axial force path, they significantly affect how loads are introduced into each plate and how stress is distributed near the connections. The angle configuration (Figure 60(c)) differs from the tab plate systems by using angles that are bolted to the top, bottom, and side plates. There is no welded interface in this setup. This configuration establishes a direct mechanical connection between all adjacent plates and maintains continuity even when one component fractures.



The corner connection configurations directly affect how the TB responds to component-level fracture. Consistent with the fracture scenarios investigated in previous chapters, two primary cases were studied: fracture of the bottom plate and fracture of a side plate. A consistent modeling assumption was adopted for the behavior of tab plates. If the fractured plate had tabs welded to it, those tabs were also considered fractured. If the tabs were bolted to the fractured plate, they were assumed to remain intact. This assumption is supported by the concept of cross-boundary fracture resistance (CBFR), wherein bolted components continue to sustain loads across a fractured interface. This behavior was also observed in previous experimental studies and past investigations (2), including the Hastings bridge study.

In the horizontal tab configuration, if the bottom plate fractured, only that plate is assumed to fail, with the side plates and horizontally welded tabs remaining functional. However, if the side plate fractures, both the side plate and the horizontally welded tabs are considered fractured. In the vertical tab configuration, a fracture in the bottom plate leads to the failure of the plate and its welded vertical tabs, while the side plates continue to perform. If the side plate fractured in this configuration, the top and bottom plates with their bolted tabs remain effective. For the angle configuration, since the angles are bolted to both the top, bottom, and side plates without welding, they are assumed to remain intact regardless of which component fractures. This is also illustrated in Figure 61.

Although the global load transfer mechanism is preserved across all configurations, the local stress distribution, deformation behavior, and capacity of the TB can vary significantly depending on connection details. These differences are especially important under faulty conditions, as they influence how effectively TB can redistribute loads and maintain structural integrity. As a result, each configuration is analyzed independently for both strength and fatigue limit states to support the development of a reliable and generalized methodology for evaluating internal redundancy in fractured TBs.



Source: FHWA

**Figure 61. Illustration. Flowchart illustrating the assumed fracture scenarios and fractured plates with different corner connections.**

### 6.1.1 TB geometries considered for development of formulations

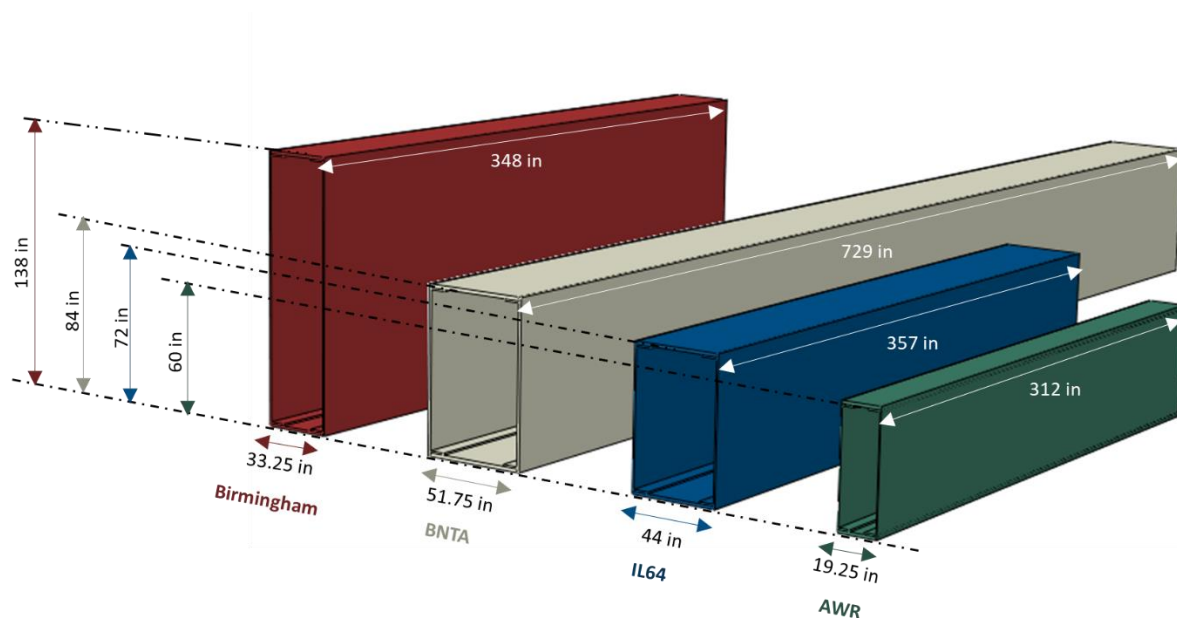
To support the development of simplified formulations for estimating the remaining capacity of fractured TBs, a range of TB geometries was analyzed using detailed submodeling techniques. This effort began with two in-service tied arch bridges for which global finite element models were developed: the Birmingham bridge and the AWR Bridge. To broaden the scope of the study and capture a wider spectrum of practical design configurations, TB cross-sections from two additional in-service bridges were also incorporated, the Illinois Route 64 (IL64) Bridge and the Blennerhassett Network Tied Arch (BNTA).

Thus, resulted in four distinct baseline TB geometries, each representing a unique set of geometric and detailing characteristics based on actual bridge designs. The baseline geometries are shown in the Figure 62, all drawn to the same scale. It can be readily observed that they exhibit very different geometric properties, such as section modulus. The figure depicts only the TB segment between two adjacent hangers, and the hanger spacing varies for each bridge, reflecting their individual design configurations.

To expand the dataset and support the development of robust formulation, nine additional TB geometries were created by varying the thicknesses of the component plates in the original four designs. These modifications were restricted to plate thickness, while the overall TB depth and width were kept constant to preserve the original cross-sectional proportions. This approach allowed for controlled variation in fracture-affected areas and facilitated a more comprehensive investigation of trends in faulty behavior.

The resulting 13 TB geometries were then analyzed for all three corner connections, horizontal tabs, vertical tabs, and angle connections. This expanded the dataset to a total of 39 unique TB configurations for each fracture scenario, covering a broad range of realistic design conditions. Each configuration was evaluated under both bottom plate and side plate fracture conditions to assess the influence of connection detailing on structural performance. The primary objective was to quantify the remaining capacity of faulted TBs, forming the basis for the development of simplified and reliable predictive formulations.

The geometries with tab-type corner connections are provided in Table 20, while with angle-type connections are listed in Table 21. It is important to note that in these tables, bridge names without a numeric suffix represent the original design geometries, whereas names with numeric suffixes refer to additional TB geometries that were created and analyzed as part of the extended dataset.



Source: FHWA

**Figure 62. Illustration. TB sections of four baseline geometries.**

**Table 20. TB geometries with tab-type corner connections**

<b>Bridge ID</b>	<b>Bottom / top plate width (inch)</b>	<b>Bottom/ top plate thickness (inch)</b>	<b>Bottom/ top plate area (inch<sup>2</sup>)</b>	<b>Side plate height (inch)</b>	<b>Side plate thickness (inch)</b>	<b>Side plate area (inch<sup>2</sup>)</b>	<b>Tab plate</b>
Birm	33.25	1.375	45.72	138.00	0.875	120.75	1"x8.125"
Birm-1	33.25	1.000	33.25	138.00	0.875	120.75	1"x8.125"
Birm-2	33.25	1.750	58.19	138.00	0.875	120.75	1"x8.125"
AWR	19.25	1.500	28.88	60.00	0.500	30.00	1"x6"
AWR-1	19.25	1.500	28.88	60.00	0.750	45.00	1"x6"
AWR-2	19.25	1.750	33.69	60.00	0.500	30.00	1"x6"
IL64	44.00	1.500	66.00	72.00	0.875	63.00	1"x8"
IL64-1	44.00	1.750	77.00	72.00	0.500	36.00	1"x8"
IL64-2	44.00	1.250	55.00	72.00	1.250	90.00	1"x8"
BNTA	51.75	1.750	90.56	84.00	1.500	126.00	1"x7.75"
BNTA-1	51.75	2.000	103.50	84.00	1.000	84.00	1"x7.75"
BNTA-2	51.75	1.875	97.03	84.00	0.750	63.00	1"x7.75"
BNTA-3	51.75	2.500	129.38	84.00	0.675	56.70	1"x7.75"

**Table 21. TB geometries with angle-type corner connections**

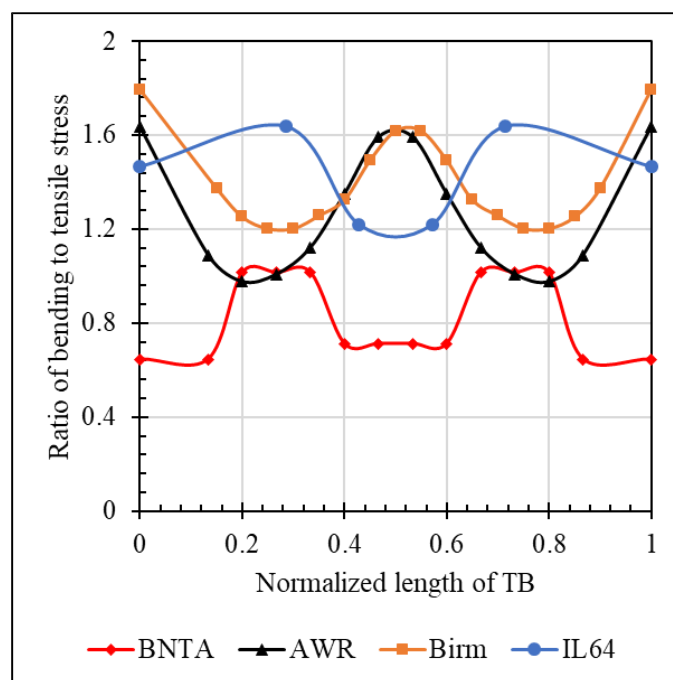
<b>Bridge ID</b>	<b>Bottom/ top plate width (inch)</b>	<b>Bottom/ top plate thickness (inch)</b>	<b>Bottom/ top plate area (inch<sup>2</sup>)</b>	<b>Side plate height (inch)</b>	<b>Side plate thickness (inch)</b>	<b>Side plate area (inch<sup>2</sup>)</b>	<b>Tab plate</b>
Birm	33.25	1.375	45.72	138.00	0.875	120.75	L8x8x1
Birm-1	33.25	1.000	33.25	138.00	0.875	120.75	L8x8x1
Birm-2	33.25	1.750	58.19	138.00	0.875	120.75	L8x8x1
AWR	19.25	1.500	28.88	60.00	0.500	30.00	L8x8x1
AWR-1	19.25	1.500	28.88	60.00	0.750	45.00	L8x8x1
AWR-2	19.25	1.750	33.69	60.00	0.500	30.00	L8x8x1
IL64	44.00	1.500	66.00	72.00	0.875	63.00	L8x8x1
IL64-1	44.00	1.750	77.00	72.00	0.500	36.00	L8x8x1
IL64-2	44.00	1.250	55.00	72.00	1.250	90.00	L8x8x1
BNTA	51.75	1.750	90.56	84.00	1.500	126.00	L8x8x1
BNTA-1	51.75	2.000	103.50	84.00	1.000	84.00	L8x8x1
BNTA-2	51.75	1.875	97.03	84.00	0.750	63.00	L8x8x1
BNTA-3	51.75	2.500	129.38	84.00	0.675	56.70	L8x8x1

## 6.2 DEVELOPMENT OF SIMPLIFIED METHODOLOGY

As described earlier that in the tied arch bridges, the TB is typically subjected to a combination of axial tension and bending moments. A review of existing bridge plans indicates that the proportion of these forces varies significantly, both among different bridges and along the length of an individual TB. This variability poses a challenge for evaluation, as no consistent axial-to-bending moment ratio can be applied universally.

Figure 63 illustrates this concept by presenting the ratio of bending stress to tensile stress along the normalized length of the TB for four in-service bridges: BNTA, AWR, Birm, and IL64. The x-axis represents the normalized TB length from one end to the other, while the y-axis shows the stress ratio at each location. The curves clearly demonstrate how the relationship between bending and axial stresses changes along the TB, not only from bridge to bridge but also within the same structure. In certain segments, bending stresses exceed axial stresses, whereas in others, axial tension is the dominant force. This non-uniform behavior highlights the need for a generalized evaluation method capable of capturing a wide range of loading conditions.

This complexity is further compounded by the need to account for material and geometric nonlinearity when evaluating fractured members. Performing FEA for every scenario is not practical for routine assessments. Therefore, the objective of this work is to develop a simplified yet reliable methodology that can be readily applied by engineers without requiring computationally intensive modeling.



Source: FHWA

**Figure 63. Graph. Ratio of bending to tensile stress along the length of the TB.**

Through the detailed evaluation of various TB geometries, a practical and effective approach was identified using the well-established axial load-moment (P-M) interaction curve. While this method is traditionally used for compression members, it has been adapted here for members

subjected to axial tension and bending. The interaction curve serves as a capacity envelope, illustrating the maximum permissible combinations of axial force and bending moment that a TB can resist in each faulted condition.

To account for the effects of fracture, separate interaction curves are developed for the TB in its faulty state. A fracture in the bottom plate reduces the TB's axial and flexural resistance by eliminating a significant portion of the cross-section that contributes to load-carrying capacity. Similarly, a fracture in the side plate reduces the TB's capacity due to the loss of structural continuity and area. These effects are captured in the modified interaction curves for the fractured conditions.

Nonlinear material properties and geometric nonlinearity were included in the analysis to accurately reflect the post-fracture behavior of the TB. Once the interaction curve for the fractured TB is established, the remaining capacity can be evaluated by plotting the factored design loads using the Redundancy II load combination, as suggested in the AASHTO IRM Guide Spec. (6). If the point representing the applied axial force and bending moment lies within the interaction curve, the TB is considered capable of carrying the design loads despite the fracture. If the point lies outside the curve, it suggests that the remaining capacity has been exceeded.

This simplified P-M interaction approach provides a practical tool for estimating the post-fracture strength of TBs without requiring detailed FEA for each case. However, for it to serve as a meaningful evaluation framework, a clear failure criterion should be established. This criterion is necessary to determine the threshold beyond which the TB should be considered incapable of safely resisting service loads, and to inform when further analysis or intervention should be performed.

### **6.2.1 Failure criterion**

To plot the P-M interaction curve for a given combination of axial load and bending moment, it is essential to first establish a consistent failure criterion that can be applied across all TB geometries. This criterion is also critical for halting the Abaqus analysis at the correct stage, ensuring that the simulation ends at a meaningful point where the remaining capacity can be evaluated. A failure criterion is necessary to identify the load level at which local strains, typically near a bolt hole, exceed tolerable limits. When this occurs, failure of the remaining intact components adjacent to the fracture could be imminent. After reviewing experimental test data from previous studies, tension coupon results, and conducting nonlinear FE simulations, a simple and effective criterion was adopted.

For this analysis, the net-section fracture criterion was adopted in accordance with AASHTO and AISC design provisions. This criterion limits the load based on the net section area, which is the gross area reduced by any holes or fractures. The corresponding net-section fracture resistance, as defined in LRFD Design Article 6.8.2, assumes that the ultimate tensile strength uniformly applies over this net area. This simplification allows for a practical estimation of axial tension capacity while maintaining consistency with standard design practices. While this assumption does not account for localized strain concentrations near discontinuities such as bolt holes, it is widely accepted in structural steel design. ASTM A709 steels used in bridges are known to

tolerate such localized effects, making this assumption both practical and conservative. To validate this approach for use in TB analysis, a preliminary FE simulation was conducted using a simple plate with a single hole subjected to axial tension. The limiting strain at the factored net-section fracture load was recorded, using a resistance factor of 0.8 in line with AASHTO LRFD BDS Article 6.5.4.2. A mesh sensitivity study revealed that using a mesh size of 0.13 inches around the hole and 1 inch elsewhere with quadratic shell elements produced consistent strain results. This mesh refinement was adopted in all TB models.

In Abaqus, the unfractured TB submodels were subjected to axial tension under AASHTO LRFD BDS loading provisions until the net-section fracture load was reached, as defined in AASHTO LRFD BDS Article 6.8.2. The load was applied incrementally until this threshold was achieved, at which point the analysis was terminated. The resulting strain values at the bolt holes in the TB submodels closely matched those observed in the plate-with-hole validation model, confirming the suitability of the plate-derived strain as the failure limit across different TB geometries.

The analysis was specifically carried out for the TBs from the four in-service bridges (BNTA, IL64, AWR, and Birm) previously mentioned, for which the bending-to-tensile stress ratios were presented earlier. These TBs were transformed with all three corner connection types (horizontal tab, vertical tab, and angle) and subjected to net-section fracture load, and the resulting strain at the hole was recorded. These strain values are provided in Table 22. The strains ranged from approximately 0.11 to 0.14 depending on geometry and detailing. Structural steels generally demonstrate elongation at fracture of 20%, and these plastic strain values indicate that localized fracture around bolt hole should not be occurring. These differences in the values for different bridges and geometries primarily stem from differences in connection detailing and the influence of local geometry on stress concentrations around the holes. However, the use of a consistent mesh across all models ensured that these differences did not compromise the comparability of strain values, which confirms that the strain measurements are consistent and valid across different TB geometries, despite variations in detailing and geometry. Based on this methodology, the following sections develop the P-M interaction curves used to assess the structural capacity of fractured TBs under combined axial and bending loads.

**Table 22. Limiting plastic strains for different TB geometries**

<b>Bridge ID</b>	<b>Plastic strain, horizontal tabs</b>	<b>Plastic strain, vertical tabs</b>	<b>Plastic strain, angles</b>
Birm	0.142	0.148	0.144
AWR	0.124	0.141	0.141
IL64	0.120	0.118	0.112
BNTA	0.123	0.117	0.131

### **6.2.2 Critical plate: In the context of a fractured TB**

In the context of a fractured TB, the critical plate is the component that governs the structural response after a fracture occurs and ultimately determines the remaining capacity under applied loads. When a fracture initiates, the load redistribution causes a shift in stress demands, making it

essential to identify which plate becomes most stressed. This critical plate is where strain limits are first reached and thus the analysis is subsequently stopped.

For the same fracture scenario, the critical plate may differ depending on the corner connection geometry. For example, in a horizontal tab configuration with a bottom plate fracture, the tab plate that is welded to the side plate becomes the critical plate, as it is forced to carry a larger portion of the load previously resisted by the bottom plate. In contrast, when the side plate is fractured, both the side plate and welded tab are considered ineffective, resulting in the bottom plate becoming the critical plate due to its increased role in carrying the redistributed load.

Once the critical plate is identified, the analysis focuses on the hole(s) adjacent to the fracture in that plate. This location typically experiences the highest localized strain. The analysis continues under applied loads in the faulted state until the strain at this location reaches the failure strain. This limit corresponds to the net-section fracture strain derived from the unfractured TB analysis. At that point, the simulation is terminated, and the axial and bending load combination at that stage is recorded as the remaining capacity of the fractured section.

### **6.3 P-M INTERACTION CURVE FOR A FRACTURED TB**

To develop P-M interaction curves for fractured TB sections, shell element-based submodels were created following the approach described in Chapter 2. A total of 13 distinct cross-sectional geometries were examined, each independently analyzed for three previously mentioned corner connection types: horizontal tabs or vertical tabs (Table 20) and angle connections (Table 21).

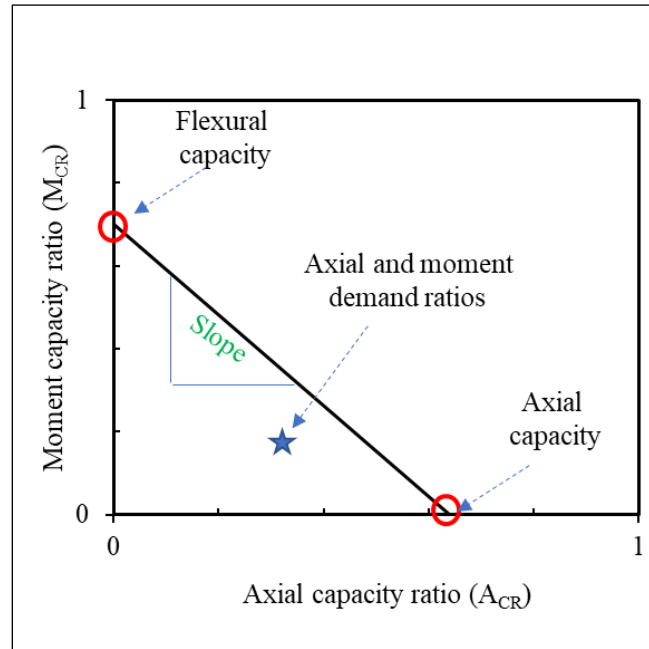
For each configuration, two fracture scenarios were considered: one involving complete fracture of the bottom plate and the other involving complete fracture of the side plate. This resulted in 39 unique TB configurations for each fracture scenario, enabling a detailed evaluation of how variations in geometry and connection detailing influence the structural response of faulted TBs subjected to combined axial and bending loads. This analysis directly supports the core objective of this report, which is to develop simplified and practical formulations for estimating the remaining capacity of fractured TBs.

Each P-M interaction curve was constructed by first evaluating two bounding load cases. In the first case, a pure axial load was applied to determine the axial capacity of the fractured section. In the second, a pure bending moment was applied to determine the flexure capacity. For every load case, the analysis was terminated when the critical plate reached a fracture limit state-based failure strain criterion at the bolt hole.

To complete the full P-M interaction curve, additional simulations were performed with combined axial and bending loads. The ratio of axial to moment loads varied incrementally, for example 10% axial and 90% moment, 20% axial and 80% moment, and so on. These loads were applied in two sequential steps within the finite element model. The axial load was applied in the first step, followed by the bending moment in the second step. Since these capacity estimates are derived from nonlinear FE analysis, the results inherently captured key effects such as geometric non-linearity, local yielding and redistribution of internal stresses. Path dependence of the sequential loads was not influential as is discussed later in Section 6.3.2. A representative P-M interaction curve for a fractured TB is shown in Figure 64. The P-M interaction curve serves as a



capacity envelope for the fractured TB, providing a basis for determining whether a given combination of axial force and bending moment can be sustained after a fracture occurs. Any demand ratio that falls below the curve is considered safe, while ratios that fall on or above the curve indicate insufficient remaining capacity. To evaluate the performance of a fractured TB in accordance with internal redundancy approach, the design demands are checked against the P-M interaction curve using the appropriate Redundancy-II load factors.



Source: FHWA

**Figure 64. Graph. Typical P-M curve of a fractured TB.**

## 1.1 Evaluation of TBs with horizontal tab connections

The evaluation began with the analysis of TBs incorporating horizontal tab connections. In this configuration, the tabs are welded to the side plates and bolted to the top and bottom plates. A representative cross section of this connection type is shown in Figure 60(a).

### 6.3.1 Bottom plate fracture condition

All 13 TB geometries, presented in Table 20, were assessed using this connection detail, with the analysis focused on the scenario involving a complete fracture of the bottom plate.

As outlined in the methodology, the evaluation began with two bounding load cases. First, each fractured model was analyzed under pure axial loading to establish the axial capacity of the faulted section. Second, the same model was subjected to pure bending to determine its flexural capacity in the fractured state. These bounding cases were analyzed using single-step simulations. Following these initial assessments, a series of combined loading scenarios was simulated to generate the full P-M interaction curves. In these cases, a two-step FEA procedure was used: axial tension was applied in Step 1, followed by bending moment in Step 2.

The applied load combinations for the BNTA geometry are summarized in Table 23. For combined loading conditions, the model identifier begins with the prefix “A”, indicating axial loading as the first step in the analysis, followed by a numerical value representing the magnitude of axial stress (ksi) applied in the first step. For instance, model “A5” refers to a case where 5 ksi axial stress was applied, followed by bending until the failure criterion was reached. The maximum axial stress considered was 30 ksi (model A30), determined based on the remaining axial capacity of the faulted TB under pure axial loading, calculated as  $0.643F_y$ , or approximately 32.15 ksi, as shown in Figure 65. Load cases exceeding this threshold were not modeled, as they surpassed the capacity of the faulted section and would not yield useful results.

While the loads were applied to fractured geometries, the associated stress magnitudes were computed using the unfractured cross-sectional properties, including area ( $A$ ), moment of inertia ( $I$ ), and centroidal distance ( $y$ ). This allowed for consistent normalization and facilitated meaningful comparison across the different TB configurations.

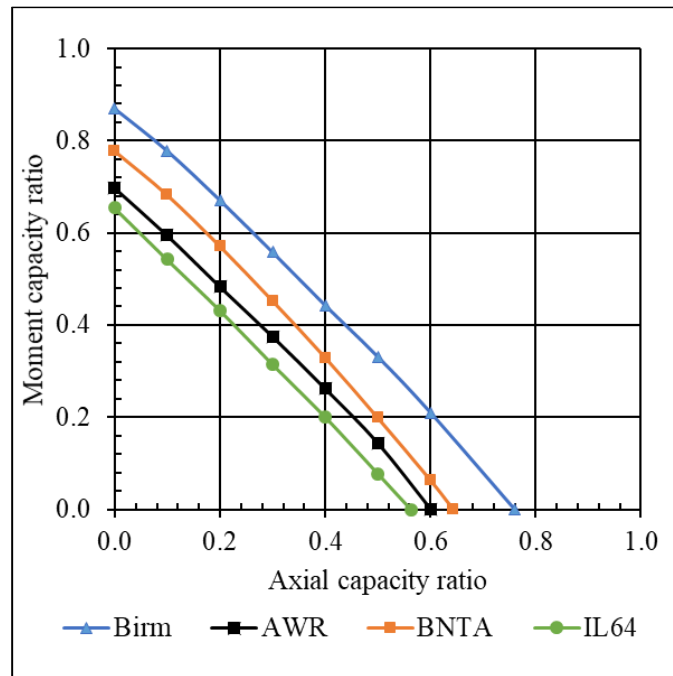
The failure criterion was established as the strain limit at the bolt hole in the critical plate. These strain thresholds, presented in Table 22, served as the termination condition for all simulations. When this limit was reached, the corresponding axial force and bending moment were recorded as the remaining capacity of the TB section in the fractured state. These capacity values were then normalized by the yield axial and flexural capacities of the unfractured sections and used to construct the P-M interaction curves.

The resulting curves for the baseline geometries under the bottom plate fracture scenario are presented in Figure 65. These plots illustrate the residual axial and bending capacities relative to the intact design capacities. Because normalization references the unfractured section properties, the interaction curves do not reach a value of 1.0 along the pure axial or bending axes.

It is important to note that the P-M interaction curves for all baseline geometries exhibit a consistent overall trend and show a nearly linear slope between the pure axial and pure bending capacity limits. This suggests a predictable relationship between combined loading conditions and remaining strength for fractured TBs. However, to draw meaningful conclusions and verify whether this behavior is inherent to all TB geometries, it is necessary to conduct a systematic evaluation across the entire set of 13 geometries. By applying a uniform modeling approach and maintaining consistency in loading, failure criteria, and normalization procedures, the influence of geometry, fracture extent, and connection type can be fully understood, supporting the development of a generalized predictive formulation for faulted capacity.

**Table 23. The applied loads for the BNTA geometry**

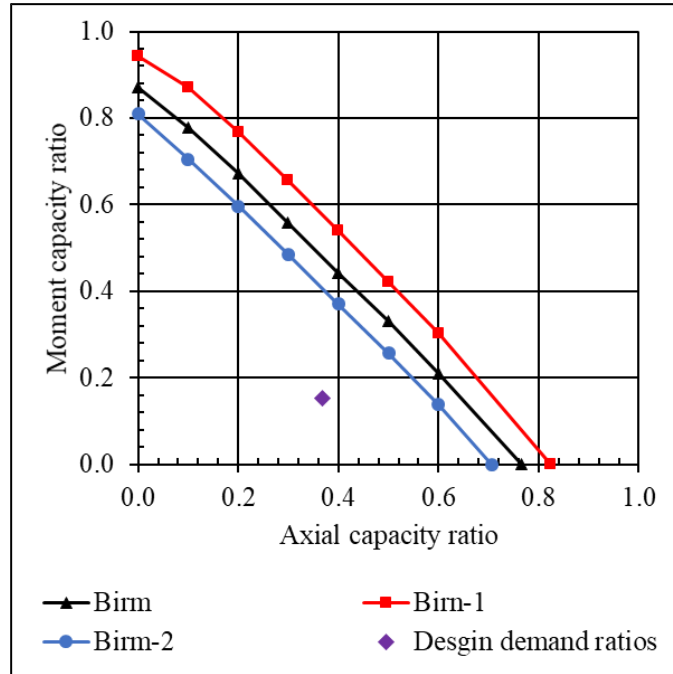
Model ID	Axial stress (ksi)	Force (kips)	Flexural stress (ksi)	Moment (kip-inch)
Pure bending	0	0	50	610,938
A5	5	2,321	45	549,844
A10	10	4,641	40	488,750
A15	15	6,962	35	427,656
A20	20	9,283	30	366,563
A25	25	11,603	25	305,469
A30	30	13,924	20	244,375
Pure axial	50	23,210	0	0



Source: FHWA

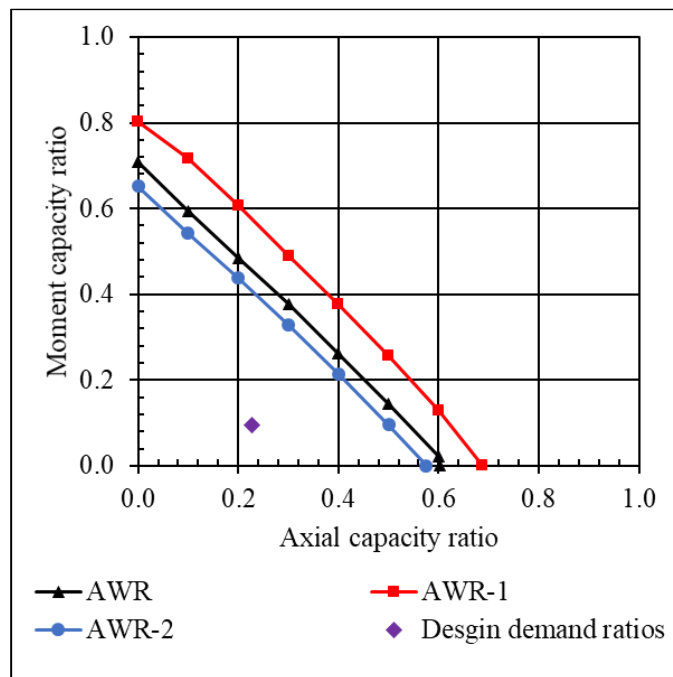
**Figure 65. Graph. P-M curve for bottom plate fractured TBs with horizontal tab connections.**

P-M interaction curves for the bottom plate fracture scenario are presented for all 13 TB geometries in the figures below. Figure 66 shows the results for the Birmingham geometries, Figure 67 presents the outcomes for AWR, and the corresponding curves for BNTA and IL64 are provided in Figure 68 and Figure 69, respectively. The percentage of cross-sectional areas fractured in each geometry under the bottom plate fracture condition is summarized in Table 24.



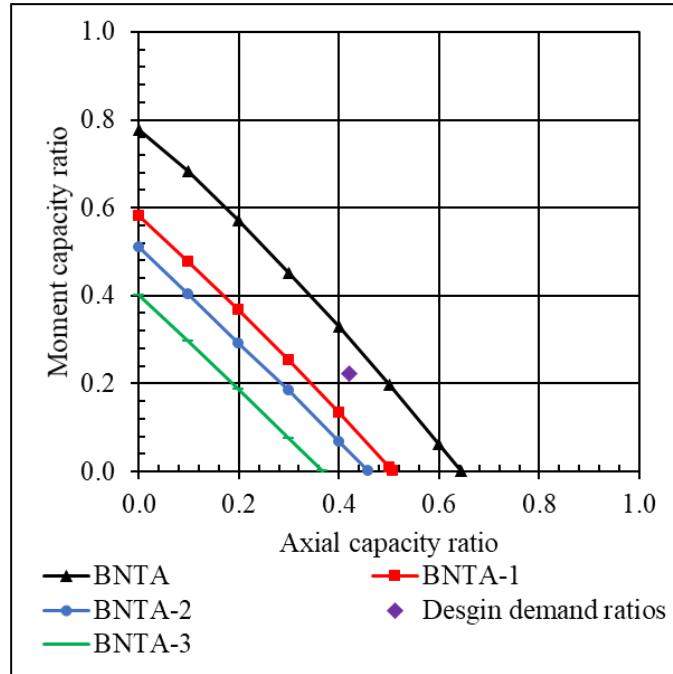
Source: FHWA

**Figure 66. Graph. P-M curve for bottom plate fractured Birmingham TBs with horizontal tab connections**



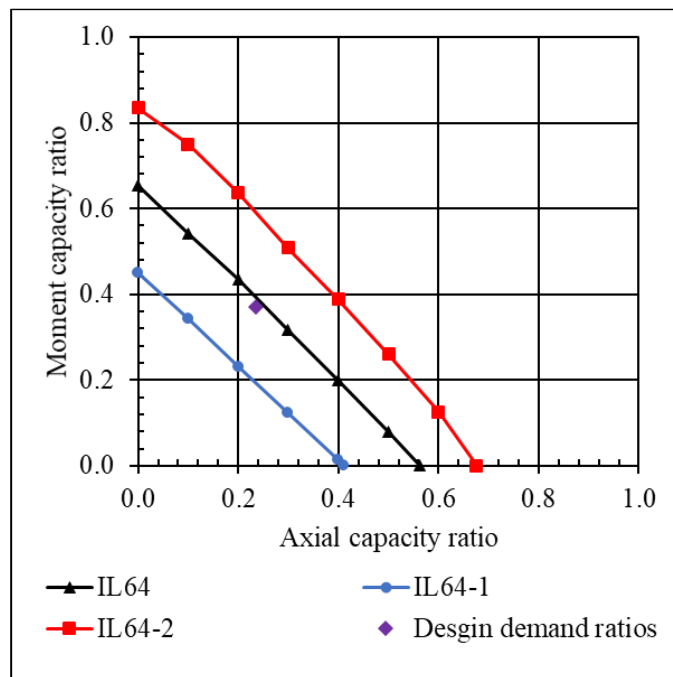
Source: FHWA

**Figure 67. Graph. P-M curve for bottom plate fractured AWR TBs with horizontal tab connections**



Source: FHWA

**Figure 68. Graph. P-M curve for bottom plate fractured BNTA TBs with horizontal tab connections**



Source: FHWA

**Figure 69. Graph. P-M curve for bottom plate fractured IL64 TBs with horizontal tab connections**

**Table 24. Percentage fractured area for the TBs with horizontal tabs under bottom plate fracture conditions**

<b>Bridge ID</b>	<b>Fractured area (%)</b>
Birm	12.51
Birm-1	9.77
Birm-2	14.91
AWR	20.37
AWR-1	16.81
AWR-2	22.26
IL64	22.76
IL64-1	29.84
IL64-2	17.08
BNTA	19.51
BNTA-1	25.49
BNTA-2	27.64
BNTA-3	32.09

In each figure, the black line represents the as-built (original) geometry, while the red and blue lines denote the modified geometries used to evaluate the influence of different fracture areas. Specifically, for Birmingham, AWR, and IL64 TBs, the red lines correspond to modified configurations with larger fractured areas, and the blue lines indicate those with smaller fractured areas relative to the as-built section. As observed, geometries with smaller fractured areas (blue lines) generally retain higher remaining capacity, while those with larger fracture extents (red lines) show reduced capacity.

For the BNTA TB, all modified configurations were developed with larger fractured areas than the original geometry. As a result, both red and blue lines for BNTA lie consistently below the black line, confirming a decrease in remaining capacity due to the increased extent of damage.

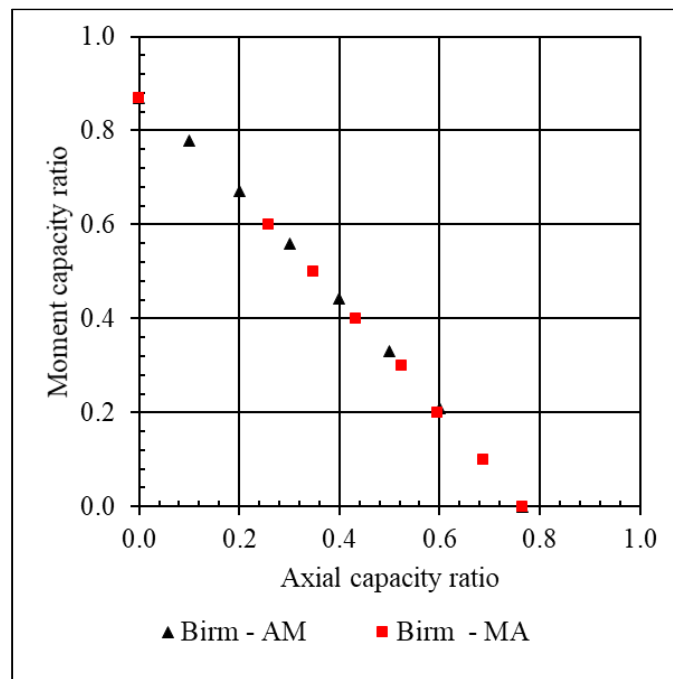
Each plot also includes a purple diamond, indicating the demand point associated with the Redundancy-II load combination, incorporating both axial force and bending moment. If this point lies beneath the P-M curve, the TB is considered to meet the internal redundancy criterion for strength under the given loading condition.

In conclusion, the results clearly demonstrate that the percentage of areas affected by fracture plays a critical role in determining the remaining structural capacity of a TB. Smaller fractured regions tend to preserve a greater portion of the original capacity, while larger fractured areas substantially reduce the faulted strength. Thus, hinting that any proposed formulation to estimate the remaining capacity should be considered for the area fractured.

### **6.3.2 Impact of changing loading sequence**

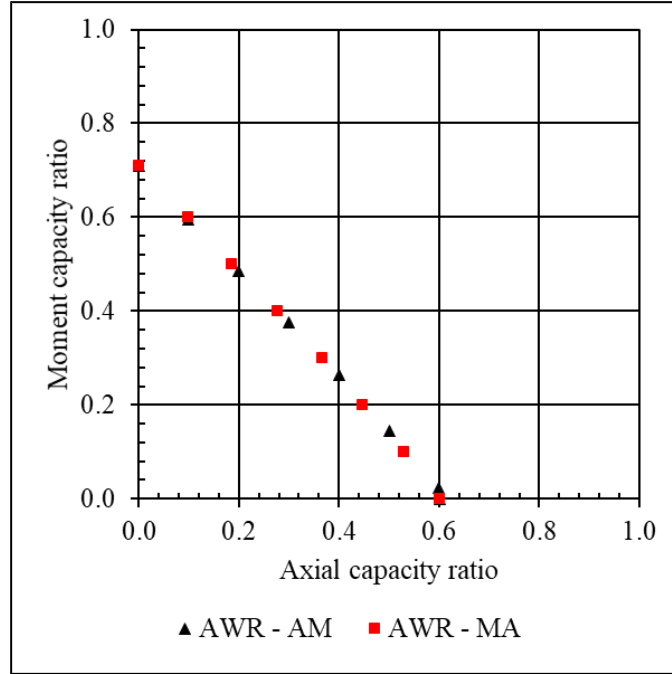
The results discussed in the previous section were obtained from analyses in which axial load was applied first, followed by bending moment. To assess whether the sequence of loading

affects the predicted remaining capacity of fractured TBs, an additional study was conducted using the original geometries of the AWR and Birmingham Bridges. In this study, the loading sequence was reversed: bending moment was applied first, followed by axial load. The results for both loading sequences are presented in Figure 70 and Figure 71. In these figures, "AM" denotes the case where axial load is applied first and moment in second step, while "MA" refers to the reversed sequence with moment applied first and axial load second. A comparison of the P-M interaction curves for each case reveals no meaningful difference between the two sequences. The curves are nearly identical, indicating that the order of loading does not influence the remaining capacity. This behavior is likely attributed to any material nonlinearity being very isolated, not affecting the majority the cross-section where it is occurring, hence the lack of load path dependence. This confirms that the selected loading sequence can be applied consistently across all simulations without compromising the accuracy or validity of the results.



Source: FHWA

**Figure 70. Graph. Impact of loading sequence on the P-M curve of bottom plate fractured Birmingham Bridge.**



Source: FHWA

**Figure 71. Graph. Impact of loading sequence on the P-M curve of bottom plate fractured AWR Bridge.**

### 6.3.3 Development of simplified methodology for bottom plate fractured TBs with horizontal tab connections

As discussed in previous sections, all P-M interaction curves were initially developed using nonlinear FEA. The next objective was to establish a simplified method for constructing these curves without the need for detailed computational modeling. Several geometric and sectional parameters such as moment of inertia, TB depth, and plate area distribution were explored as potential predictors. However, none of these parameters consistently yielded a closed-form solution suitable for estimating the moment capacity at various levels of axial load across all geometries.

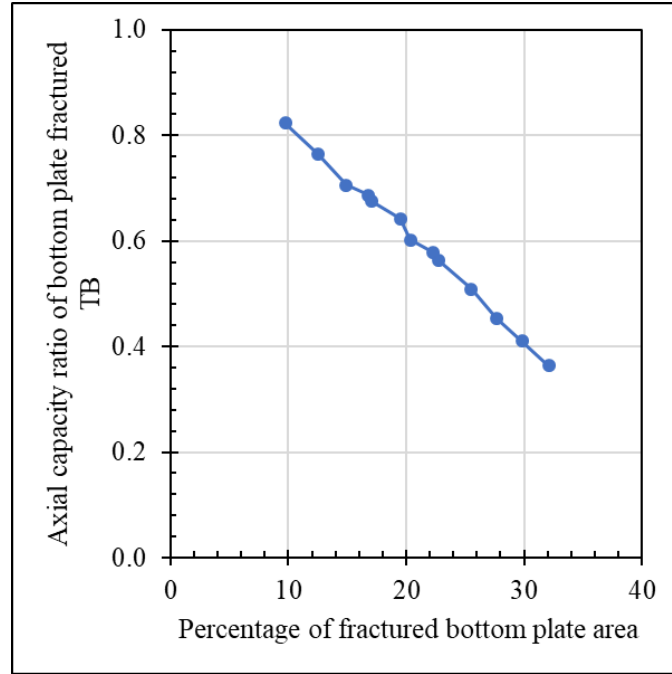
While moment capacity proved difficult to estimate directly, a clear and consistent relationship was observed between the remaining axial capacity and the percentage of the fractured bottom plate as noticed earlier. As illustrated in Figure 72, this relationship was effectively linear across all thirteen geometries. Specifically, the axial capacity was found to decrease proportionally with increasing fracture area, assuming zero applied bending. This trend provided the foundation for a simplified predictive model. Based on this observation, a linear equation was formulated to estimate the remaining axial capacity ratio ( $C_{Axial}^{BP}$ ) under a bottom plate fracture scenario as a function of the percentage of fractured cross-sectional area ( $A\%_{Frac}$ ):

$$C_{Axial}^{BP} = 1 - 2.0A\%_{Frac} \quad (5.1)$$

This equation allows for direct estimation of the axial capacity in the faulted state using only the percentage of the gross area lost due to fracture. Table 25 presents a comparison between the axial capacity ratios from FEA (column 2) and those estimated using the above equation (column



3). The percentage differences are also shown and are generally small, supporting the accuracy of the proposed method.



Source: FHWA

**Figure 72. Graph. Normalized remaining axial capacity in relation to bottom plate % fractured area.**

To extend the approach to moment capacity, the slopes of the P-M curves derived from FEA were examined. Despite the geometric diversity of the TBs, these slopes were remarkably consistent. Column 5 of Table 25 lists the individual slope values, and the average slope across all thirteen geometries was calculated to be approximately 1.15. Using this average slope and the estimated axial capacity ratio, the remaining moment capacity ratio ( $C_{Flex}^{BP}$ ) can be determined as:

$$C_{Flex}^{BP} = 1.15C_{Axial}^{BP} \quad (5.2)$$

The estimated moment capacities based on this equation are listed in column 6 of Table 25, along with the percentage differences from the FEA results in the final column. These differences were found to be generally conservative, further validating the reliability of the simplified method.

In summary, this simplified approach provides a practical and reasonably accurate means of estimating both axial and flexural capacities in bottom plate fractured TBs with horizontal tabs at corner connection.

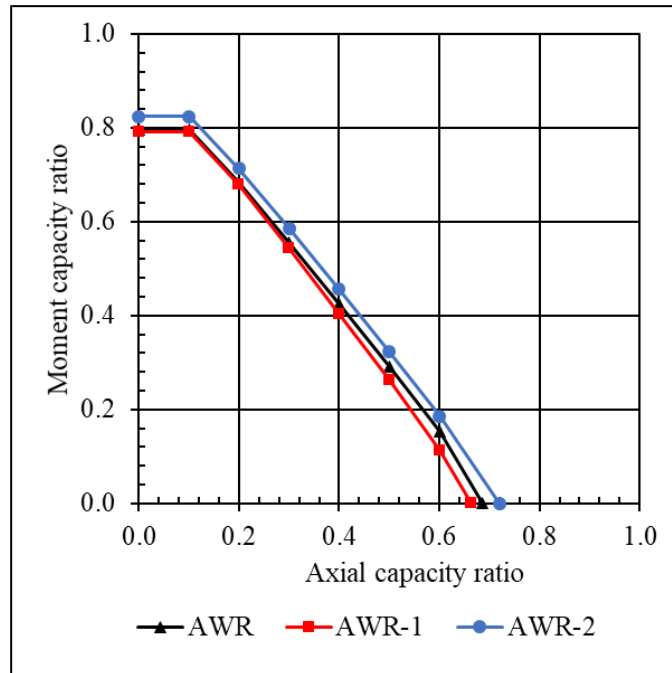
**Table 25. Estimation and comparison of P-M interaction curve parameters with the FEA values for a bottom plate fractured TB with horizontal tabs at corner connection**

Bridge ID	FEA axial capacity ratio	Est. axial capacity ratio (Eq. 5.1)	Diff. (%)	FEA moment capacity ratio	Est. moment capacity ratio (Eq. 5.2)	Diff. (%)
Birm	0.77	0.75	-2.03	0.87	0.86	-0.98
Birm-1	0.82	0.80	-2.22	0.94	0.92	-1.85
Birm-2	0.71	0.70	-0.57	0.81	0.81	-0.31
AWR	0.60	0.59	-1.64	0.71	0.68	-4.03
AWR-1	0.69	0.66	-3.34	0.80	0.76	-5.00
AWR-2	0.58	0.55	-4.14	0.65	0.64	-2.25
IL64	0.56	0.54	-3.16	0.66	0.63	-4.43
IL64-1	0.41	0.40	-1.71	0.45	0.46	2.77
IL64-2	0.68	0.66	-2.50	0.84	0.76	-9.42
BNTA	0.64	0.61	-5.14	0.78	0.70	-9.97
BNTA-1	0.51	0.49	-3.67	0.58	0.56	-3.01
BNTA-2	0.45	0.45	-1.52	0.51	0.51	-0.75
BNTA-3	0.36	0.36	-1.63	0.40	0.41	2.51

#### 6.3.4 Side plate fracture condition

In addition to analyzing bottom plate fractures for the horizontal tab configuration, the structural performance of TBs was also evaluated for scenarios involving complete fracture of the side plate and the welded tab plates. As mentioned earlier, tabs are assumed to fracture along with the plates to which they are welded. In the case of horizontal tab connections, since the tabs are welded to the side plates, a fracture in the side plate is modeled to include the failure of the attached tabs as well.

Figure 73 shows the remaining capacity curves based on axial force and bending moment combinations for the AWR bridge geometry. The horizontal plateau observed in the curve will be explained later in this section. While only one example is presented here, the overall trends were found to be similar for the remaining TB geometries.



Source: FHWA

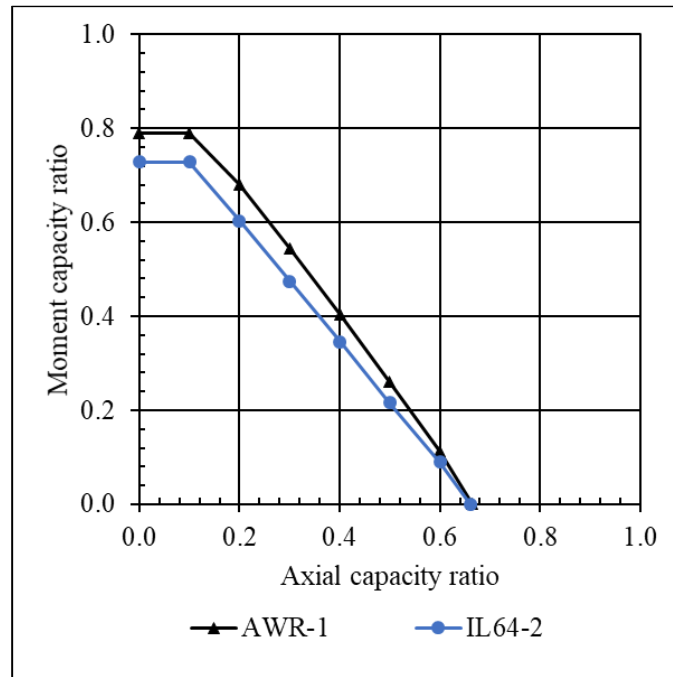
**Figure 73. Graph. P-M curve for side plate fractured AWR TB with horizontal tab connection.**

As in the bottom plate fracture case, the residual capacity was influenced by the percentage of cross-sectional areas fractured. However, a new factor was identified in this scenario; the total width of the TB. Figure 74 illustrates this effect using the AWR-1 and IL64-2 geometries. Although both sections had approximately 33% of their cross-sectional area fractured, the slope of the interaction curve varied between the two. This variation is attributed to the difference in TB width, which was 19.25 inches for AWR-1 and 44.00 inches for IL64-2. The wider IL64-2 geometry exhibited lower residual flexural strength, likely due to increased susceptibility to local eccentricity effects caused by the non-uniform distribution of stresses near the fracture.

An additional observation under this fracture scenario was the occurrence of local buckling in the top plate when the TB was subjected to pure bending without any axial tension. Figure 75 illustrates this behavior for the BNTA-2 geometry, where the application of a strong-axis moment alone led to visible buckling in the top plate. This behavior is attributed to localized compressive stresses concentrated near the fractured edge of the side plate. Because the fracture disrupts the uniform stress flow, compressive forces are concentrated more heavily on one side of the section, causing localized instability. However, when even a small amount of axial tension (for example, 5 ksi) was applied prior to bending, the buckling behavior was suppressed, as shown in Figure 76. The axial force reduced the effect of the local compression in the top plate and helped maintain stability.

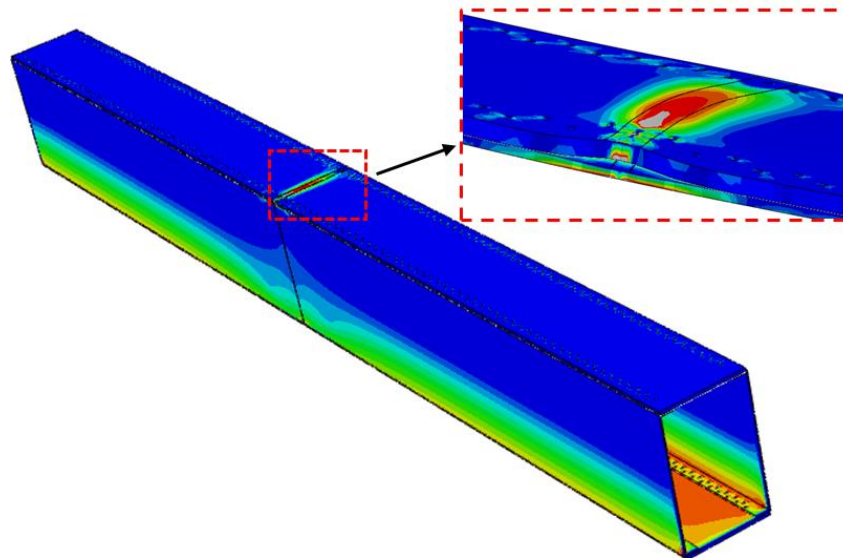
Since TBs in tied arch bridges generally remain in axial tension under service conditions, it is reasonable to assume that buckling of the top plate is unlikely to occur in practice. Based on this observation, the flexural capacity under side plate fracture should be evaluated with a small level

of axial tension applied. This assumption provides a more accurate representation of in-service behavior.



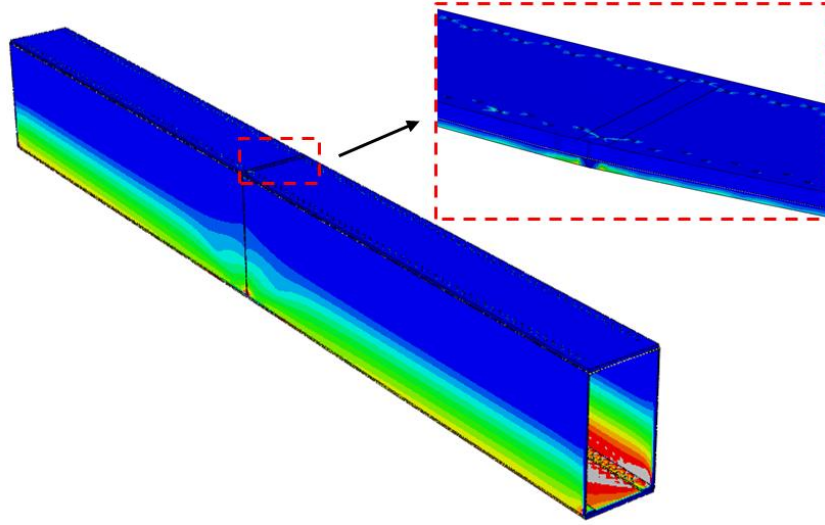
Source: FHWA

**Figure 74. Graph. P-M curve for side plate fractured TB geometries with 33% fractured area.**



Source: FHWA

**Figure 75. Illustration. Side plate fractured BNTA-2 geometry subjected to pure bending (deformations in inset figure are magnified 5 times).**



Source: FHWA

**Figure 76. Illustration. Side plate fractured BNTA-2 geometry subjected to 5 ksi of tensile and bending stresses (deformations in inset figure are magnified 5 times).**

### 6.3.5 Development of simplified methodology for outer plate fractured TBs with horizontal tab connections

Similar to the bottom plate fracture, the remaining axial capacity of the side plate fractured TB was noticed to be influenced by the percentage of area fractured ( $A_{\%Frac}$ ). The relationship is captured by the empirical expression:

$$C_{Axial}^{SP} = 1 - 1.17A_{\%Frac} \quad (5.3)$$

where  $A_{\%Frac}$  is the percentage of the gross cross-sectional area removed due to the fracture and given in Table 26.

To mitigate the potential for local buckling in the top plate under pure bending, the P-M curve is conservatively flattened beyond the point at which the section reaches the failure strain under a minimum axial tension of 5 ksi in conjunction with bending. Once the axial capacity ratio is known, the remaining flexural capacity ratio is proposed to be estimated using a slope of 1.07 (with 5 ksi axial load) can be estimated as follows:

$$C_{Flex}^{SP} = 1.07C_{Axial}^{SP} \quad (5.4)$$

Table 27 presents a comparison between the axial capacity ratios obtained from FE analysis in column 2 and those estimated using the proposed empirical expression in column 3 for the side plate fracture scenario. The percentage differences are also included in the table and are generally small, indicating strong agreement between the estimated values and those derived from FE analysis. This consistency supports the reliability of the simplified method for predicting the remaining axial capacity. A negative percentage difference indicates that the proposed correlations underpredict the strength compared to the FE results, whereas a positive difference signifies that the correlations overpredict the fractured TB section strength relative to the FE models.

Similarly, the flexural capacity ratios estimated using the proposed expression are compared with the FEA results in columns 5 and 6. A higher discrepancy was observed for the Birmingham bridge geometries. This can be attributed to the relatively large fracture areas in these geometries, which range from 35 percent to 40 percent of the total cross-sectional area. Such a disproportionate area loss from a single plate fracture is expected to significantly influence the structural response. Based on this finding, the presented simplified approach should not be applied to cases where the fracture of a single plate results in more than 30 percent loss of the total cross-sectional area.

Excluding the Birmingham cases, the estimated results for the other bridge geometries showed reasonable agreement with FEA predictions. These findings demonstrate that the proposed method offers a practical and sufficiently accurate alternative to detailed numerical simulations for evaluating the residual strength of TBs under side plate fracture conditions.

**Table 26. Percentage fractured area for the TBs with horizontal tabs under side plate fracture conditions**

<b>Bridge ID</b>	<b>Fractured area (%)</b>
Birm	37.49
Birm-1	40.23
Birm-2	35.09
AWR	29.63
AWR-1	33.19
AWR-2	27.75
IL64	27.24
IL64-1	20.16
IL64-2	32.92
BNTA	30.49
BNTA-1	24.51
BNTA-2	22.36
BNTA-3	17.91

**Table 27. Estimation and comparison of P-M interaction curve parameters with the FEA values for a side plate fractured TB with horizontal tabs at corner connection**

Bridge ID	FEA axial capacity ratio	Est. axial capacity ratio (Eq. 5.3)	Diff. (%)	FEA moment capacity ratio	Est. moment capacity ratio (Eq. 5.4)	Diff. (%)
Birm	0.60	0.56	-6.13	0.63	0.60	-4.69
Birm-1	0.53	0.53	0.60	0.54	0.57	5.51
Birm-2	0.63	0.59	-5.79	0.69	0.63	-8.30
AWR	0.64	0.65	2.72	0.67	0.70	4.53
AWR-1	0.61	0.61	-0.03	0.66	0.65	-1.15
AWR-2	0.66	0.68	2.04	0.70	0.72	3.56
IL64	0.70	0.68	-2.66	0.75	0.73	-2.25
IL64-1	0.77	0.76	-0.96	0.78	0.82	4.45
IL64-2	0.63	0.61	-1.97	0.66	0.66	-0.99
BNTA	0.60	0.64	7.22	0.70	0.69	-2.14
BNTA-1	0.70	0.71	2.28	0.76	0.76	0.65
BNTA-2	0.72	0.74	2.88	0.76	0.79	3.35
BNTA-3	0.79	0.79	-0.57	0.82	0.85	3.41

#### 6.4 EVALUATION OF TBS WITH VERTICAL TAB CONNECTIONS

For the vertical tab connections, the same methodology used for the horizontal tab configuration was applied. Submodels were developed using an identical approach to ensure consistency in the analysis framework. In this configuration, the vertical tabs are welded to the top and bottom plates and bolted to the side plates. Therefore, when the bottom plate is assumed to be fractured, the attached vertical tabs were also considered fractured in the model. As a result, the percentage of cross-sectional areas affected by the bottom plate fracture is higher for the vertical tab configuration compared to the horizontal tab configuration.

In contrast, under the side plate fracture scenario, only the side plates were assumed to be fractured, while the vertical tabs remained intact. Consequently, the percentage of area fractured in this scenario is lower than that in the corresponding horizontal tab configuration. The specific fractured area percentages for each geometry under both scenarios are summarized in Table 28.

All thirteen TB geometries were analyzed using the vertical tab connection configuration, and the results were found to be consistent with those observed for the horizontal tab configuration. For the baseline geometries, the P-M interaction curves under the bottom plate fracture scenario are presented in Figure 77, while the corresponding results for the side plate fracture scenario are shown in Figure 78.

It is important to note that under the bottom plate fracture condition, the IL64 and AWR geometries exhibited nearly identical P-M interaction curves. This similarity is attributed to both geometries experiencing approximately 28% loss in cross-sectional areas due to the fracture. A

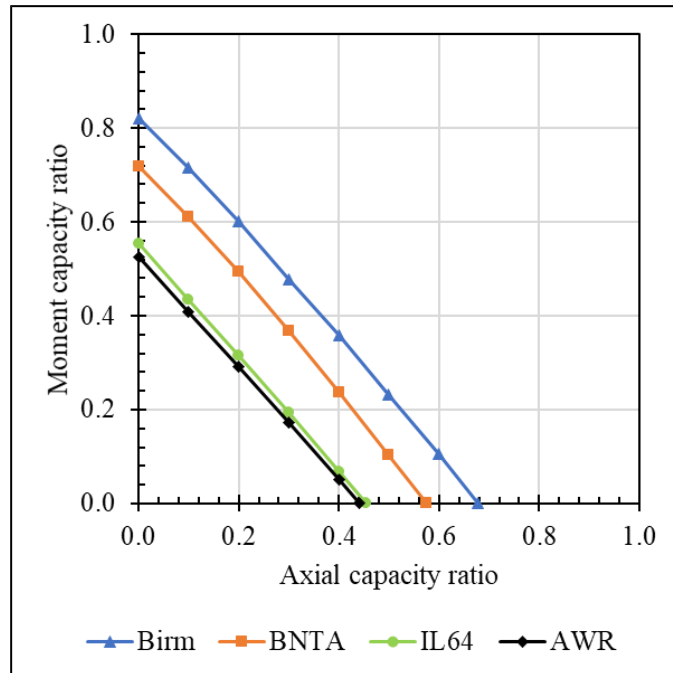
similar observation was made for the side plate fracture condition, where the BNTA and Birmingham geometries also showed comparable P-M curves, corresponding to closely matched percentages of fractured area.

Although these geometries differ significantly in other characteristics such as overall depth, flange width, and moment of inertia, the consistent behavior across these cases indicates that the percentage of area lost due to fracture plays a dominant role in determining the remaining capacity. These results suggest that fractured area percentage is a key parameter in assessing the residual strength of TBs, independent of the specific corner connection configuration.

**Table 28. Percentage area fractured for different TB corner connections**

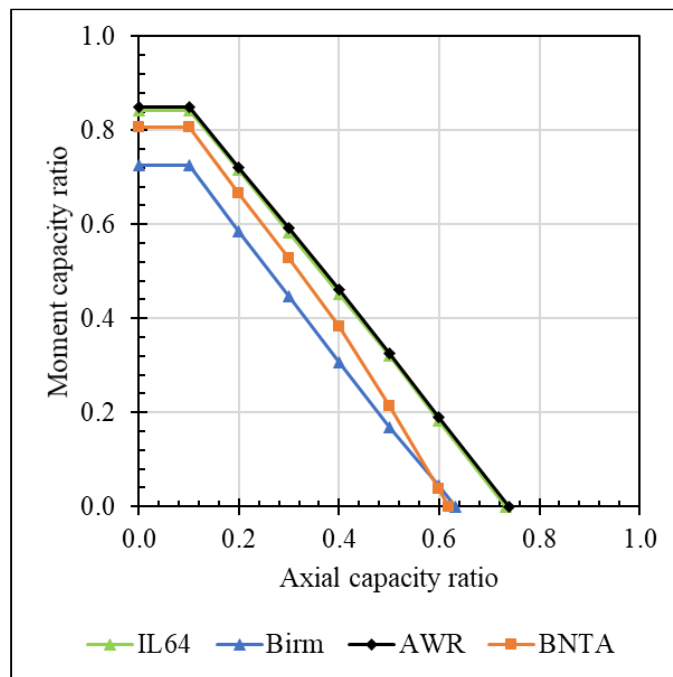
<b>Bridge ID</b>	<b>Bottom plate fractured, horizontal tabs (%)</b>	<b>Bottom plate fractured, vertical tabs (%)</b>	<b>Bottom plate fractured, angles (%)</b>	<b>Side plate fractured, horizontal tabs (%)</b>	<b>Side plate fractured, vertical tabs (%)</b>	<b>Side plate fractured, angles (%)</b>
Birm	12.51	16.96	11.64	37.49	33.04	30.73
Birm-1	9.77	14.54	9.04	40.23	35.46	32.81
Birm-2	14.91	19.07	13.92	35.09	30.93	28.90
AWR	20.37	28.84	17.85	29.63	21.16	18.55
AWR-1	16.81	23.80	15.06	33.19	26.20	23.47
AWR-2	22.25	30.18	19.66	27.75	19.82	17.51
IL64	22.76	28.28	20.75	27.24	21.72	19.81
IL64-1	29.84	36.05	26.92	20.16	13.95	12.59
IL64-2	17.08	22.05	15.71	32.92	27.95	25.71
BNTA	19.51	22.85	18.37	30.49	27.15	25.55
BNTA-1	25.49	29.31	23.79	24.51	20.69	19.31
BNTA-2	27.64	32.05	25.53	22.36	17.95	16.58
BNTA-3	32.09	35.94	29.94	17.91	14.06	13.12





Source: FHWA

**Figure 77. Graph. P-M curve for bottom plate fractured baseline TB geometries with vertical tab connection.**



Source: FHWA

**Figure 78. Graph. P-M curve for bottom plate fractured baseline TB geometries with vertical tab connection.**

For the vertical tab connections, the simplified method estimated the axial capacity under the bottom plate fracture scenario using the same linear relation identified for the horizontal tab configuration

$$C_{Axial}^{BP} = 1 - 2A_{\%Frac} \quad (5.5)$$

However, a slightly higher slope of 1.22 was used to estimate the corresponding flexural capacity.

$$C_{Flex}^{BP} = 1.22C_{Axial}^{BP} \quad (5.6)$$

For the side plate fracture scenario, the axial capacity ratio was expressed as

$$C_{Axial}^{SP} = 1 - 1.2A_{\%Frac} \quad (5.7)$$

and with the flexural capacity subsequently estimated by multiplying this axial ratio by a constant slope of 1.12.

$$C_{Flex}^{SP} = 1.12C_{Axial}^{SP} \quad (5.8)$$

It is important to note that this expression for the side plate fracture scenario directly estimates the flexural capacity under a condition where a bending moment is applied along with a minimum axial stress of 5 ksi, to mitigate the potential for local buckling in the top plate.

The estimated capacities were compared with the FEA results for the bottom plate fracture scenario in Table 29 and for the side plate fracture scenario in Table 30. In both cases, the estimated values showed strong agreement with the FEA results, demonstrating the accuracy and reliability of the proposed simplified method.

**Table 29. Estimation and comparison of P-M interaction curve parameters with the FEA values for a bottom plate fractured TB with vertical tabs at corner connection**

Bridge ID	FEA axial capacity ratio	Est. axial capacity ratio (Eq. 5.5)	Diff. (%)	FEA moment capacity ratio	Est. moment capacity ratio (Eq. 5.6)	Diff. (%)
Birm	0.68	0.66	-2.44	0.82	0.81	-1.91
Birm-1	0.73	0.71	-3.33	0.93	0.87	-7.04
Birm-2	0.63	0.62	-1.79	0.76	0.75	-0.06
AWR	0.44	0.42	-4.19	0.53	0.52	-1.73
AWR-1	0.56	0.52	-6.27	0.71	0.64	-10.47
AWR-2	0.41	0.40	-3.37	0.49	0.48	-0.32
IL64	0.45	0.43	-4.25	0.55	0.53	-4.15
IL64-1	0.29	0.28	-3.77	0.36	0.34	-5.43
IL64-2	0.59	0.56	-5.27	0.77	0.68	-10.91
BNTA	0.57	0.54	-5.57	0.72	0.66	-8.22
BNTA-1	0.43	0.41	-3.32	0.5	0.50	0.57
BNTA-2	0.36	0.36	-1.43	0.42	0.44	3.85
BNTA-3	0.27	0.28	4.18	0.35	0.34	-1.95

**Table 30. Estimation and comparison of P-M interaction curve parameters with the FEA values for a side plate fractured TB with vertical tabs at corner connection**

Bridge ID	FEA axial capacity ratio	Est. axial capacity ratio (Eq. 5.7)	Diff. (%)	FEA moment capacity ratio	Est. moment capacity ratio (Eq. 5.8)	Diff. (%)
Birm	0.63	0.60	-4.70	0.73	0.68	-10.26
Birm-1	0.6	0.57	-4.09	0.68	0.64	-15.77
Birm-2	0.66	0.63	-4.98	0.76	0.70	-9.16
AWR	0.74	0.75	0.82	0.85	0.84	3.64
AWR-1	0.66	0.69	4.16	0.81	0.77	-1.85
AWR-2	0.76	0.76	0.43	0.87	0.85	4.27
IL64	0.73	0.74	0.97	0.84	0.83	-1.44
IL64-1	0.84	0.83	-0.76	0.89	0.93	6.03
IL64-2	0.64	0.66	3.97	0.78	0.74	-7.96
BNTA	0.62	0.67	8.92	0.81	0.76	-2.95
BNTA-1	0.72	0.75	4.76	0.85	0.84	-1.20
BNTA-2	0.76	0.78	2.72	0.87	0.88	1.74
BNTA-3	0.83	0.83	0.46	0.9	0.93	4.87

## 6.5 EVALUATION OF TBS WITH ANGLE CONNECTIONS

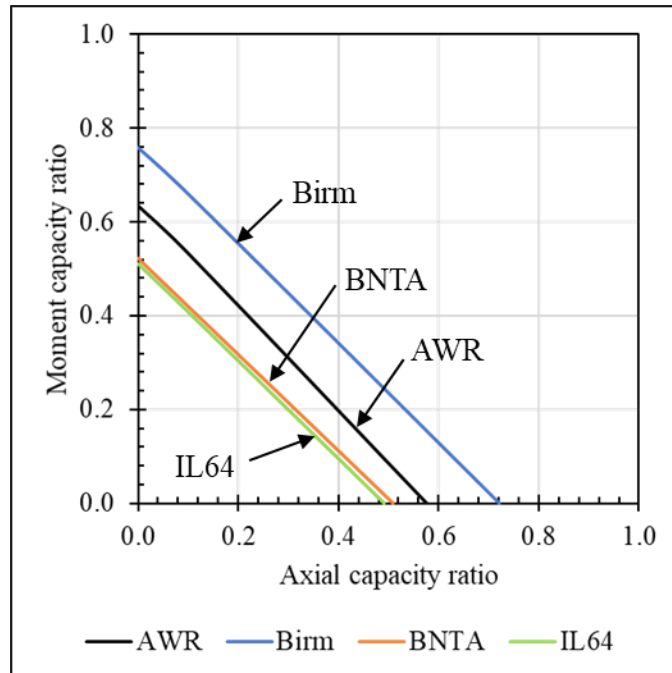
For the angle connections, the same methodology applied to the horizontal and vertical tab configurations was used to develop and analyze the submodels. In this connection type, the angles are bolted to the side, top, and bottom plates without any welding. As a result, under both bottom and side plate fracture scenarios, the angles were not considered fractured in the models. This modeling decision reflects the fact that the load path through the angles remains active regardless of which adjacent plate fractures, since they are mechanically fastened to all three surrounding plates.

Given this detailing, the percentage of cross-sectional areas affected by fracture is generally lower for the angle configuration compared to both horizontal and vertical tab configurations. This is because no additional area from the connector components is lost when a plate fractured. The specific fractured area percentages for each geometry under both fracture scenarios are summarized in Table 28.

All thirteen TB geometries were analyzed using the angle connection configuration, and the results were found to follow similar trends as the other configurations. The P-M interaction curves for the baseline geometries under the bottom plate fracture condition are presented in Figure 79, while those for the side plate fracture condition are shown in Figure 80.

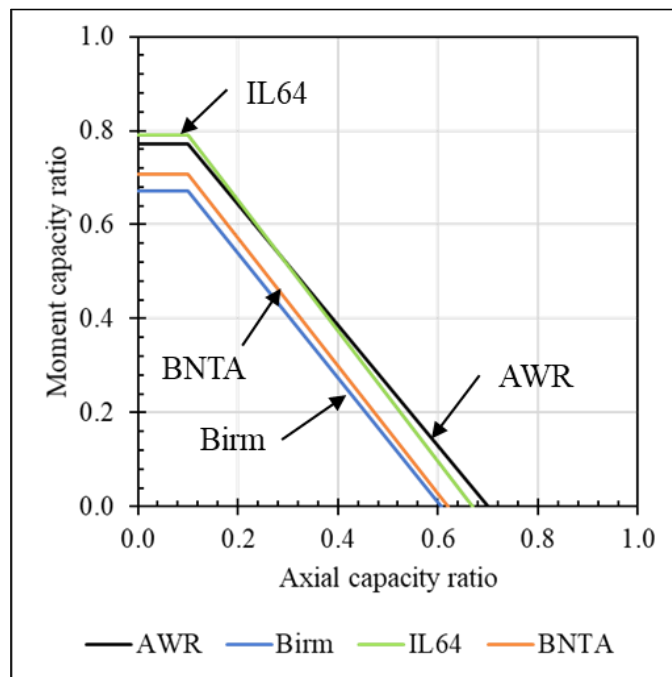
A notable observation under the bottom plate fracture scenario is that the IL64 and BNTA geometries exhibited nearly identical P-M interaction curves. This similarity corresponds to both geometries experiencing comparable percentages of cross-sectional area loss due to fracture. A similar trend was noted under the side plate fracture scenario, where the AWR and IL64 geometries demonstrated consistent behavior, with both configurations experiencing approximately 19% of their cross-sectional area fractured.

These findings, consistent across all three connection configurations, reinforce the conclusion that the remaining capacity of a TB after a fracture is strongly governed by the percentage of the cross-sectional area that is lost. Despite differences in geometric parameters such as depth, flange width, and stiffness, the correlation between fractured area and residual capacity remains dominant. This underscores the importance of fractured area percentage as a principal variable in evaluating the structural performance of faulted TBs.



Source: FHWA

**Figure 79. Graph. P-M curve for bottom plate fractured baseline TB geometries with angle connection.**



Source: FHWA

**Figure 80. Graph. P-M curve for bottom plate fractured baseline TB geometries with angle connection.**

Since angles in this configuration are bolted to both the side and the top and bottom plates, they remain engaged even after a side plate fracture. However, following the fracture, these angles

become critical load-carrying elements. As a result, stress concentration shifts toward the remaining material near the angle connection, causing the localized region to reach the failure strain limit earlier than in other configurations. This earlier onset of failure slightly reduces the overall remaining capacity observed in FEA, as reflected in the following estimation expressions.

Under the bottom plate fracture scenario, the remaining axial capacity was calculated using the expression:

$$C_{Axial}^{BP} = 1 - 2.3A_{\%Frac} \quad (5.9)$$

A constant slope factor of 1.05 was used to estimate the corresponding flexural capacity

$$C_{Flex}^{BP} = 1.05C_{Axial}^{BP} \quad (5.10)$$

In the case of the side plate fracture scenario, the axial capacity was estimated using the relation

$$C_{Axial}^{SP} = 1 - 1.47A_{\%Frac} \quad (5.11)$$

with a slope of 1.10 applied for flexural capacity estimation

$$C_{Flex}^{SP} = 1.10C_{Axial}^{SP} \quad (5.12)$$

It is important to note that the expression used for the side plate fracture scenario directly estimates the flexural capacity under conditions where a bending moment is applied in combination with a minimum axial stress of 5 ksi. This axial tension is intended to mitigate the risk of local buckling in the top plate, which can occur under pure bending in a fractured section.

The estimated capacities for the side plate fracture scenario were compared against the FEA results in Table 31 for the bottom plate fracture condition and in Table 32 for side plate fracture. Overall, the proposed method exhibited good agreement with the detailed simulation results, confirming its applicability and accuracy. However, it is worth mentioning that for angle connections, the estimated capacities were slightly lower compared to other configurations. This reduction can be attributed to the structural behavior of the angles post-fracture.

**Table 31. Estimation and comparison of P-M interaction curve parameters with the FEA values for a bottom plate fractured TB with angle at corner connection**

Bridge ID	FEA axial capacity ratio	Est. axial capacity ratio (Eq. 5.9)	Diff. (%)	FEA moment capacity ratio	Est. moment capacity ratio (Eq. 5.10)	Diff. (%)
Birm	0.72	0.73	1.45	0.76	0.77	1.32
Birm-1	0.8	0.79	-1.18	0.85	0.83	-1.93
Birm-2	0.66	0.68	2.97	0.68	0.71	4.66
AWR	0.58	0.59	2.45	0.63	0.62	-2.34
AWR-1	0.64	0.65	2.51	0.7	0.69	-2.26
AWR-2	0.55	0.55	-0.10	0.59	0.58	-1.78
IL64	0.49	0.52	6.37	0.51	0.55	7.51
IL64-1	0.4	0.38	-4.32	0.42	0.40	-4.18
IL64-2	0.59	0.64	8.41	0.61	0.67	9.72
BNTA	0.51	0.58	13.62	0.52	0.61	16.32
BNTA-1	0.44	0.45	2.96	0.46	0.48	4.08
BNTA-2	0.42	0.41	-0.91	0.43	0.43	0.69
BNTA-3	0.34	0.31	-8.01	0.35	0.33	-7.14

**Table 32. Estimation and comparison of P-M interaction curve parameters with the FEA values for a side plate fractured TB with angle at corner connection**

Bridge ID	FEA axial capacity ratio	Est. axial capacity ratio (Eq. 5.11)	Diff. (%)	FEA moment capacity ratio	Est. moment capacity ratio (Eq. 5.12)	Diff. (%)
Birm	0.61	0.55	-9.65	0.67	0.60	-10.26
Birm-1	0.58	0.52	-11.40	0.68	0.57	-15.77
Birm-2	0.63	0.58	-8.34	0.7	0.63	-9.16
AWR	0.7	0.73	3.66	0.77	0.80	3.64
AWR-1	0.63	0.66	3.20	0.73	0.72	-1.85
AWR-2	0.71	0.74	3.87	0.78	0.82	4.27
IL64	0.67	0.71	5.72	0.79	0.78	-1.44
IL64-1	0.8	0.81	2.32	0.85	0.90	6.03
IL64-2	0.59	0.62	6.31	0.74	0.68	-7.96
BNTA	0.72	0.62	-13.28	0.71	0.69	-2.95
BNTA-1	0.65	0.72	10.22	0.8	0.79	-1.20
BNTA-2	0.71	0.76	6.55	0.82	0.83	1.74
BNTA-3	0.76	0.81	5.71	0.85	0.89	4.87

## 6.6 ACCESS HOLES IN TBS

Openings in TBs are sometimes used for inspection, maintenance, suspender connections, conduit passage, or similar functions. From the standpoint of internal redundancy, discontinuities such as access holes reduce the available cross-sectional capacity and are therefore undesirable. In developing the formulations presented earlier, access holes were not explicitly considered due to the wide range of possible configurations. Therefore, the influence of the presence of access holes was addressed within the proposed evaluation framework to ensure that redundancy is not compromised when such openings are present.

### 6.6.1 Top and bottom plates

In the context of internal redundancy, the role of the top and bottom plates becomes especially critical after a side plate fracture. Under such faulted conditions, the bottom plate, already the primary tension-carrying component of the TB, redistributes additional demands. If an access hole is introduced in the bottom plate, the reduction in effective area directly undermines this redundancy mechanism by limiting the plate's ability to sustain the redistributed loads. Therefore, relatively small unreinforced openings effectively increase the capacity lost in this state, making them particularly detrimental.

The top plate, while generally in compression in the un-faulted state, can experience increased flexural demand and localized tension once a side plate has fractured and the load path is altered. In this redistributed condition, the analysis revealed that the reduction in stiffness or effective area when an access hole is present significantly diminishes the plate's ability to contribute to residual capacity and therefore adversely impacts redundancy.

Because the effects were found to be excessive, it was decided that access holes in either the bottom or top plates are not permitted *unless* the area removed is replaced by splicing with a fully developed solid cover plate or doubler plate that restores the original strength. When reinforcement is provided and an opening is necessary, it should be centered within the plate width to minimize eccentricity and secondary stresses. When such reinforcement is present, the formulations for side plate fracture conditions remain unchanged.

### 6.6.2 Side plates

Side plates are typically relatively deep (compared to the top or bottom plates), and the analysis showed that an access hole at mid-depth is less detrimental to overall behavior in the faulted state because sufficient material remains to carry redistributed loads and maintain section stability. Nevertheless, the access hole in a side plate should still be properly proportioned and detailed to preserve internal redundancy (i.e., it should be of a reasonable size and within the limits of the geometries considered herein). Therefore, limits are imposed on the size of access holes based on the portion of cross-sectional area that remains effective and the need to prevent localized higher stresses. After various trials, reasonable proportions were found that also satisfy the general suggestion found in the AASHTO LRFD BDS regarding the size for access holes. In summary, the maximum height of an access hole should not exceed 20% of the side plate depth, and its length should not exceed 1.5 times its height. Openings should be located at the mid-depth of the side plate where practical. Access holes should not be placed on both side plates at the same



cross section. When access holes are used on each side plate, they should be offset by a minimum of two times the depth of the tie beam. When openings exceed the chosen limits or are positioned outside the suggested location, they should be reinforced with a fully developed solid cover plate or doubler plate to restore capacity and maintain the member's internal redundancy.

For redundancy evaluation, when access holes satisfy the suggestions, the formulations for bottom plate fracture should account for the reduced area in the fractured section properties. In such cases,  $A_{\%Frac}$  is calculated accordingly.

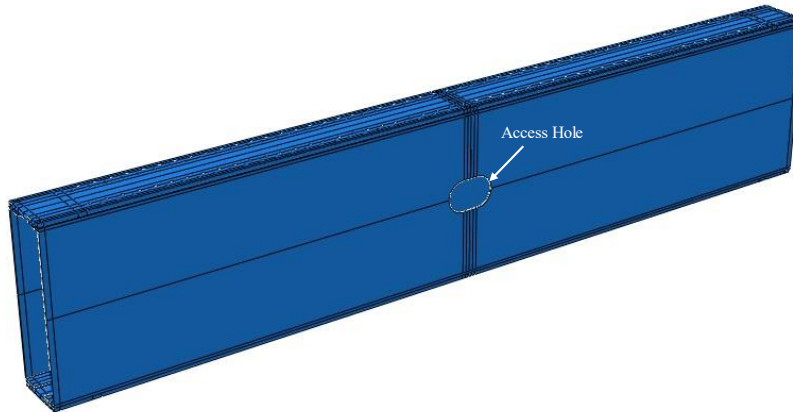
$$A_{\%Frac} = \frac{A_{Frac}}{A_G - 2A_{HH}} \quad (5.14)$$

Where  $A_{HH}$  = The area removed by the hand hole or access hole at the cross section under evaluation (in<sup>2</sup>).

After several trials of developing a method to account for the effect of the access holes, Eq 5.14 was developed. It is important to note that even when an access hole is permitted in a single side plate, it can be seen in Eq. 5.14 that twice its area is considered in the evaluation. This is because the side plate with the reduced effective area (due to the hole) reaches the failure strain sooner than the other, limiting the reserve capacity of the adjacent side plate. This approach ensures that the evaluation accurately reflects the reduced redundancy in accordance with the limiting strain criterion.

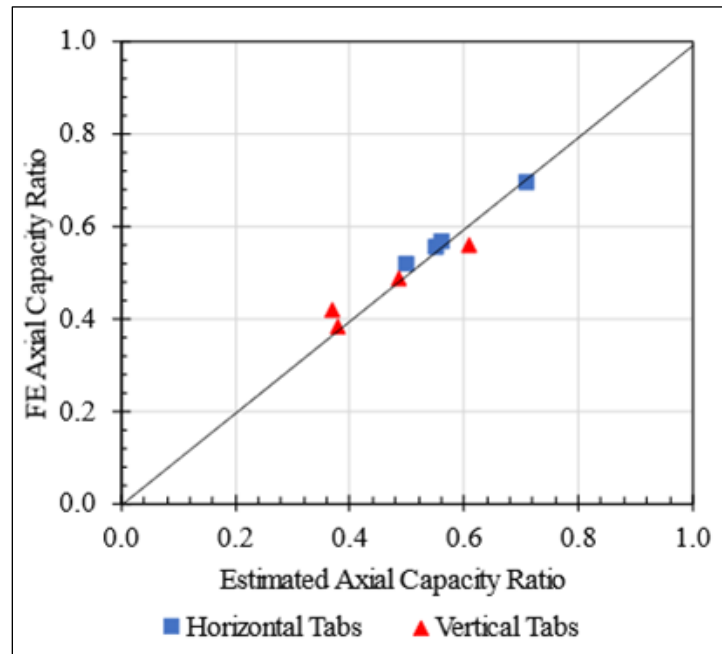
To verify that the proposed approach accurately captures the influence of access holes, the results were compared against FEA models for four baseline tie beam geometries with manhole sized holes, *maximum height equal to 20% of the tie beam depth and length equal to 1.5 times the hole height*, with the suggested criteria to estimate modified  $A_{\%Frac}$  as per Eq. 5.14. For reference, a tie beam with a manhole located in one of its side plates is shown in Figure 81. As described previously, to estimate the remaining capacity of a fractured tie beam, the proposed P-M curve is constructed by using the axial and flexural capacity ratios as anchor points and connecting them with a straight line. Accurate estimation of these anchor points therefore enables reliable prediction of the remaining capacity under combined axial and bending loads. The comparison of axial capacity ratio is presented in Figure 82, while the comparison of flexural capacity ratio is shown in Figure 83.

In these figures, the red triangles represent tie beams with vertical tabs analyzed under the bottom plate fracture condition with the side plate hole, whereas the blue rectangles correspond to tie beams with horizontal tabs. The black diagonal line with unit slope indicates perfect agreement between the estimated and FEA capacities, and its inclusion provides a benchmark to judge accuracy. The close clustering of the data points around this line confirms that the proposed formulations capture the effect of access holes with good accuracy in both axial and flexural capacity predictions. This validation demonstrates that the proposed framework remains applicable and reliable even when access holes are present within the tie beam.



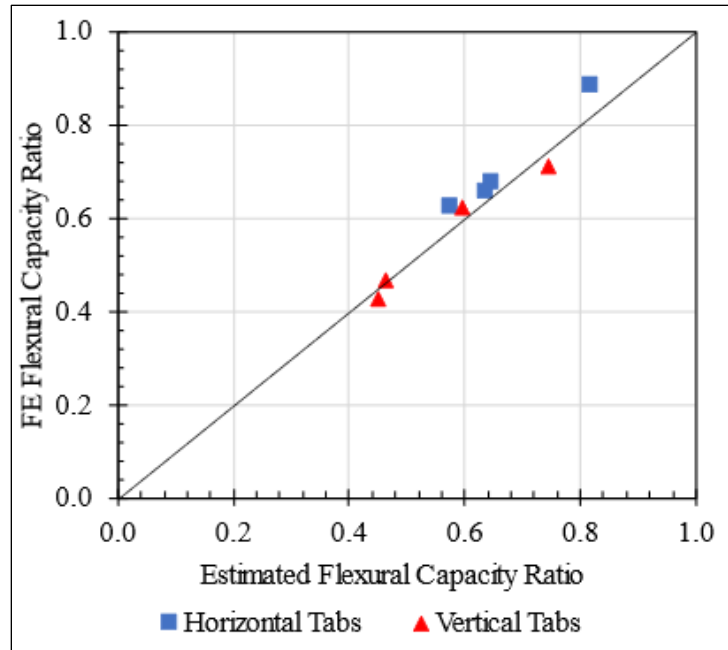
Source: FHWA

**Figure 81. Illustration. Tie beam with a manhole located in one of its side plates sized according to the suggested criteria.**



Source: FHWA

**Figure 82. Graph. Comparison of axial capacity ratio between proposed approach and FEA results for tie beams with access holes.**



Source: FHWA

**Figure 83. Comparison of flexural capacity ratio between proposed approach and FEA results for tie beams with access holes.**

## **7 DEVELOPMENT OF SIMPLIFIED METHODOLOGY FOR FATIGUE ANALYSIS**

The previous chapter focused on remaining strength after fracture, whereas this chapter shifts focus to fatigue behavior, which plays a critical role in determining inspection intervals and ensuring structural reliability.

Given that TBs in these bridges are primarily subjected to a combination of axial tension and bending moments, separate fatigue analyses are conducted for axial and flexural loading conditions. The principle of superposition is then employed to combine the resulting stress ranges from axial tension and bending, enabling the calculation of the final stress range for each connection type and fracture scenario under live load (LL) conditions. Superposition is an acceptable approach since the stress ranges associated with fatigue are very small and result in elastic response even in faulted conditions during the loading and unloading associated with fatigue.

FEA models identical to those utilized in the strength evaluations were developed for each of the thirteen geometries, considering three distinct connection types: horizontal tabs, vertical tabs, and angle connections, and two primary fracture scenarios: bottom and side plate. The geometry, mesh discretization, element type, and interaction properties remained consistent with the previous analyses.

To evaluate the relative fatigue performance of the TB corner configurations under a given fracture condition, a nominal load approach was employed. Instead of applying full fatigue truck loading cases and analyzing a global model for each case (such as Fatigue I or II), a representative load was applied that resulted in a 1.0 ksi stress in the unfaulted condition. This same loading (for both axial and bending separately) was then applied in the faulted condition. Since the analysis is linear elastic, the monotonic loading can also represent the same effect as a stress range, without having to run two separate analyses at the minimum and maximum load with the difference representing the range. The other benefit of normalizing the loading such that the stress is 1.0 ksi in the unfaulted condition, is the stresses in the faulted condition represent the amplification of the stress range directly.

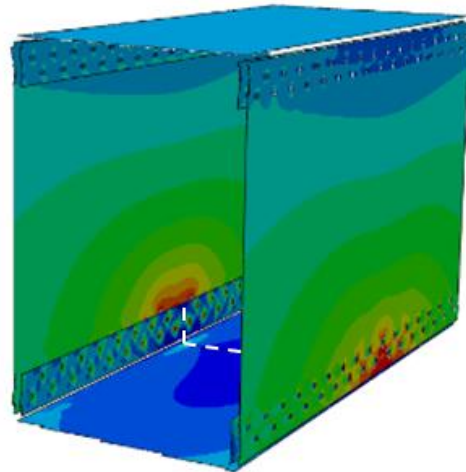
### **7.1 STRESS RESPONSE OF CRITICAL PLATES POST-FRACTURE**

As a given plate becomes non-functional due to fracture, the remaining intact plates are assumed to carry a greater share of the load range, often resulting in localized stress-range amplification. To evaluate fatigue behavior under these conditions, the analysis began identifying the critical plate (i.e., the component that attracts most of the redistributed load and governs fatigue response). The identification of the critical plate depends on both the fracture location (either bottom or side plate) and the connection type used at the corner of the TB. Each connection type (horizontal tab, vertical tab, and angle) responds differently to fracture due to its unique detailing.

For the horizontal tab configurations, where tabs are bolted to the bottom and top plates, and welded to the side plates, the tab plate becomes critical under bottom plate fracture, while the unfractured bottom plate becomes critical under side plate fracture. In vertical tab configurations, with tabs welded to the bottom and top plates and bolted to the side plates, the side plate

becomes critical under BP fracture, whereas the tab plate becomes critical under side fracture. For angle connections, bolted to both bottom and top plates, and side plates with no welds, the angle section remains intact in both fracture scenarios and becomes the critical component by carrying the redistributed load. Following the identification of the critical plate for each fracture scenario, the redistributed stresses in the critical plate were evaluated to understand the resulting fatigue behavior.

For cases where the side or bottom plate serves as the critical component, it was observed that the region of the plate adjacent to the fracture location experiences elevated stress, while the far end of the component along its height or width typically shows minimal change in stress under nominal fatigue loading in the faulted condition. In other words, the stress range is effectively unchanged away from the fracture, which is expected. This behavior is illustrated in the Figure 84 where the dotted white line indicates the fracture location on the bottom plate, and the contour plot shows longitudinal stress distribution, with red representing high stress and blue indicating low stress regions.

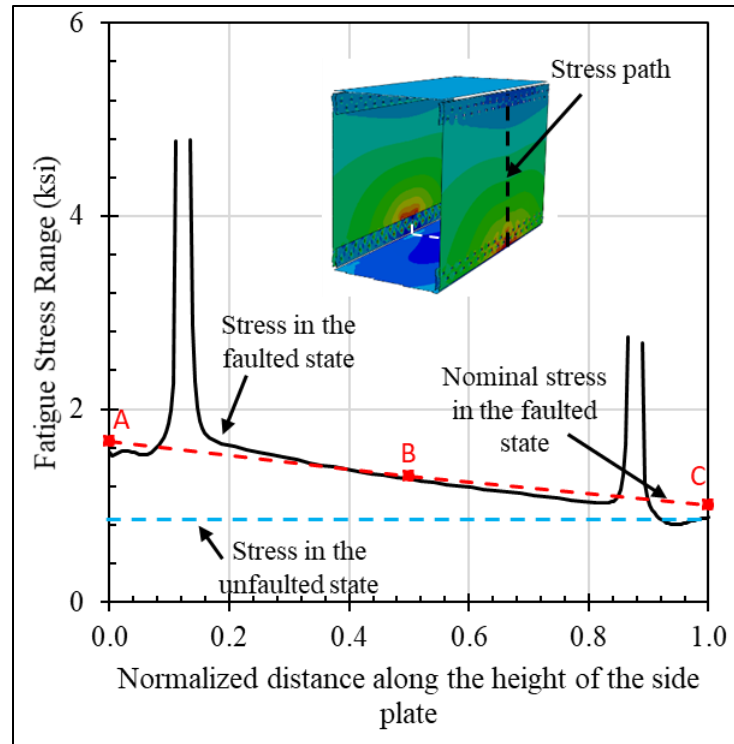


Source: FHWA

**Figure 84. Illustration. Longitudinal stress distribution in the critical plate (side plate) when bottom plate and welded tabs are fractured.**

For the condition shown in the Figure 85, the actual stress along the height of the side plate in the faulted conditions is plotted (solid black line) in Figure 85. Since the applied nominal stress is 1.0 ksi, the solid black line represents the amplification of the stress range in the faulted condition. There are two effects in the solid black line; first there is a linear ramp in the amplification which is highlighted with the dashed red line, and second, there are very sharp gradients at the locations of the holes. The sharp gradients related to the presence of the hole is not of interest as they are approximately 3.0 as expected. Identifying the stress concentration factor (SCF) at a hole is not the point of the analysis, because the fatigue category captures that effect when performing an AASHTO nominal stress fatigue calculation. If the hole is filled with an un-tensioned fastener (e.g. a rivet), then the hole is classified as a category D detail, and that does not change in the faulted or unfaulted state. The true power of the analysis is the amplification of the nominal stress at the hole, which is the red dashed line. For instance, there is a hole at approximately a normalized distance of  $x = 0.16$ , with a unfaulted stress range of 1.0 ksi

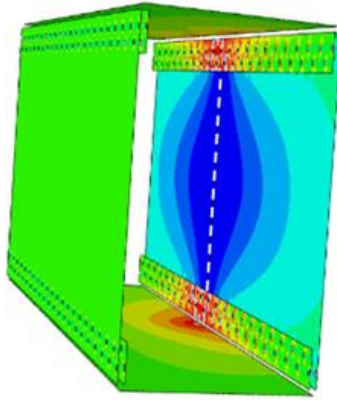
(dashed blue line) and 1.6 ksi stress range (dashed red line) in the faulted condition. In the faulted condition, the nominal stress range at the hole, 1.6 ksi, would be compared to allowable fatigue stress range considering a category D detail. Thus, the goal of the fatigue analyses for various TB scenarios is to capture the effect of the red dashed line (the amplified nominal stress) in the faulted condition and distill it into simple predictive equations.



Source: FHWA

**Figure 85. Graph. Longitudinal stress in the side plate when bottom plate and welded tabs are fractured.**

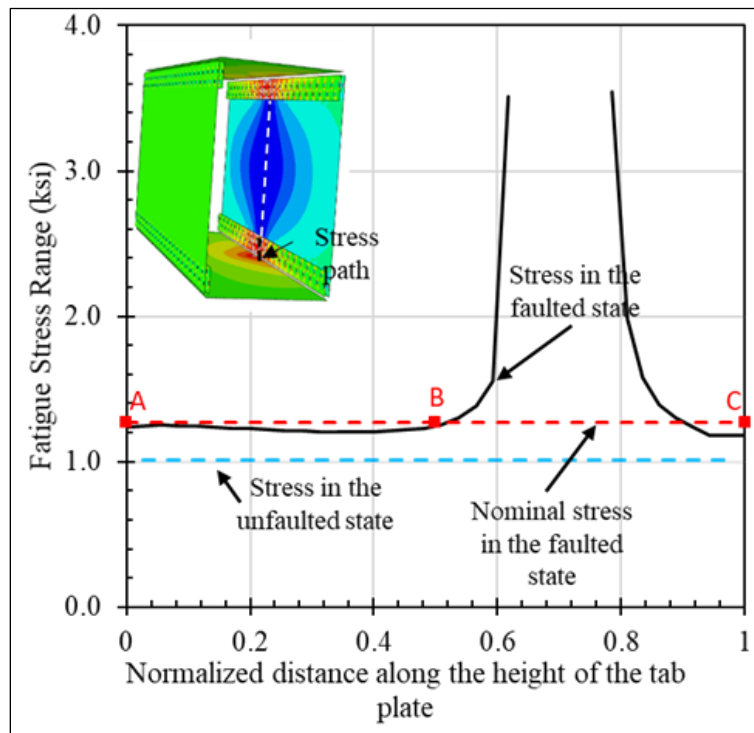
For cases where the tab or angle serves as the critical component, it was observed that elevated nominal stresses extend along the entire length or width of the component and the gradient observed in Figure 85 is not observed. Additionally, the adjacent unfractured plate also experiences elevated stress. This occurs because the smaller connection element, such as the tab or angle, becomes more significant in the post-fracture condition as it begins to resist the forces that were previously carried by the side or bottom plate in the unfaulted state. This behavior is illustrated in the Figure 86 for the vertical tab configuration under the side plate fracture condition. The white dotted line indicates the fracture location on the side plate. In this case, the tabs become the critical components, and the contour plot shows the longitudinal stress distribution, with red indicating high stress and blue indicating low stress. Elevated stress is observed in the bolted tabs as well as in the adjacent top and bottom plates near the fracture.



Source: FHWA

**Figure 86. Illustration. Longitudinal stress distribution in the tab plate when side plate is fractured.**

For such a situation, Figure 87 shows the stress profile along the height of the critical tab. The black line represents the stress distribution, with noticeable sharp gradients at the bolt hole locations. However, in this scenario, the nominal stress amplification (red dashed line) is uniformly amplified, in lieu of the linear gradient seen in Figure 85. By estimating the nominal stress range in the region marked by the red line, the corresponding fatigue stress range can be used to determine a suitable inspection interval again using the familiar AASHTO nominal stress range approach.



Source: FHWA

**Figure 87. Graph. Longitudinal stress in the tab plate when side plate is fractured.**

Based on these observations, three key locations were identified along the length of the critical plate to capture the stress variation in the faulted condition:

- Point A: The near end of the critical plate (at  $x = 0$ ).
- Point B: The mid-length of the critical plate (at  $x = 0.5$ ).
- Point C: the location on the critical plate at the far end connected to the fractured component (at  $x = 1.0$ ).

In some cases, such as shown in Figure 85, the stresses at points A, B, and C are clearly different. However, in other cases, such as shown in Figure 87, stress is effectively constant, and the values of A, B, and C are the same. After evaluating all 13 geometries and all different fracture scenarios (side plate, bottom plate, and the 3 different corner connections), trends in how the nominal longitudinal stress range is distributed across the critical plate were observed. Evaluation of the local stresses at the edge of the hole confirmed the stress concentration factors in the critical plate were still on the order of 2.8 to 3.0 at the edge of the hole. Thus, the use of the nominal stress range approach (albeit in conjunction with adjustment factors to be discussed below) was found to be valid.

To estimate the nominal fatigue stress shown by the red lines in the plots for all the geometries, corner connections, and fracture scenarios analyzed, simplified formulations were developed to calculate the nominal stress range at these key locations in the faulted state. As expected for some details the values are constant whereas for others, adjustments due to the gradient in nominal stress are accounted for. Nevertheless, the nominal stress range is of primary interest, as it allows the continued use of established fatigue categories and allows practicing engineers to apply simplified fatigue life in the faulted state, which is suggested by the IRM Guide Spec. (6) in order to set the in-service special inspection interval.

## 7.2 STRESS ESTIMATION IN CRITICAL PLATE UNDER FATIGUE LOADING

As stated, to evaluate the fatigue response of TBs in the faulted state, a simplified and scalable method was developed to estimate the stress range in the critical plate. The estimates were generated for all connection types (horizontal tabs, vertical tabs, and angles), under both bottom and side plate fracture scenarios, and considering separate cases for axial and bending. The resulting correlations are summarized in the Table 33.

The core of the estimation approach lies in scaling expressions derived from regression analysis of FE data. These expressions are grounded in the basic mechanics principle:

$$\text{Stress} = \frac{\text{Force}}{\text{Area}} \quad (6.1)$$

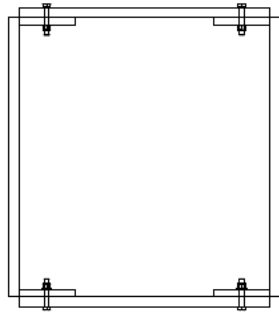
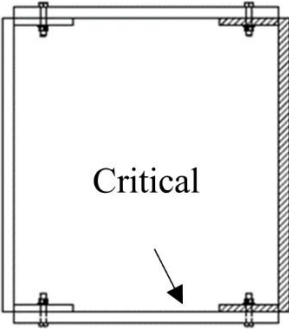
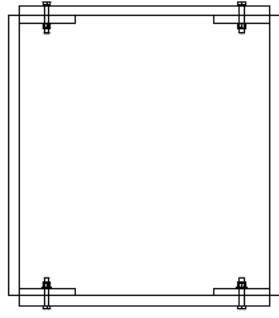
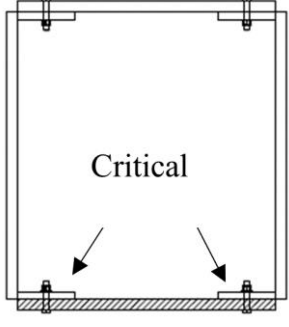
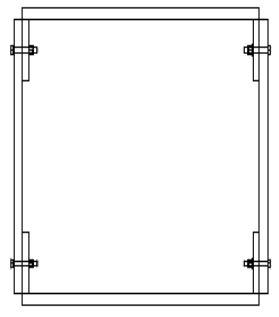
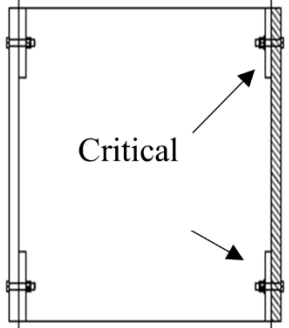
When a given plate fractures, the load range, whether due to axial or flexural stress, that was previously carried by the failed component is redistributed to the remaining intact plates. As a result, the stress range in these unfractured plates increases. The increase in stress range was first captured with a scaling parameter ( $\alpha$ ), represented as a ratio of the area of the fractured plate (representing the lost resistance) to the area of the critical plate (representing the component now absorbing the additional force). Scaling factors were also developed for both axial and bending loading as needed. It was found that such simple formulations capture the rise in stress range

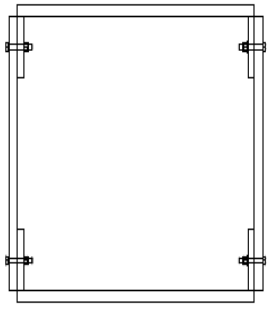
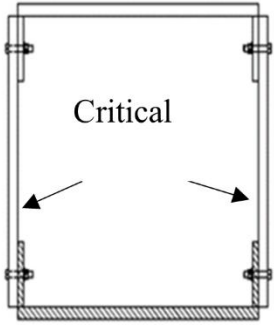
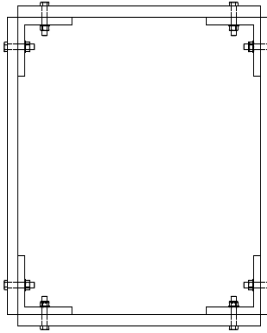
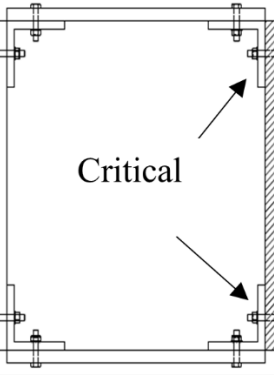
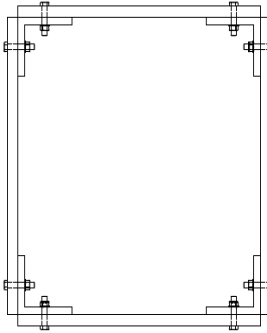
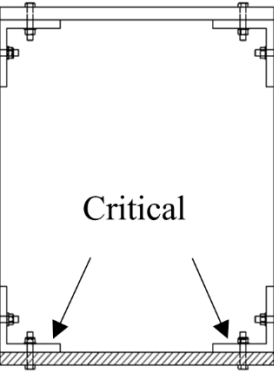


due to the transfer of force to the smaller remaining area. The scaling parameter captures the uniform amplification of the nominal stress range.

For the cases where side or bottom plate serve as critical component, another amplification parameter ( $\beta$ ), was needed to account for the linear ramp of the nominal stress ranges as was seen in the red dashed line in Figure 87. This factor provides a means to capture the localized increase in stress near the interface between the fractured and critical components, where geometric discontinuities cause peak stress.

**Table 33. Proposed equations to estimate the stress range in the critical plate under fatigue loading**

Case	Corner Configuration	Fracture Condition	Parameters
1a	 <p>Horizontal Tabs</p>	 <p>Side Plate Fracture Condition</p>	<p>Critical Component: Bottom Plate</p> $\alpha_{Axial} = \frac{0.5A_{SP} + A_{TP}}{A_{BP} + 0.19A_{TP}}$ $\alpha_{Flex} = \frac{0.5A_{SP} + A_{TP}}{A_{BP} + 0.19A_{TP}}$ $\beta_{Axial} = 2.5$ $\beta_{Flex} = 2.2$
1b	 <p>Horizontal Tabs</p>	 <p>Bottom Plate Fracture Condition</p>	<p>Critical Component: Tab</p> $\alpha_{Axial} = \frac{A_{BP}}{2A_{TP} + 0.22A_{SP}}$ $\alpha_{Flex} = \frac{A_{BP}}{2A_{TP} + 0.22A_{SP}}$ $\beta_{Axial} = 1.0$ $\beta_{Flex} = 1.0$
2a	 <p>Vertical Tabs</p>	 <p>Side Plate Fracture Condition</p>	<p>Critical Component: Tab</p> $\alpha_{Axial} = \frac{0.5A_{SP}}{A_{TP} + 0.63\sqrt{\frac{A_{TP}}{A_{BP}}}A_{BP}}$ $\alpha_{Flex} = \frac{0.17A_{SP}}{A_{TP} + 0.73\sqrt{\frac{A_{TP}}{A_{BP}}}A_{BP}}$ $\beta_{Axial} = 1.0$ $\beta_{Flex} = 1.0$

Case	Corner Configuration	Fracture Condition	Parameters
2b	 <p>Vertical Tabs</p>	 <p>Bottom Plate Fracture Condition</p>	<p>Critical Component: Side Plate</p> $\alpha_{Axial} = \frac{A_{BP} + 2A_{TP}}{1.62A_{SP}}$ $\alpha_{Flex} = \frac{A_{BP} + 2A_{TP}}{1.62A_{SP}}$ $\beta_{Axial} = 4.0$ $\beta_{Flex} = 4.0$
3a	 <p>Angles</p>	 <p>Side Plate Fracture Condition</p>	<p>Critical Component: Angle</p> $\alpha_{Axial} = \frac{0.5A_{SP}}{A_{An} + 0.35\sqrt{\frac{A_{An}}{A_{BP}}}A_{BP}}$ $\alpha_{Flex} = \frac{0.17A_{SP}}{A_{An} + 0.31\sqrt{\frac{A_{An}}{A_{BP}}}A_{BP}}$ $\beta_{Axial} = 1.2$ $\beta_{Flex} = 1.0$
3b	 <p>Angles</p>	 <p>Bottom Plate Fracture Condition</p>	<p>Critical Component: Angle</p> $\alpha_{Axial} = \frac{A_{BP}}{2A_{An} + 0.12A_{SP}}$ $\alpha_{Flex} = \frac{A_{BP}}{2A_{An} + 0.12A_{SP}}$ $\beta_{Axial} = 1.2$ $\beta_{Flex} = 1.2$

where:

$A_{BP}$  = Net area of bottom plate of a tie beam (inch<sup>2</sup>)

$A_{SP}$  = Net area of side plate of a tie beam (inch<sup>2</sup>)

$A_{An}$  = Net area of an angle used in the corner connection of a tie beam (inch<sup>2</sup>)

$A_{TP}$  = Net area of a tab plate used in the corner connection of a tie beam (inch<sup>2</sup>)

### **7.3 PROCEDURE TO ESTIMATE STRESS RANGE IN THE CRITICAL PLATE UNDER FRACTURE**

The following section outlines how to use Table 33 to estimate the stress range in the critical plate under a given fracture scenario. The procedure begins by identifying the connection type (horizontal tab, vertical tab, or angle) and the loading condition (axial force and/or bending moment).

Using the parameters provided in Table 33, the stress ranges due to axial and bending loads are calculated independently and then superimposed to determine the total stress range in the critical plate. Based on the identified connection and fracture type (either bottom plate or outer plate), the critical plate is determined using the methodology outlined in earlier sections.

If the bottom or side plate is identified as the critical component, the stress distribution along its length is evaluated through the following three-step process outlined below. Again, it is noted that in some cases, the factors  $\alpha$  and  $\beta$  presented below account for gradients in the stress, even for the cases where the gradient is constant (i.e., as shown in Figure 87).

Step 1: Point C represents the end of the critical plate connected to the unfractured component. As this region is not directly influenced by the fracture, it is assumed to experience no additional stress due to fracture. The stress at this location ( $S_C$ ) is thus estimated as below:

$$S_C = \Delta FS \quad (6.2)$$

Where,  $\Delta FS$  = nominal factored fatigue stress range in the given TB cross section in the unfaulted condition (ksi)

Step 2: At Point B, located at the mid-length of the critical plate, the nominal stress range is computed based on the redistributed force. This represents the average stress level the plate carries after fracture, and can be estimated as:

$$S_B = \Delta FS (1 + \alpha) \quad (6.3)$$

Step 3: Point A lies at the end of the critical plate adjacent to the fractured component, where abrupt changes in stiffness and force flow lead to localized stress amplification. To capture these effects, the factors ( $\alpha$  and  $\beta$ ) from Table 33 are applied to nominal stress to estimate the peak stress at this location. The peak stress at this edge represented as  $S_A$  is calculated using the scaling parameter and amplification factor:

$$S_A = \Delta FS (1 + \alpha \beta) \quad (6.4)$$

However, in scenarios where tab plates or angle sections act as the critical component (e.g., horizontal tab or angle connections under bottom plate fractured scenario), the behavior differs. In these cases, the entire component experiences elevated stress, and can be estimated as  $\Delta FS (1 + \alpha \beta)$ .

Under the fracture scenario where tabs act as the critical component, the redistributed stress in the tabs remains nearly uniform along their length. In contrast, when angles are the critical component, the stress in the leg bolted to the unfractured plate is estimated using the scaling parameter. The leg connected to the fractured plate experiences a stress approximately  $1.2\beta$  times higher. The developed approach to estimating stress distribution along the critical plate enhances the accuracy of fatigue assessment. By incorporating geometry-dependent scaling parameters and amplification factors, the methodology captures the localized effects of load redistribution following fracture. Together, these formulations provide a practical and transparent framework for evaluating the fatigue performance of fractured TBs in tied arch bridges.

The following example uses the geometry of the IL64 bridge with horizontal tabs to demonstrate the application of the approach. The plate sizes for the IL64 are given in Table 20. In this example, it is assumed a side plate is fractured with an initial axial fatigue stress range ( $\Delta FS$ ) of 2.0 ksi.

The corresponding  $\alpha$  and  $\beta$  factors are taken from Table 33 and applied to compute the redistributed stress values at key points on the critical plate. The calculations and results are presented as follows:

- The critical plate is bottom plate. Using the table above:
- Calculate the scaling parameter:  $\alpha = \frac{0.5A_{SP} + A_{TP}}{A_{BP} + 0.19A_{TP}} = \frac{0.5(63) + 8}{(66) + 0.19(8)} = 0.585$
- Determine the amplification factor:  $\beta = 2.5$
- $S_A = \Delta FS = 2.0$  ksi
- $S_B = \Delta FS (1 + \alpha) = 2.0 \text{ ksi} + (0.585 \times 2.0 \text{ ksi}) = 3.17$  ksi
- $S_C = \Delta FS (1 + \alpha \beta) = 2.0 + (2.5 \times 0.585 \times 2 \text{ ksi}) = 4.93$  ksi

Similar calculations for flexural loading are carried out using the corresponding expressions provided in Table 33. The resulting stress ranges from both axial and bending loads are then combined to obtain the total stress range in the critical plate for the faulted condition.

This refined understanding of stress distribution along the critical plate enables a more accurate assessment of fatigue performance, particularly when combined with geometry-based scaling and amplification parameters. In practice, the stress at the junction of the critical plate and the fractured component is the primary point of concern, as it governs the fatigue stress range in the faulted state and ultimately dictates the calculation of inspection intervals. This stress range can be estimated by summing the fatigue stress range due to axial and flexural components of the LL:

$$\Delta FFS_{Total} = \Delta FFS_{Axial} + \Delta FFS_{Flex} \quad (6.5)$$

where:

$$\Delta FFS_{Axial} = \Delta FS_{Axial}(1 + \alpha_{Axial} \cdot \beta_{Axial}) \quad (6.6)$$

$$\Delta FFS_{Flex} = \Delta FS_{Flex}(1 + \alpha_{Flex} \cdot \beta_{Flex}) \quad (6.7)$$

$\Delta FFS_{Total}$  = total nominal factored fatigue stress range in the critical component of the fractured TB (ksi)

$\Delta FFS_{Axial}$  = nominal factored axial fatigue stress range in the critical component of the fractured TB due to the fatigue design LL

$\Delta FFS_{Flex}$  = nominal factored flexural fatigue stress range in the critical component of the fractured TB due to the fatigue design LL

$\Delta FS_{Axial}$  = nominal factored axial fatigue stress range in the given TB cross section in the unfaulted condition (ksi)

$\Delta FS_{Flex}$  = nominal factored flexural fatigue stress range in the given TB cross section in the unfaulted condition (ksi)

$\alpha_{Axial}$  = scaling parameter for calculating the nominal factored axial fatigue stress range in a fractured TB determined from Table 33

$\beta_{Axial}$  = amplification factor for calculating the nominal factored axial fatigue stress range in a fractured TB determined from Table 33

$\alpha_{Flex}$  = scaling parameter for calculating the nominal factored flexural fatigue stress range in a fractured tie beam determined from Table 33

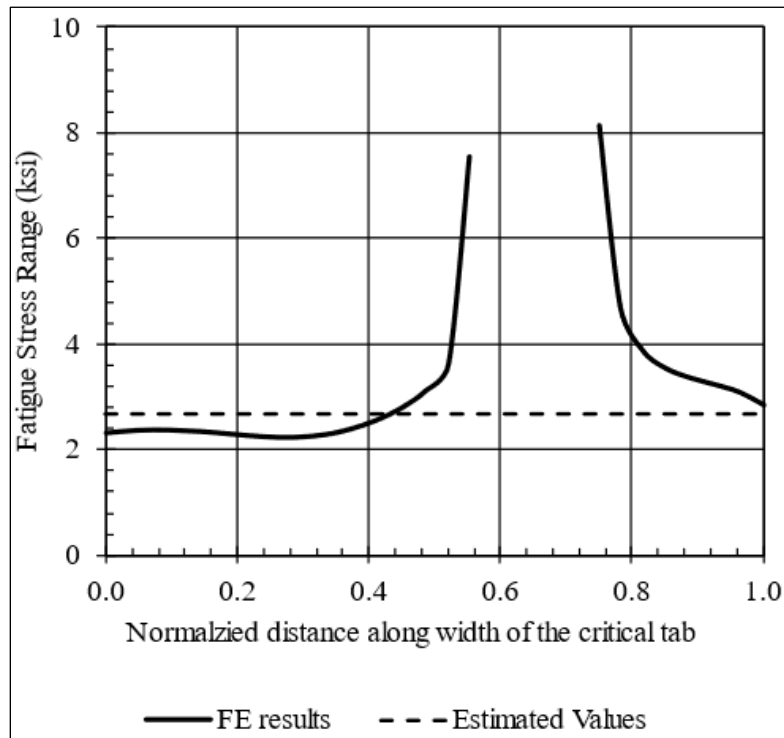
$\beta_{Flex}$  = amplification factor for calculating the nominal factored flexural fatigue stress range in a fractured TB determined from Table 33

#### 7.4 FATIGUE FORMULATION FOR TBS WITH ACCESS HOLES IN SIDE PLATES

As discussed in the strength formulations (Sec. 6.6), access holes are not permitted in the top or bottom plates, and therefore the side plate fracture formulations remain unchanged. In contrast, when a tie beam with an access hole of area  $A_{HH}$  in one of its side plates is subjected to the bottom plate fracture condition, the fatigue stress range estimation should account for the corresponding reduction in effective area. Under the bottom plate fracture condition, the side plates carry the redistributed load after the loss of resistance from the fractured bottom plate, and accordingly, it may be the way to address the change in load redistribution was to modify the parameters  $\alpha$  and  $\beta$ . Using the four basic geometries used in the strength evaluation for handholes discussed above, it was subsequently found that only the calculation of  $\alpha$  needed to be revised for the fatigue stress range estimation. More specifically, the equation used to calculate  $\alpha$  could be modified to account for the effect of the access holes. The updated equation is shown in Table 34 for the various applicable cases (*Note the addition of the term  $A_{HH}$  in the equation, which accounts for the access hole. When there is no handhole, the term is zero and the*

*equation results in the same value for alpha as when there was no handhole as originally developed.)*

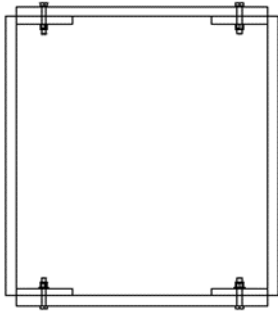
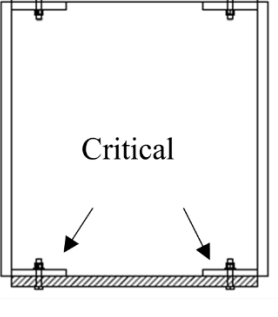
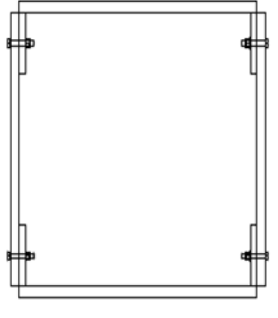
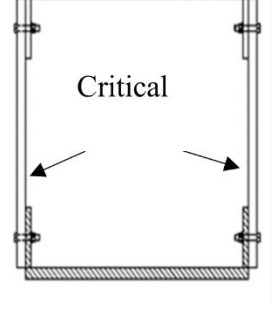
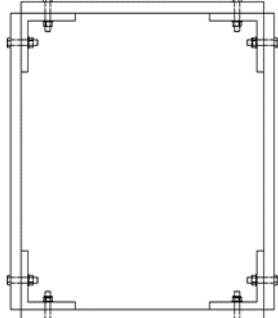
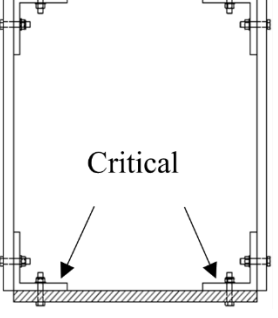
The revised equation was found to result in very good estimates of the nominal stress range at the holes in the critical component. For example, for the AWR tie beam with a horizontal tab and an access hole in the side plate, the stress range in the critical plate (tab) was evaluated under a 1 ksi axial stress and a bottom plate fracture condition using Abaqus. The resulting stress values from the FE are plotted in Figure 88 as a solid black line, where the empty slot indicates the location of the hole in the tab. These FEA results are compared against the estimated values plotted as a dotted line, which represent the nominal stresses and do not account for stress amplification or concentration near the hole. The estimation was carried out using the correlations presented in Table 34 and the equations outlined in the previous section. The comparison of the two stress plots shows good agreement, validating the effectiveness of the proposed approach in accurately predicting the stress range in the critical plate. These findings demonstrate the applicability of the method for fatigue assessment of tie beams with side plate access holes under bottom plate fracture conditions.



Source: FHWA

**Figure 88. Graph. Fatigue stress range in the critical plate (tab) of the AWR tie beam with a side plate access hole under 1 ksi axial stress and bottom plate fracture.**

**Table 34. Proposed equations to estimate the stress range in the critical plate under fatigue loading**

Case	Corner Configuration	Fracture Condition	Parameters
1b	 <p>Horizontal Tabs</p>	 <p>Bottom Plate Fracture Condition</p>	<p>Critical Component: Tab</p> $\alpha_{Axial} = \frac{A_{BP}}{2A_{TP} + 0.22(A_{SP} - A_{HH})}$ $\alpha_{Flex} = \frac{A_{BP}}{2A_{TP} + 0.22(A_{SP} - A_{HH})}$ $\beta_{Axial} = 1.0$ $\beta_{Flex} = 1.0$
2b	 <p>Vertical Tabs</p>	 <p>Bottom Plate Fracture Condition</p>	<p>Critical Component: Side Plate</p> $\alpha_{Axial} = \frac{A_{BP} + 2A_{TP}}{1.62(A_{SP} - A_{HH})}$ $\alpha_{Flex} = \frac{A_{BP} + 2A_{TP}}{1.62(A_{SP} - A_{HH})}$ $\beta_{Axial} = 4.0$ $\beta_{Flex} = 4.0$
3b	 <p>Angles</p>	 <p>Bottom Plate Fracture Condition</p>	<p>Critical Component: Angle</p> $\alpha_{Axial} = \frac{A_{BP}}{2A_{An} + 0.12(A_{SP} - A_{HH})}$ $\alpha_{Flex} = \frac{A_{BP}}{2A_{An} + (A_{SP} - A_{HH})}$ $\beta_{Axial} = 1.2$ $\beta_{Flex} = 1.2$



## 8 VALIDATION OF PROPOSED SIMPLIFIED METHODOLOGY

In this chapter, the accuracy and applicability of the proposed simplified methodology are validated using two additional TB geometries from the LaCrosse and Atchison bridges. These geometries were not part of the original dataset used to develop the formulation, making them suitable for independent evaluation. The validation study includes both strength and fatigue assessments under bottom plate and side plate fracture conditions and covers all three corner connection types: horizontal tab, vertical tab, and angle connections.

For each geometry, submodels were analyzed using all three corner connection types: horizontal tab, vertical tab, and angle connections. The configurations incorporating tab-type connections are summarized in Table 35, while the corresponding angle connection configurations are provided in Table 36. Results from the simplified equations were directly compared with those from detailed finite element analyses to determine whether the proposed methodology reliably predicts remaining capacity and stress response in configurations not originally used in its development. The following sections present these results, along with comparisons, trends, and discussion of any observed deviations.

**Table 35. TB geometries with tab-type corner connections used in the validation study**

Bridge ID	Bottom/ top plate width (inch)	Bottom/ top plate thickness (inch)	Bottom/ top plate area (inch <sup>2</sup> )	Side plate height (inch)	Side plate thickness (inch)	Side plate area (inch <sup>2</sup> )	Tab plate
La Crosse	30.000	1.500	45.000	65.500	0.750	49.125	1"x8"
Atchison	48.000	1.125	54.000	70.000	0.750	52.500	1"x8"

**Table 36. TB geometries with angle-type corner connections used in the validation study**

Bridge ID	Bottom/ top plate width (inch)	Bottom/ top plate thickness (inch)	Bottom/ top plate area (inch <sup>2</sup> )	Side plate height (inch)	Side plate thickness (inch)	Side plate area (inch <sup>2</sup> )	Angle
La Crosse	30.000	1.500	45.000	65.500	0.750	49.125	L8x8x1
Atchison	48.000	1.125	54.000	70.000	0.750	52.500	L8x8x1

## 8.1 ASSESSMENT OF PROPOSED FORMULATION FOR HORIZONTAL TAB-BASED TBS

Both TB geometries were first modeled with horizontal tab-type connections (Table 35) and analyzed under bottom plate and side plate fracture conditions. For the bottom plate fracture scenario, the P-M curve parameters were estimated using Equation 5.1 for axial capacity ratio ( $C_{Axial}^{BP}$ ) and Equation 5.2 for flexural capacity ratio ( $C_{Flex}^{BP}$ ). The detailed calculations for the LaCrosse geometry are presented below.

In the case of the LaCrosse River bridge (Table 35), the bottom plate area is 45.00 in<sup>2</sup>, and the gross area is 220.25 in<sup>2</sup>. The pure axial point ( $C_{Axial}^{BP}$ ) is estimated as follows:

$$A_{\%Frac} = \frac{30 * 1.5}{2 * ((30 * 1.5) + (65.5 * 0.75) + 8 + 8)} = \frac{45}{220.25} = 0.20$$

$$C_{Axial}^{BP} = 1 - 2.0A_{\%Frac} = 1 - 2(0.20) = 0.59$$

The pure flexure point ( $C_{Flex}^{BP}$ ) is estimated as follows:

$$C_{Flex}^{BP} = 1.15 C_{Axial}^{BP} = 0.68$$

Similarly, for the case of side plate fracture, the P-M curve was estimated using Equations 5.3 and 5.4. The calculations for the LaCrosse geometry are presented below.

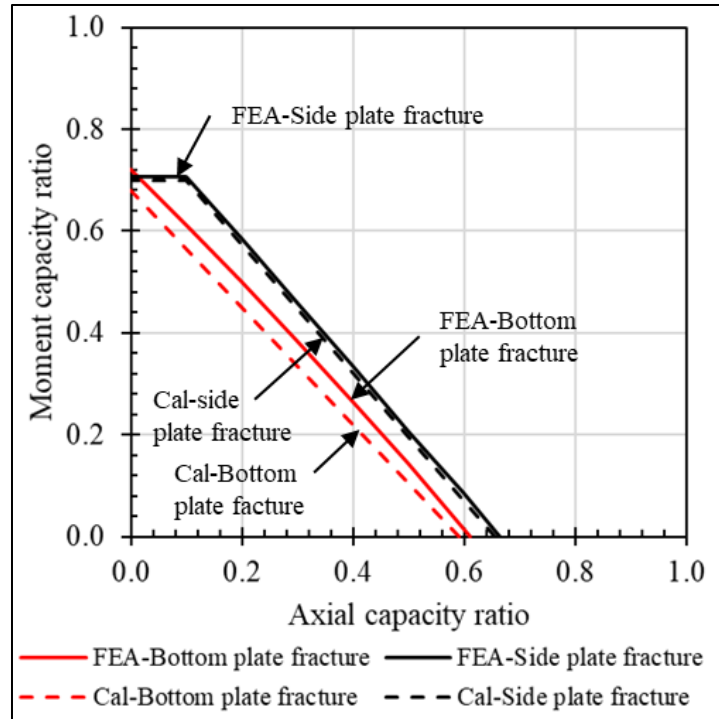
Since the tabs are welded to the side plate, a side plate fracture also results in the fracture of the two attached tabs. Therefore, these tabs are considered fractured in the analysis.

$$A_{\%Frac} = \frac{(65.5 * 0.75) + (2 * 8)}{2 * ((30 * 1.5) + (65.5 * 0.75) + 8 + 8)} = \frac{65.125}{220.25} = 0.30$$

$$C_{Axial}^{SP} = 1 - 1.2A_{\%Frac} = 1 - 1.2(0.22) = 0.73$$

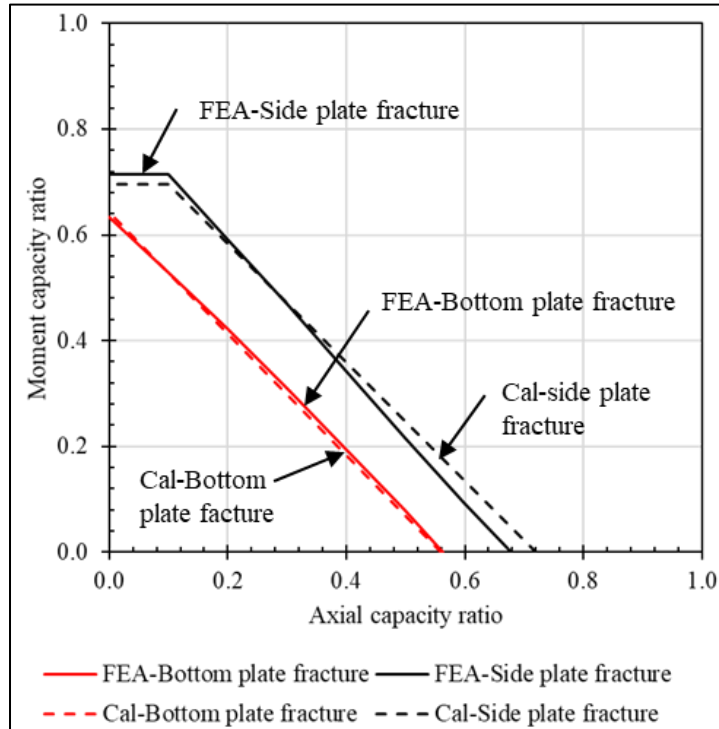
$$C_{Flex}^{SP} = 1.12 C_{Axial}^{SP} = 1.12(0.73) = 0.82$$

The P-M curves generated using the estimated values for the LaCrosse TB are plotted alongside the corresponding FEA results in Figure 89. Figure 90 presents a similar comparison for Atchison Bridge. In both plots, red lines represent the P-M curves for the bottom plate fracture condition, while black lines indicate the side plate fracture condition. Dashed lines correspond to the simplified method estimates, and solid lines show the results obtained from FEA. The close alignment between the estimated and FEA curves in both cases confirms the accuracy and reliability of the proposed simplified approach.



Source: FHWA

**Figure 89. Graph. P-M curve comparison between simplified method and FEA for LaCrosse TB when bottom plate is fractured.**



Source: FHWA

**Figure 90. Graph. P-M curve comparison between simplified method and FEA for Atchison TB when bottom plate is fractured.**

After evaluating the remaining strength, the next step was to estimate the fatigue stress ranges. As described in the previous chapter, to estimate the fatigue stress ranges the submodels were subjected to fatigue axial and bending loads separately. For each fracture scenario and corner connection type, the corresponding critical plate was identified. Stress distributions along the length of this critical plate were then calculated under both loading conditions. These individual stress ranges were then combined using superposition to determine the total fatigue stress range in the faulted condition.

For the bottom plate fracture with horizontal tab connections, the tab plates served as the critical components. In contrast, for the side plate fractured condition, the bottom plate acted as the critical plate. To estimate the post-fracture stress ranges in these components, the faulted TB submodels were subjected to unit axial and unit bending loads of ( $\Delta FS =$ ) 1 ksi each in separate analyses. The calculations for LaCrosse TB are shown below.

$$\Delta FS_{Axial} = 1 \text{ ksi}$$

$$\Delta FS_{Flex} = 1 \text{ ksi}$$

For bottom plate fracture, following the Table 33 the critical plate is tabs and scaling parameter is calculated for this case as:

$$\text{Scaling parameter } (\alpha_{axial} = \alpha_{flex}) = \frac{A_{BP}}{2A_{TP} + 0.22A_{SP}} = \frac{\left(\frac{45}{220.25}\right)}{2\left(\frac{8}{220.25}\right) + \left(\frac{49.125}{220.25}\right)} = 1.68$$

$$\text{Amplification factor } (\beta_{axial} = \beta_{flex}) = 1$$

As the critical plate is tab, it will experience a uniform stress calculated as:

$$\Delta FFS_{Axial} = \Delta FS_{Axial}(1 + \alpha_{Axial} \cdot \beta_{Axial}) = 1 (1 + 1.68) = 2.68 \text{ ksi}$$

$$\Delta FFS_{Flex} = \Delta FS_{Flex}(1 + \alpha_{Flex} \cdot \beta_{Flex}) = 1 (1 + 1.68) = 2.68 \text{ ksi}$$

$$\Delta FFS_{Total} = \Delta FFS_{Axial} + \Delta FFS_{Flex} = 2.68 + 2.68 = 5.36 \text{ ksi}$$

It is important to note that for the bottom plate fracture condition, the stress range in the critical plate did not change with the type of applied load.

For side plate fracture, following the Table 33 the critical plate is bottom plate and scaling parameter for axial load is calculated for this case as:

$$\text{Scaling parameter } (\alpha_{axial}) = \frac{0.5A_{SP} + A_{TP}}{1A_{BP} + 0.19A_{TP}} = \frac{0.5\left(\frac{49.125}{220.25}\right) + \left(\frac{8}{220.25}\right)}{\left(\frac{45}{220.25}\right) + 0.19\left(\frac{8}{220.25}\right)} = 0.69$$

$$\text{Amplification factor } (\beta_{axial}) = 2.5$$

$$\Delta FFS_{Axial} = \Delta FS_{Axial}(1 + \alpha_{Axial} \cdot \beta_{Axial}) = 1 (1 + (2.5 \times 0.69)) = 2.73 \text{ ksi}$$

$$\Delta FFS_{Total} = \Delta FFS_{Axial} + \Delta FFS_{Flex} = 2.68 + 2.68 = 5.36 \text{ ksi}$$

Similarly, for flexural fatigue load the calculations are as follows:

$$\text{Scaling parameter } (\alpha_{flex}) = \frac{0.16A_{SP} + A_{TP}}{1A_{BP}} = \frac{0.16(\frac{49.125}{220.25}) + (\frac{8}{220.25})}{(\frac{45}{220.25})} = 0.35$$

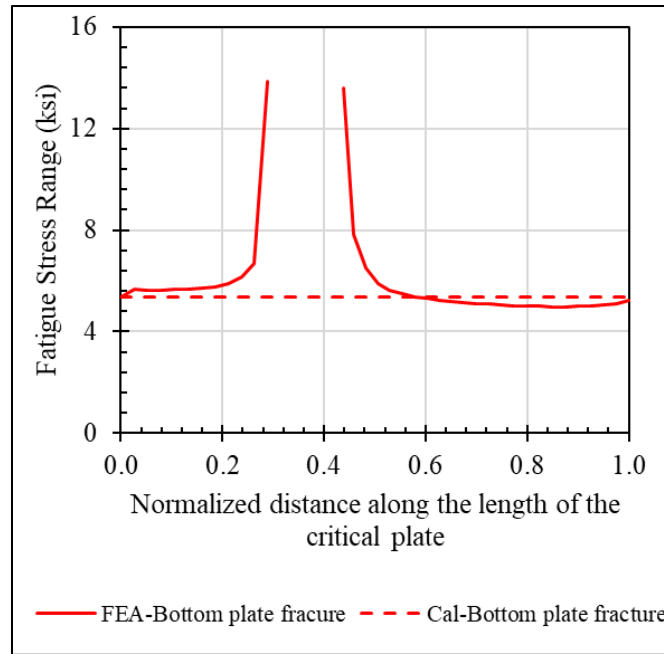
$$\text{Amplification factor } (\beta_{flex}) = 2.2$$

$$\Delta FFS_{Flex} = \Delta FS_{Flex} (1 + \alpha_{Flex} \cdot \beta_{Flex}) = 1 (1 + (2.2 \times 0.35)) = 1.77 \text{ ksi}$$

$$\Delta FFS_{Total} = \Delta FFS_{Axial} + \Delta FFS_{Flex} = 2.73 + 1.77 = 4.5 \text{ ksi}$$

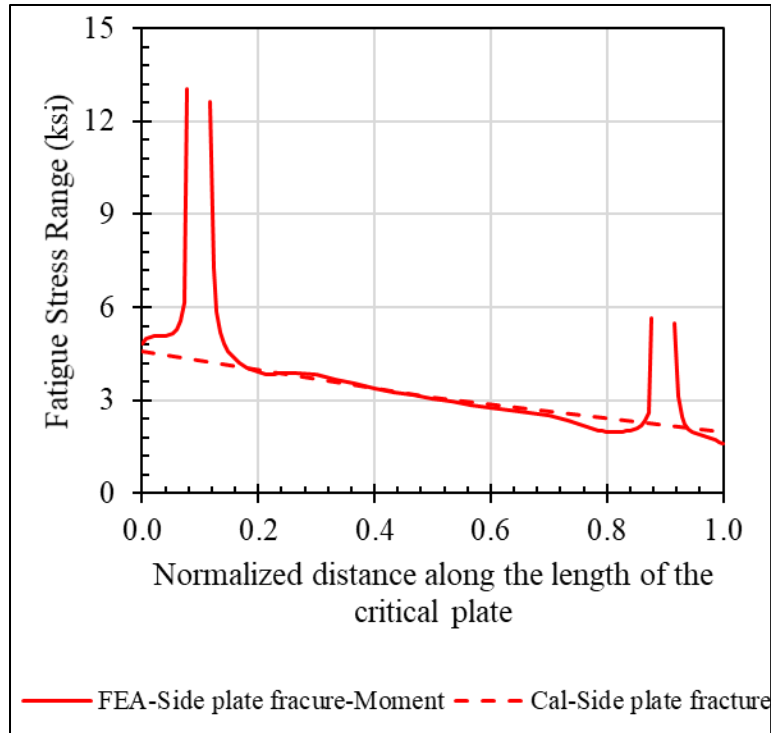
The calculated stress values are compared with the FE results and plotted in the corresponding figures. For the bottom plate fracture scenario, the comparison is shown in Figure 91. The stress distribution under side plate fracture for combined axial and flexural loadings is presented in Figure 92. In both figures, solid lines represent the FE results, and the dashed lines represent the values estimated using the proposed method.

The peaks observed in the FE results correspond to localized stress concentrations at the bolt holes. Although these can be approximated using a stress concentration factor of approximately 2.5, such localized effects are not explicitly captured in the simplified plots shown here, which focus on the nominal stress distribution. The overall comparison of the plots shows that the stress estimation in the fractured condition was well-predicted using the proposed equations.



Source: FHWA

**Figure 91. Graph. Comparison between simplified method and FEA for fatigue stress in the critical plate in the LaCrosse TB when bottom plate is fractured.**



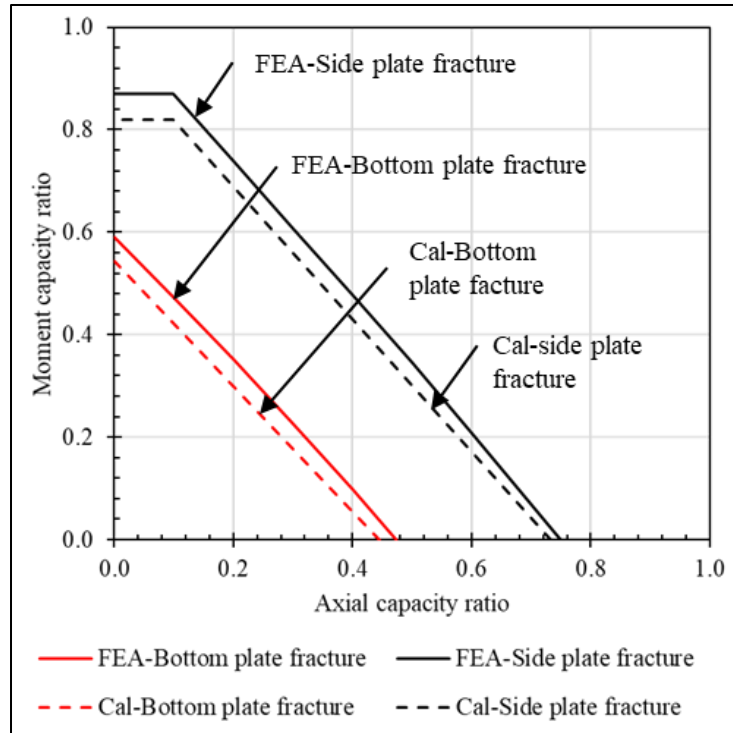
Source: FHWA

**Figure 92. Graph. Comparison between simplified method and FEA for fatigue stress in the critical plate in the LaCrosse TB when side plate is fractured.**

Overall, the comparison for the horizontal tab configuration under both bottom and side plate fracture conditions demonstrates strong agreement between the calculated results and those obtained from FEA, for both strength and fatigue assessments.

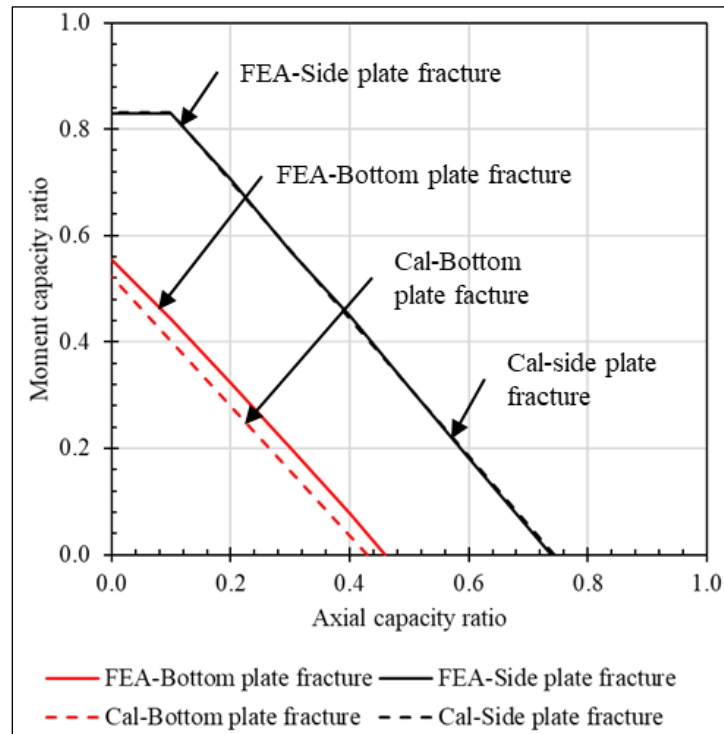
## 8.2 ASSESSMENT OF PROPOSED FORMULATION FOR VERTICAL TAB-BASED TBS

Similar to the horizontal tab configuration, validation calculations were carried out for TBs with vertical tab connections. The resulting P-M interaction curves for the LaCrosse and Atchison bridge geometries are presented in Figure 93 and Figure 94, respectively. In both cases, the estimated curves generated using the proposed simplified method closely match the results from detailed FEA, thereby confirming the reliability and accuracy of the formulation for evaluating the remaining strength of TBs with vertical tab corner connections.



Source: FHWA

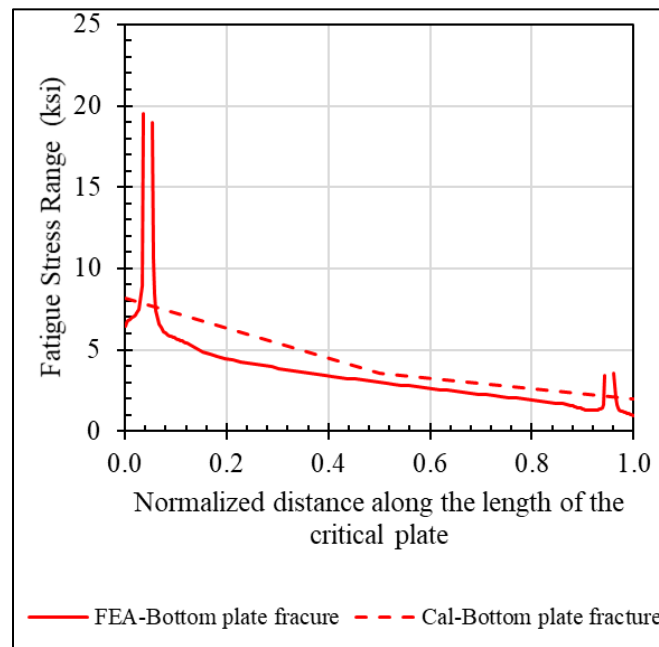
**Figure 93. Graph. P-M curve comparison between simplified method and FEA for LaCrosse TB with vertical tabs when bottom plate is fractured.**



Source: FHWA

**Figure 94. Graph. P-M curve comparison between simplified method and FEA for Atchison TB with vertical tabs when bottom plate is fractured.**

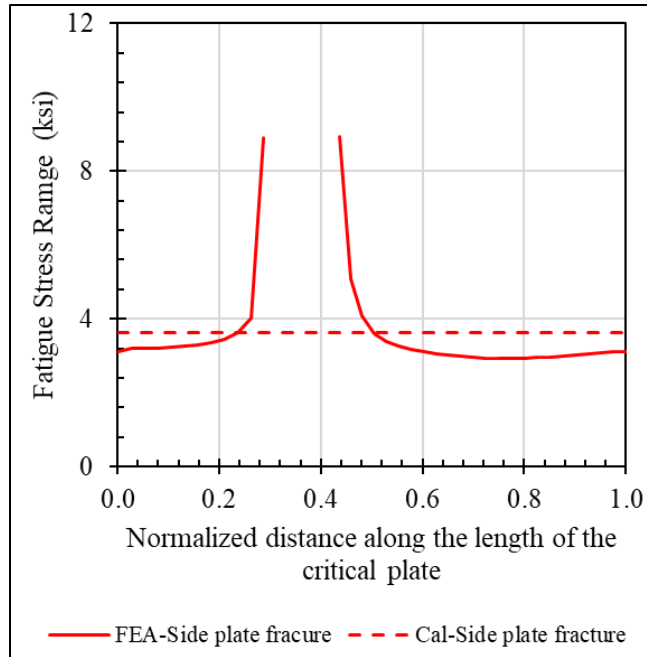
The fatigue validation for TBs with vertical tab connections was carried out by comparing the estimated stress distributions with FEA results for both bottom plate and side plate fracture conditions. For LaCrosse, the stress distribution in the critical plate under bottom plate fracture condition is presented in Figure 95, and the results for side plate fracture are shown in Figure 96. For both fracture conditions, the calculated stress ranges closely matched the FEA results, particularly at mid-length and near the ends of the critical plates. This agreement confirms the effectiveness of the proposed method in evaluating fatigue demand across different loading conditions and fracture scenarios in vertical tab configurations.



Source: FHWA

**Figure 95. Graph. Comparison between simplified method and FEA for fatigue stress in the critical plate in the LaCrosse TB with vertical tabs when bottom plate is fractured.**



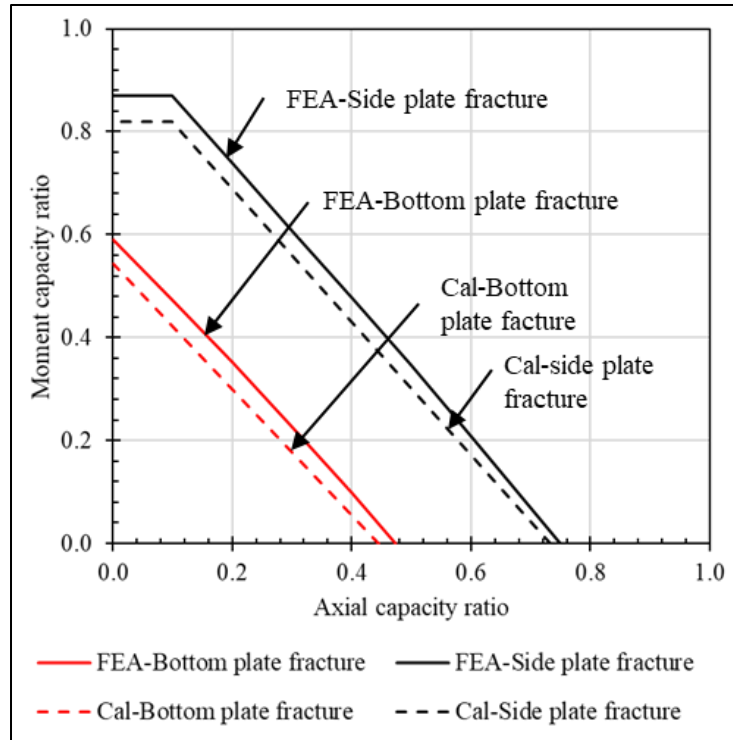


Source: FHWA

**Figure 96. Graph. Comparison between simplified method and FEA for fatigue stress in the critical plate in the LaCrosse TB with vertical tabs when side plate is fractured.**

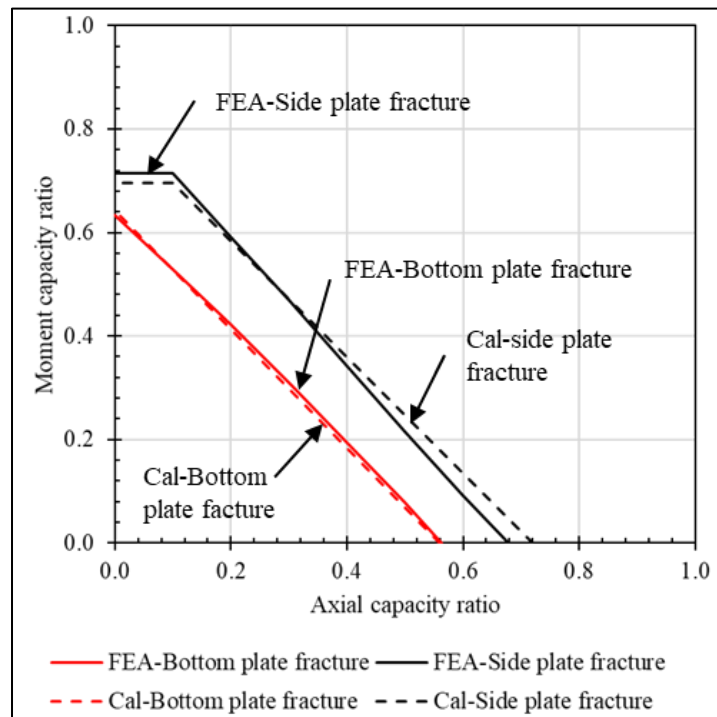
### 8.3 ASSESSMENT OF PROPOSED FORMULATION FOR ANGLE-BASED TBS

Similar to the tab configurations, validation calculations were also conducted for TBs with angle connections. The resulting P-M interaction curves for the LaCrosse and Atchison bridge geometries are shown in Figure 97 and Figure 98, respectively. These estimates were generated using the equations for angle connections developed in Chapters 5 and 6. In both cases, the estimated curves closely follow the detailed FEA results, confirming the reliability of the simplified method in predicting the remaining strength of TBs with angle-type corner connections under both bottom plate and side plate fracture conditions.



Source: FHWA

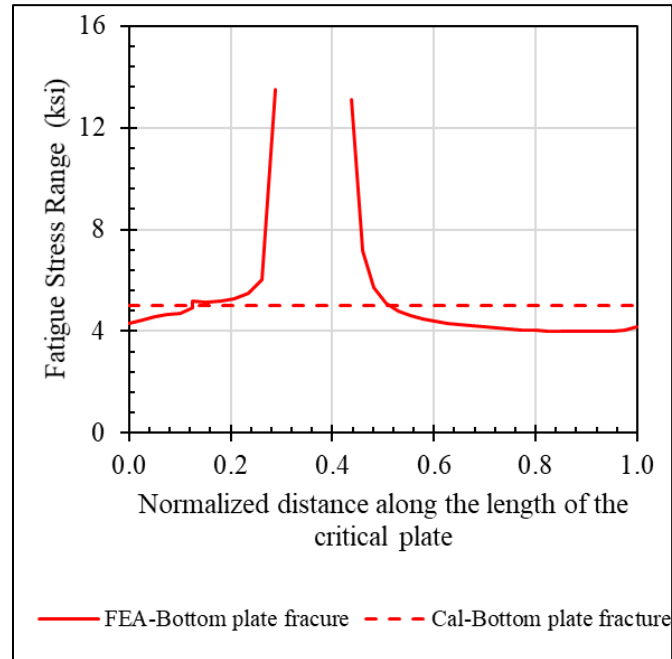
**Figure 97. Graph. P-M curve comparison between simplified method and FEA for LaCrosse TB with angles when bottom plate is fractured**



Source: FHWA

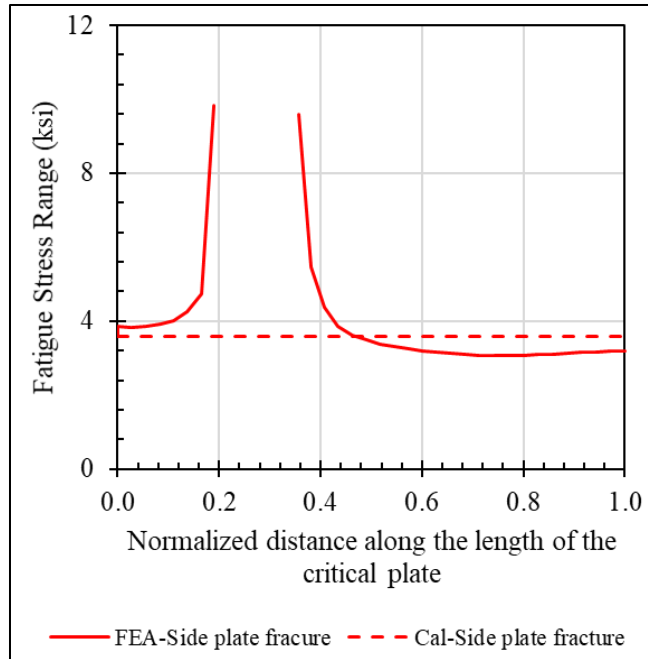
**Figure 98. Graph. P-M curve comparison between simplified method and FEA for Atchison TB with angles when bottom plate is fractured**

The fatigue validation for TBs with angle-type corner connections was conducted by comparing the stress ranges estimated using the proposed method with those obtained from detailed FEA simulations under both bottom plate and side plate fracture conditions. The results for LaCrosse are generated. Figure 99 captures the stress distribution in the critical angle component under the bottom plate fracture. While Figure 100 depicts the stress response for a side plate fracture. In both scenarios, the simplified estimates closely align with the FEA results, especially at key locations along the angle leg. This agreement highlights the robustness and reliability of the proposed methodology for evaluating fatigue performance in angle-connected TBs across a range of fracture and loading conditions.



Source: FHWA

**Figure 99. Graph. Comparison between simplified method and FEA for fatigue stress in the critical plate in the LaCrosse TB with angles when bottom plate is fractured**



Source: FHWA

**Figure 100. Graph. Comparison between simplified method and FEA for fatigue stress in the critical plate in the LaCrosse TB with angles when side plate is fractured**

In summary, the validation study confirmed the accuracy and applicability of the proposed simplified methodology for evaluating both strength and fatigue performance of TBs. The approach was tested on two independent TB geometries named: LaCrosse and Atchison, that were not included in the formulation development. Across all scenarios, including bottom and side plate fracture conditions and three different connection configurations, the simplified estimates showed strong agreement with detailed FEA results. This consistency demonstrates that the proposed method reliably captures the key structural behaviors influencing remaining capacity and fatigue demand in faulted TBs. As such, the methodology offers a practical, efficient, and robust tool for assessing damaged TBs in tied arch bridges, suitable for integration into bridge evaluation and maintenance practices.

## 9 SUMMARY AND CONCLUSIONS

This report was motivated by a key gap in current practice: there is no direct methodology available for estimating the remaining strength and fatigue performance of TB in tied arch bridges under faulted conditions involving combined axial and bending loads. To address this, a detailed FE-based analytical study was carried out. The study began with the development of two global bridge models - one with a deep TB and the other with a shallow tie TB - to investigate the influence of localized component fractures on the overall structural response.

In global models, fractures were introduced at high-demand regions (midspan and quarter span) in the bottom plate and a side plate. In all cases, the global response of the bridge remained unaffected, indicating that the internal forces were effectively redistributed within the TB cross-section. This observation confirmed the feasibility of using localized submodel analyses to evaluate the behavior of the fractured tie beam.

Subsequently, detailed submodels were developed for thirteen TB geometries with varying geometric properties, including differences in depth, flange width, and plate thicknesses. These geometries were analyzed across three corner connection types - horizontal tabs, vertical tabs, and angle connections - and under both bottom plate and side plate fracture condition. A simplified method was proposed using P-M interaction curves to estimate the remaining capacity. The equations developed for each connection type were strongly dependent on the percentage area fractured. They were validated using two additional TB geometries from the LaCrosse and Arkansas River bridges, which were not part of the original dataset.

In parallel, the fatigue behavior of faulted TBs was evaluated. For each fracture and connection configuration, the critical plate responsible for carrying the redistributed load was identified. The submodels were subjected to axial and bending stress separately, and the resulting stress ranges were used to formulate scaling and amplification factors. These estimates were validated against FE simulations and demonstrated good agreement.

Overall, the strength and fatigue methodologies developed in this study provide a simplified and practical framework for assessing the residual performance of fractured TBs with different geometric configurations. The proposed simplified equations can be readily used by engineers for inspection planning and decision-making, addressing a critical need in the evaluation of TBs in faulty condition.

### 9.1 CONCLUSIONS

The study addressed a significant gap in current bridge evaluation practices by providing practical, validated tools to estimate remaining axial and flexural capacities and fatigue stress ranges after localized component fracture in the TBs. The key findings of the study are presented below:

- Global bridge models with both shallow and deep TBs were developed to assess the impact of localized fractures in either the bottom or side plate. The results showed no significant changes in global forces or displacements, confirming that force redistribution within the TB cross-section maintains overall bridge behavior.

- Based on this, a submodeling approach was adopted. Submodels used forces from the global analysis and effectively captured localized stress redistribution and internal redundancy following fracture.
- Three corner connection configurations were evaluated: horizontal tabs, vertical tabs, and angle connections. Each connection type dictated which component became critical after fracture and how loads redistributed across the cross-section.
- The concept of a critical plate, the component attracting the majority of post-fracture load, was essential to both strength and fatigue analysis. Focusing on this plate improved the efficiency and accuracy of the assessment framework.
- A key finding was that the remaining capacity of a fractured TB is strongly influenced by the percentage of the cross-sectional area that is fractured, regardless of other geometric variations. Higher fractured area percentages resulted in more severe capacity reductions.
- Simplified equations were developed to estimate P-M interaction curves using only axial capacity and a geometry-informed slope for bending. These were formulated based on fracture area and cross-sectional characteristics.
- For fatigue assessment, axial and bending stress ranges were evaluated separately. Stress scaling relationships were created using geometric ratios to estimate the redistributed stress in the critical plate after fracture.
- The proposed simplified formulations were validated against two additional TB geometries from the LaCrosse and Atchison bridges. These were not part of the development dataset. The simplified predictions closely matched detailed FEA results for both strength and fatigue, demonstrating the accuracy and reliability of the proposed methodology.

## 10 REFERENCES

1. National Bridge Inspection Standards, 23 CFR 650 Subpart C.
2. Lloyd, J. B., Martin, F. J. B., Korkmaz, C., & Connor, R. J. (2021). Internal Redundancy of Mechanically Fastened Built-Up Steel Axially Loaded Multicomponent Members. *Journal of Bridge Engineering*, 26(7), 04021040. [http://dx.doi.org/10.1061/\(ASCE\)BE.1943-5592.0001743](http://dx.doi.org/10.1061/(ASCE)BE.1943-5592.0001743).
3. Federal Highway Administration (FHWA). Tech Brief: Evaluation of Member and Load-Path Redundancy on the US-421 Bridge Over the Ohio River. FHWA-HRT-13-105. <https://www.fhwa.dot.gov/publications/research/infrastructure/structures/bridge/13105/index.cfm>.
4. Hebdon, M. H., Bonachera Martin, F. J., Korkmaz, C., & Connor, R. J. (2017). Fracture Resilience of Steel Built-Up Members Subjected to Flexure. *Journal of Bridge Engineering*, 22(7). [https://doi.org/10.1061/\(ASCE\)BE.1943-5592.0001059](https://doi.org/10.1061/(ASCE)BE.1943-5592.0001059).
5. Hebdon, M. H., Bonachera Martin, F. J., Korkmaz, C., & Connor, R. J. (2017). Load redistribution and remaining fatigue life of steel built-up members subjected to flexure following a component failure. *Journal of Bridge Engineering*, 22(9). [http://dx.doi.org/10.1061/\(ASCE\)BE.1943-5592.0001087](http://dx.doi.org/10.1061/(ASCE)BE.1943-5592.0001087).
6. American Association of State Highway and Transportation Officials. (2018). Guide specifications for internal redundancy of mechanically-fastened built-up steel members (with 2022 interim revisions).
7. National Transportation Safety Board. (1970). Collapse of U.S. 35 Highway Bridge, Point Pleasant, West Virginia December 15, 1967. Highway Accident Report NTSB/HAR-71-1. Washington, D.C..
8. American Association of State Highway and Transportation Officials. (1978). Guide Specifications for Fracture Critical Non-Redundant Steel Bridge Members. Washington D.C..
9. National Transportation Safety Board. (1984). Collapse of a Suspended Span of interstate Route 95 Highway Bridge Over the Mianus River Greenwich, Connecticut, June 28, 1983. Highway Accident Report NTSB/HAR-84/03. Washington, D.C..
10. Federal Highway Administration (1986). Inspection of Fracture Critical Bridge Members, Supplement to the Bridge Inspector's Training Manual. Report Number FHWA-IP-86-026. McLean, VA.
11. American Association of State Highway and Transportation Officials. (2020). AASHTO LRFD bridge design specifications (9th ed.). Washington, D.C.

12. Federal Highway Administration (2022). Memorandum. Subject: ACTION: Inspection of Nonredundant Steel Tension Members. Washington, D.C.
13. American Association of State Highway and Transportation Officials. (2018). Guide specifications for analysis and identification of fracture critical members and system redundant members. Washington, D.C.
14. Santosuosso, B. J., McGormley, J., Warke, R. W., & Kern, T. M. (2021). I-40 Hernando DeSoto Bridge fracture investigation.
15. National Transportation Safety Board. (2008). Collapse of I-35W Highway Bridge Minneapolis, Minnesota August 1, 2007. Highway Accident Report NTSB/HAR-08/03. Washington, D.C.
16. American Association of State Highway and Transportation (AASHTO). The Manual for Bridge Evaluation, Third Edition, 2017, with 2018 And 2020 Interim Revisions and November 2021 Errata. Washington, D.C., 2018. Available from: [www.transportation.org](http://www.transportation.org).
17. Niemann, T. L. (1999). Hastings Bridge Fracture Investigation. The 16th International Bridge Conference. Pittsburgh, PA. June 14-16, 1999.
18. ASTM International. (2018). Standard specification for metallic-coated parallel and helical steel wire structural strand (ASTM A586-18). <https://www.astm.org/a0586-18.html>.
19. Beyer, W. E. (1984). Preliminary analysis and hanger adjustment of tied arch bridges (Master's thesis, Montana State University).
20. Ocel, J. (2013). Guidelines for the Load and Resistance Factor Design and Rating of Riveted and Bolted Gusset-Plate Connections for Steel Bridges.